Università degli Studi Roma Tre

Physics Department 'Edoardo Amaldi'

Quantum Transport in low-dimensional *Si/SiGe* and *AlGaN/GaN* systems

by

Giulia Frucci

Dissertation submitted to the

Department of Physics

in partial fulfillments of the requirements for the degree of

Doctor of Philosophy

Supervisors

Prof. Florestano Evangelisti

Dr. Luciana Di Gaspare

Coordinator

Prof. G. Altarelli

Academic Year 2008/2009

Contents

Introduction

In recent years the study of electronic properties of low dimensional mesoscopic systems has attracted considerable interest. One of the reasons for this is the opportunity it gives of investigating a wide range of new effects related to ballistic transport and phase coherence. Another reason can be found in the possibility it gives of fabricating nanostructures both for microelectronics and for possible applications in quantum computing and spintronics in general.

The two-dimensional electron gas (2DEG) is one of the most appealing starting points for achieving low-dimensional systems, i.e. systems where the motion of carriers is confined to two or less directions. Today a 2DEG can be obtained easily by growing semiconductor heterostructures. As a matter of fact, recent advancements in the deposition of high quality semiconductor heterostructures allows to confine carriers and obtain high-mobility two dimensional electron gases. In addition the novel micro and nanofabrication techniques allow to build nanodevices, suitable for the investigation of quantum transport.

In the field of quantum transport much attention has been focused on effects related to spintronics, electron correlation and coherent cotunneling, as well as the role of impurities and disorder in low carrier density systems, single charging phenomena and spin phenomena such as the spin Hall effect. To explain these effects it is necessary to go beyond the one-electron picture which is able to account, for example, for the conductance quantization in $G_0 = 2e^2/h$ units, to be found in one dimensional ballistic conductors. Indeed, many experiments with different kinds of devices (quantum point contacts, single electron transistors, etc.), have revealed unexpected behaviours, whose origins are still being debated. As an example, we mention the so-called *0.7 anomaly* in the $AlGaAs/GaAs$ quantum point contacts, or the

presence of *Kondo effect* in quantum dots.

These scenarios become more intriguing when Si-based nanostructures are considered since, in this case, quantum transport properties become more complex for the presence of valley degeneracy.

Recent advancements in the growth of lattice mismatched heterostructures allow to achieve high quality $Si/SiGe$ 2DEGs. These have emerged as promising alternative systems for basic research in the field of 2D electron physics, which was previously mainly restricted to $AlGaAs/GaAs$ heterostructures. Si-based 2DEG is an interesting platform for spin physics and quantum information, due to the weak spin-orbit coupling in Si and to the presence of nuclear zero spin isotopes, which make electron spin coherence time extremely long. However, silicon has a near degeneracy of orbital states in the conduction band, arising from multiple valley minima, which can enhance decoherence rates and make qubit operation in quantum computing more complicated. In quantum wells, the valley degeneracy is lifted, but if the splitting is smaller than or comparable to the spin splitting, the problem of decoherence or interference still exists. It has been shown that quantum confinement in nanostructures provides some amount of control over the valley splitting. Indeed, recent measurements in a split-gate quantum point contact (QPC) have shown that the valley splitting can reach a value of the order of $0.5 \div 2\ meV$, being enhanced by the lateral confinement of the electron wave-function exerted by electrostatic and magnetic means [1].

In the past ten years, due to developments in the field of $AlGaN/\ GaN$ heteostructures, research has focused also on GaN-based 2DEG. The latter is in fact among the most promising materials for the study of properties related to ballistic transport and it is interesting from a technological point of view. This technological interest derives from the relevance that GaN has assumed for applications in high-power and high-temperature microelectronic devices. The large band offset and the strong piezoelectric effect in this material system have been shown to generate an intrinsic high sheet density two-dimensional electron gas with enhanced electron mobility. In addition, the relatively heavy mass of electrons makes GaN 2DEGs a convenient system for studying spin-polarized and electron-electron correlation effects. In particular, a high value of the dimensionless parameter r_s, governing the strength of the e-e interaction, can be obtained thanks to the

low value of the relative dielectric constant, even at relatively high electron concentrations, like $n_s \sim 10^{13} cm^{-2}$, which is the value found in our sample. The strong spontaneous and piezoelectric polarization charge gives these systems a strong asymmetric electric field at the interface, which can also enhance the spin-orbit interaction, thus providing a spin-splitting energy of the conduction band states at zero-external field.

In this dissertation we report the electron transport measurements of Si- and GaN-based low-dimensional systems.

As for the Si structures, we have investigated quantum transport properties of strongly-confined Shottky-gated constrictions, made starting from Si-based 2DEG and focusing on the conductance behaviour of nanostructures with various geometries. Measurements have been made as a function of the gate voltage, the source-drain bias and the magnetic field. Our results reveal a complex framework due to the occurrence of deviations from the ideal quantized conductance behaviour. For instance, these can be due to backscattering from impurities or transmission resonance, produced by multiple reflections, for the presence of an abrupt geometry of the confining potential. However our findings have revealed a zero-field energy valley splitting in our etched-nanostructures, due to the strong confinement generated by physical etching of the 2DEG heterostructures. In practice, in different devices we found a valley splitting energy of the order of $\sim 1 meV$ that is comparable to values reported in literature.

As for the GaN structures, we studied the electrical properties of an $AlGaN/GaN$ system, exploiting both classical and quantum Hall effect. In the preliminary investigation of the 2DEG new interesting problems have come out of the analysis of both Shubnikov-de Haas and low-field measurements. For instance, the occupancy of a second energy level of the 2DEG or the occurrence of a zero-field spin-splitting due to spin orbit interaction. Electron quantum transport of mesoscopic devices on GaN-based heterostructures was also investigated. For these systems we measured the conductance as a function of the gate voltage and the magnetic field. In addition, we investigated the effect of deliberately introducing an asymmetry in the conning potential. In this thesis work we reported the preliminary interpretations of the electron transport measurements on GaN 2DEGs nan-

odevices. For a complete understanding further investigation are required.

Organization of this Dissertation

Chapter 1 gives an introduction of the basic concepts of electronic transport in quantum point contacts. Starting from the description of a 2DEG, the main issues concerning quantum transport in low-dimensional systems are discussed.

In Chapter 2 the main configurations of the measured devices are presented. The experimental set-up, including instruments, filtering and cryostats, has been briefly described.

Chapter 3 presents the electrical characterization and analysis of results of Si-based nanostructures.

Chapter 4 contains the main achievements obtained in the study of a novel system such as GaN-based 2DEG.

Chapter 1

Basic concepts of electron transport in Quantum Point Contacts

In this introductory chapter we will give the basic concepts relevant for electron transport in Quantum Point Contacts (QPC). We will analyse various aspects of electron quantum transport in nanostructures obtained by two-dimensional electron gases (2DEGs). In particular, we will focus on real systems and their problems indicating the non-ideality factors. We will illustrate the outmost important aspects of the systems investigated showing also the differences between the Si/SiGe and GaN/AlGaN two-dimensional electron gases.

1.1 Introduction

The chance of tailoring an artificial potential landscape for electrons in semiconductor nanostructures offers the possibility to study quantum transport in ballistic and quasi-ballistic regimes in low-dimensional systems. Indeed, mesoscopic devices are characterized by a size, L, which can be made smaller or comparable to both the electron coherence length, l_ϕ, and the electron mean free path, l. This means that electrons retain a definite phase and momentum relations during mesoscopic transport, thus allowing coherent processes and ballistic transport to occur. Indeed, l_ϕ is strongly affected by temperature - increasing as the temperature is decreased - and the use of

high mobility two-dimensional electron gas devices allows to reach mean free paths of the order of tens of nanometers or longer. Furthermore, electrons can be easily confined in semiconductor thin film heterostructures since λ_F is large ($\gtrsim 10\ nm$) in semiconductors. This makes the Fermi wavelength λ_F another important length scale to be considered.
In order to measure low-dimensionality effects in mesoscopic devices, typical sizes of the nanostructures must be less than or comparable to the Fermi wavelength. A measure of the importance of interactions in an electron system is the ratio between the typical Coulomb interaction energy and the average kinetic energy of the electron at the Fermi level. This dimensionless parameter r_s is also the average inter-electron spacing in units of the effective Bohr radius, a_{Bohr},

$$r_s = \frac{E_P}{E_K} = \left(\frac{e^2}{4\pi\epsilon \cdot r}\right)\left(\frac{r^2 m^*}{\hbar^2}\right) = \frac{r}{a_{Bohr}}. \tag{1.1}$$

In eq.1.1 m^* is the electron effective mass, ϵ is the dielectric constant specific of the semiconductor used in units of ϵ_0, whereas r is the inter-electron spacing which can be written in terms of the electron sheet density $r = n_s^{-1/2}$. Thus, the dimensionless parameter becomes $r_s = (a_{Bohr}^2 n_s)^{-1/2}$.
For high density electron gases, the kinetic energy is large, and $r_s \ll 1$, therefore interactions are little important and can be treated as a perturbation to the kinetic motion. On the other hand, at low carrier densities, electrons have small kinetic energy, therefore $r_s \gg 1$, and hence interactions dominate in these systems. Midway between these two limits there is a range of r_s where interaction and kinetic energies are comparable. Such systems manifest a number of surprising and complicated effects including Kondo effect and the so called *0.7 anomaly* [2, 3, 4, 5, 6, 7]. Devices investigated in this thesis consist of 2DEGs with $r_s \sim 1$, i.e. they are suitable systems to study electrons interactions.

The 2DEGs used for the successive production of devices are based on $Si/SiGe$ and $GaN/AlGaN$ heterostructures. Each of these 2DEGs shows some peculiar aspects. In the table below, we listed the most important parameters of the two investigated systems along with the typical values of a $GaAs/AlGaAs$-based 2DEG, for comparison.

		Si	GaN	GaAs	Units
Effective Mass	m^*	0.19	0.22	0.067	$m_e = 9.1 \cdot 10^{-31}\ kg$
Spin Degeneracy	g_s	2	2	2	
Valley Degeneracy	g_v	2	1	1	
Dielectric Constant	ϵ	11.9	8.9	13.1	$\epsilon_0 = 8.9 \cdot 10^{-12}\ Fm^{-1}$
Density of States	$\rho(E) = g_s g_v \frac{m^*}{2\pi\hbar^2}$	1.59	0.92	0.28	$10^{15}\ m^{-2} meV^{-1}$
Sheet Density	n_s	0.92	10.57	0.2	$10^{16}\ m^{-2}$
Fermi Wave vector	$k_F = \sqrt{\frac{4\pi n_s}{g_s g_v}}$	1.70	8.15	1.12	$10^8\ m^{-1}$
Fermi Velocity	$v_F = \hbar k_F / m^*$	0.10	0.43	0.19	$10^6\ m/s$
Fermi Energy	$E_F = (\hbar k_F)^2 / 2m^*$	5.8	115.6	7.1	meV
Electron Mobility	μ_e	1	2.02	10^2	m^2/Vs
Transport lifetime	$\tau_t = m^* \mu_e / e$	1.08	2.5	39	ps
Diffusion Constant	$D = v_F^2 \tau_t / 2$	0.006	0.23	0.71	m^2/s
Resistivity	$\rho = 1/n_s e \mu_e$	680	29	31	Ω
Fermi Wavelength	$\lambda_F = 2\pi / k_F$	37	7.7	56	nm
Mean Free Path	$l = v_F \tau_t$	0.112	1.08	7.4	μm
Thermal length	$l_T = \sqrt{\hbar D / k_B T}$	0.21	1.33	2.3	$\mu m (T/K)^{-1/2}$
Cyclotron Radius	$l_c = \hbar k_F / eB$	112	536	74	$nm (B/T)^{-1}$
Magnetic Length	$l_m = \sqrt{\hbar / eB}$	26	26	26	$nm (B/T)^{-1/2}$
Landé factor	g_0	2	2	-0.44	
Inter-electron spacing	$r_s = \frac{1}{\sqrt{a_{Bohr}^2 n_s}}$	3.14	1.43	2.16	
	$k_F l$	19	883	830	
	$\omega_c \tau_t$	1	2	100	(B/T)
	$E_F / \hbar\omega_c$	9.5	109	2	$(B/T)^{-1}$

Table 1.1: Main electronic properties of the *Si* and *GaN* 2DEGs investigated in this thesis work and of a typical *GaAs* 2DEG.

The most evident difference between these materials is the heavy mass of electrons both in Si and GaN compared to $GaAs$ 2DEGs. This produces lower mobilities compared to Gallium Arsenide gases. The typical mean free path is not greater than few hundreds of nanometers, with the ordinary values for the sheet carrier density in $Si/SiGe$ 2DEGs. On the contrary, GaN 2DEGs, having larger electronic densities, allow to obtain larger mean free paths, comparable with those of high-mobility $GaAs$ heterostructures. As already mentioned, the dimensionless parameter is representitive of the significance of electron interactions in the 2DEG. Regarding silicon, the low electron density along with the heavy mass of electrons indicate that e-e interactions are relevant in this system. However, it is possible to tune the value of r_s, and therefore the e-e interactions, also by changing material system, i.e. by moving to a system with different dielectric constant and/or effective mass or by controlling the electron density. Indeed, though the large carrier density in GaN 2DEG would point to a non-interacting electron system, the large electron mass along with the lower dielectric constant ($\epsilon = 8.9\epsilon_0$) makes the dimensionless interaction strength comparable to that of $GaAs$ 2DEGs.

In the following section a brief review will be given on the formation of a two-dimensional electron gas in $Si/SiGe$ and $GaN/AlGaN$ heterostructures.

1.2 *Si/SiGe* and *GaN/AlGaN* 2DEGs

The two-dimensional electron gases based on semiconductors heterojunction are the basic structure for the fabrication of mesoscopic devices. The fabrication processes of 2DEG in Si and in GaN include quite different steps as well as diverse basic principles, so they will be discussed separately.

The Si QPCs described in this thesis are made from 2DEG which forms at the interface of a $Si/SiGe$ heterostructure. Details of the $Si/SiGe$ heterostructure growth can be found in ref.[8, 9]. In order to produce the confinement of the carriers within the silicon channel, a tensile Si film must be grown on top of a relaxed $Si_{1-x}Ge_x$ layer. The sequence of the structure along with the thickness of each layer is reported in fig.1.1. Starting from

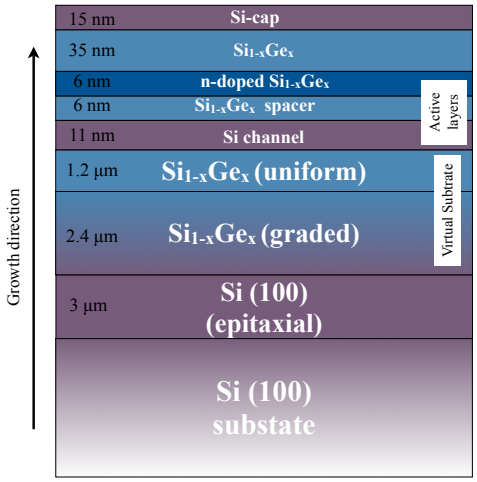

Figure 1.1: Layer sequence utilized for the realization of *Si* QPC measured in this thesis.

a bulk $Si(100)$ substrate, an epitaxially grown film of Si was deposited to improve the crystalline quality. The electrical performances of the structure crucially depend on the crystalline quality of the relaxed $Si_{1-x}Ge_x$ layer deposited hereafter. The best results were obtained by using a compositionally graded $SiGe$ buffer layer on the epitaxial Si surface followed by a thick $SiGe$ layer at a fixed composition ($Si_{0.81}Ge_{0.19}$). This structure is commonly referred to as a virtual substrate (VS). In this way, it is possible to confine the dislocations within the graded layer and to obtain a dislocation density at the sample surface lower than $10^6\ cm^{-2}$. The active layers were obtained by using *Low Pressure Chemical Vapour Deposition* (LPCVP), depositing on the VS the following: (i) a tensile Si channel layer (thickness 11 nm), (ii) a $Si_{0.81}Ge_{0.19}$ spacer layer (thickness 6 nm), and (iii) a n-doped $Si_{0.81}Ge_{0.19}$ (thickness 6 nm). The structure was completed by a second 35 nm thick $Si_{0.81}Ge_{0.19}$ spacer layer followed by a Si cap layer.

Free carriers for the 2DEG are provided by the n-type dopants located in the $SiGe$ doped layer and transferred into the triangular potential well formed in the Si channel. A typical band diagram of a similar heterostructure is shown in fig.1.2 (a). A triangular potential well is formed at the interface between the Si channel and the $SiGe$ spacer. At low temperature, electrons are present only where the conduction band dips below the Fermi energy. As a result, free electrons in the system are confined in the poten-

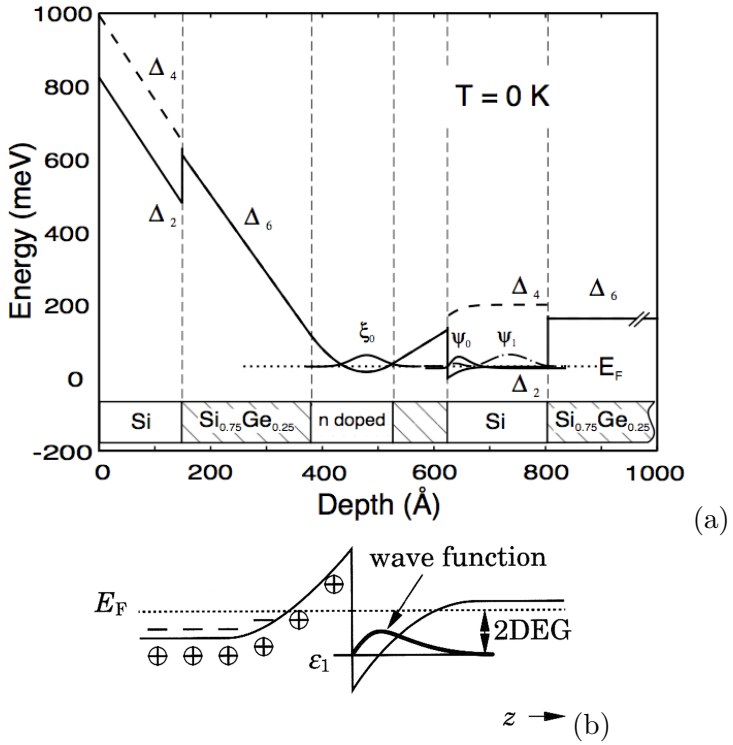

Figure 1.2: (a) Potential variation in an n-type $Si/SiGe$ modulation doped structure on a relaxed $Si_{0.75}Ge_{0.25}$ buffer layer. Only the lowest subband Ψ_0 in the well is occupied at 0 K. From ref. [10]. (b) Schematics of the energy diagram in a generic modulation doped heterostructure.

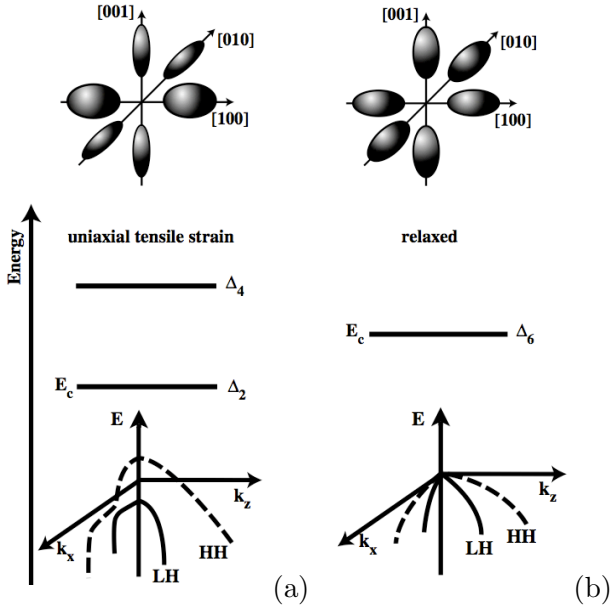

Figure 1.3: Valley structure, conduction band and valence band splitting of (a) bulk silicon and (b) uniaxial tensile strained silicon grown on $Si_{1-x}Ge_x$ virtual substrate.

tial well close to the heterointerface. Thus, quantized energy levels form in the potential well. At the typical electron densities for this 2DEG only the first level is populated (see fig.1.2 (b)), localizing electrons in the z-direction to few nanometers from the interface. By using a rough estimate and assuming a triangular well approximation [11], the second subband level lays approximately 37 meV above the first in our Si 2DEG. Since this value is much higher than the Fermi energy of our 2DEG, $E_F \approx 5.8\ meV$ (see table 1.1), than the measurement temperature ($T < 1K \approx 86\mu eV$) and than the excitation bias ($eV_{ex} \approx 10\mu eV$), the second subband is unoccupied, and the electron gas can be considered two-dimensional.

The amount of transferred charge and hence the electron sheet density in the silicon channel depends both on the concentration of dopants and on the transfer efficiency which is reduced for thick spacer layers. On the other hand the spacer layer is necessary to reduce the Coulomb scattering of the electrons from the ionized impurities of the doped layer. Therefore, the thickness of the spacer layer has to be tailored to allow both the increase of mobility and a significant charge transfer efficiency.

One peculiar characteristic of the Si 2DEG, compared to $GaAs$ or GaN-based 2DEGs, is the presence of the valley-degeneracy in the conduction band. Indeed cubic bulk (relaxed) silicon has six conduction band minima along the Δ-direction, see fig.1.3 (a). However, due to the existence of about 4.2% lattice mismatch between Si and Ge, band structure of Si in a $SiGe$ heterostructure is modified under tensile strain. The strain split the conduction band minima so that Δ_2 (twofold degenerate) is lower in energy than Δ_4, see fig.1.3 (b). Therefore, in a Si channel under biaxial tensile strain, as it is in the case of our 2DEG, the transport parallel to the heterostructure interface involves only electrons with transverse effective mass (those from the Δ_2 minima of the conduction band, see fig.1.2 (a)), due to the partial removal of the valley degeneracy [10].

The sequence of the heterostructure for the formation of the GaN-based 2DEG is reported schematically in fig.1.4. The formation mechanism of the

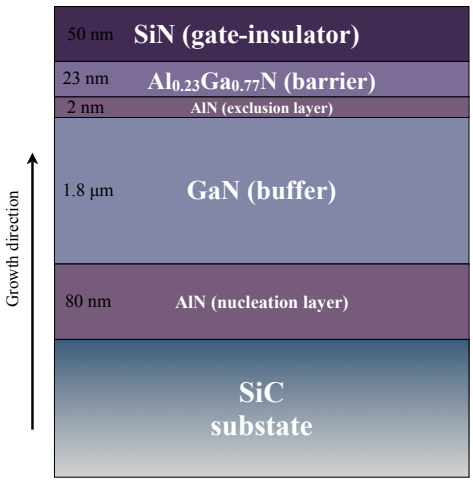

Figure 1.4: Layer sequence utilized for the realization of GaN QPC measured in this thesis.

2DEG in $AlGaN/GaN$ heterostructures is profoundly different from those described for $Si/SiGe$ or $AlGaAs/GaAs$ 2DEGs. In the following, we will give a short description of the principles at the basis of the formation of a two-dimensional electron gas.
The peculiar aspect of the 2DEG $AlGaN/GaN$ heterostructures is that the formation of the electron gas does not necessarily require the introduction

of additional defects associated with doping. Indeed, free carriers can also result from the spontaneous and piezoelectric polarization charge (this effect is typically referred to as a *piezoelectric doping*): thanks to the strong piezoelectric and spontaneous polarization in III-nitrides, it is possible to enhance the carrier concentration to values up to $2 \cdot 10^{13}\ cm^{-2}$ [12].

The natural crystal structure of III-nitrides is wurtzite, a hexagonal structure defined by the edge length a_0 of a basal hexagon, the height c_0 of the hexagonal prism, and an internal parameter u defined as the anion-cation bond length along the c-axis, in units of c_0. Wurtzite is the structure with the highest symmetry compatible with the presence of spontaneous polarization [13], and the piezoelectric tensor of wurtzite has three non-vanishing independent components. Two of these components measure the piezoelectric polarization P_{PE} induced along the c-axis,

$$P_{PE} = e_{33}\epsilon_z + e_{31}(\epsilon_x + \epsilon_y), \tag{1.2}$$

where $\epsilon_z = (c - c_0)/c_0$ is the strain along the c-axis, the in-plane strain $\epsilon_x = \epsilon_y = (a - a_0)/a_0$ is assumed to be isotropic, e_{33}, e_{31} are the piezoelectric coefficients, and a and c are the lattice constants of the strained layer. To determine the amount of piezoelectric polarization in the direction of the c-axis through the change in polarization induced by variations of the lattice constants a and c only, we can consider the relation

$$\frac{c - c_0}{c_0} = -2\frac{C_{13}}{C_{33}}\frac{a - a_0}{a_0}. \tag{1.3}$$

Thus, the piezoelectric tensor can be written as,

$$P_{PE} = 2\frac{a - a_0}{a_0}\left(e_{31} - e_{33}\frac{C_{13}}{C_{33}}\right), \tag{1.4}$$

where C_{13} and C_{33} are elastic constants [13]. From a microscopic point of view, a strain parallel or perpendicular to the c-axis produces an internal displacement of the metal sublattice with respect to the nitrogen ones, i.e. a variation of the parameter u of the wurtzite structure. The measured piezoelectric polarization is due to the effect of the change of the macroscopic lattice constants and to the associated change in u. The piezoelectric polarization increases with strain and, for crystals or epitaxial layers under the same strain, in the direction from GaN to AlN. The value of spontaneous

polarization is predicted to be very large and also increasing from GaN to AlN, due to the more pronunced nonideality of the crystal structure (u increases, c/a decreases moving far away from the ideal ratio $c/a = 1.633$ for a closed packed hexagonal structure). In the table 1.2 lattice constants, spontaneous polarization and piezoelectric constants of AlN and GaN are reported, taken from [13]. The spontaneous polarization of these group-III

	AlN	GaN
a_0 ($\AA$)	3.112	3.189
c_0 ($\AA$)	4.982	5.185
u	0.380	0.376
P_{SP} (C/m^2)	-0.081	-0.029
e_{33} (C/m^2)	1.46	0.73
e_{31} (C/m^2)	-0.60	-0.49

Table 1.2: Lattice constants, spontaneous polarization and piezoelectric constants of AlN and GaN [13].

nitrides is negative. The orientation of the spontaneous and piezoelectric polarization is defined assuming that the positive direction goes from the metal (cation) to the nearest neighbor nitrogen atom (anion) along the c-axis. Since

$$\left(e_{31} - e_{33}\frac{C_{13}}{C_{33}}\right) < 0 \tag{1.5}$$

is always valid for any Al concentration it follows from eq.1.4 that the piezoelectric polarization is negative for tensile ($a > a_0$) and positive for compressive ($a < a_0$) strained $AlGaN$ barriers, respectively. As a consequence, the piezoelectric polarization is parallel to the spontaneous one in the case of tensile strain, and antiparallel in the case of compressively strained $AlGaN$ layers. In our heterostructure (fig.1.4) an AlN exclusion layer is grown on a GaN buffer layer and therefore under tensile strain. In this specific case the piezoelectric and the spontaneous polarization point in the same direction and the value of the total polarization is the sum of the piezoelectric and spontaneous polarization

$$P = P_{PE} + P_{SP}. \tag{1.6}$$

Since both the values of the piezoelectric and spontaneous polarization increase from GaN to AlN, the total polarization of a strained $AlGaN$ layer is larger than that of a relaxed GaN buffer layer ($|P(AlGaN)| \geqslant |P(GaN)|$). As a consequence of this definition, the negative spontaneous polarization of GaN and $AlGaN$, as well as the negative piezoelectric polarization of an $AlGaN$ layer under tensile strain, points from the nitrogen towards the nearest neighbor Ga (or Al) atom along the c-axis. Therefore, the total polarization of both layers is directed towards the substrate for the Ga-face and towards the surface for the N-face polarity crystals (fig.1.5).

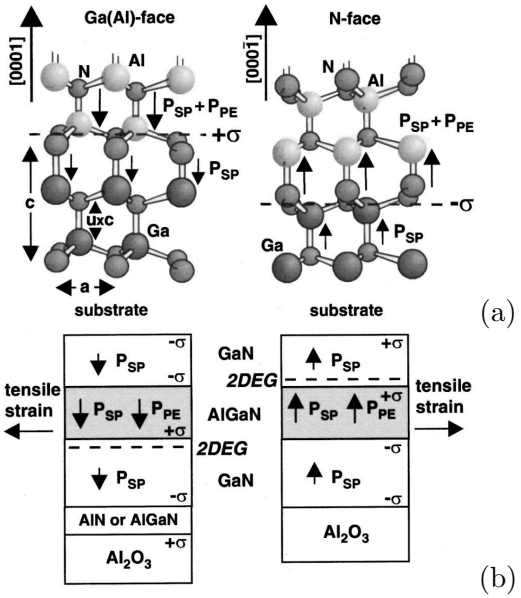

Figure 1.5: Crystal structure of pseudomorfic AlN/GaN heterostructure with $Ga(Al)$-face or N-face polarity. (b) 2DEGs in $GaN/AlGaN/GaN$ heterostructures with Ga-face or N-face polarity. From ref. [12].

The gradient of polarization in space induces a polarization charge density. In analogy, at an abrupt interface of a top/bottom layer heterostructure ($AlGaN/GaN$ or $GaN/AlGaN$), the polarization can decrease or increase within a bilayer, causing a fixed polarization charge density defined by

$$\sigma(P_{PE} + P_{SP}) = \sigma(P_{PE}) + \sigma(P_{SP}). \tag{1.7}$$

If the polarization induced charge density is positive ($+\sigma$), free electrons will tend to compensate the polarization induced charge resulting in the for-

mation of a 2DEG with a sheet carrier concentration n_s, assuming that the triangular quantum well at the $AlGaN/GaN$ interface will drop below the Fermi level E_F. Analogously, a negative sheet charge density $(-\sigma)$ causes an accumulation of holes at the interface if the valence band edge of the $AlGaN/GaN$ heterostructure crosses the Fermi level. The polarization induced sheet charge is found to be positive for $AlGaN$ on top of GaN with $Ga(Al)$-face polarity and for GaN on top of $AlGaN$ with N-face polarity. Therefore, the formation of 2DEGs is expected at the lower $AlGaN/GaN$ and upper $GaN/AlGaN$ interfaces for Ga- and N-face $GaN/AlGaN/GaN$ heterostructures, respectively (fig.1.5 (b)).

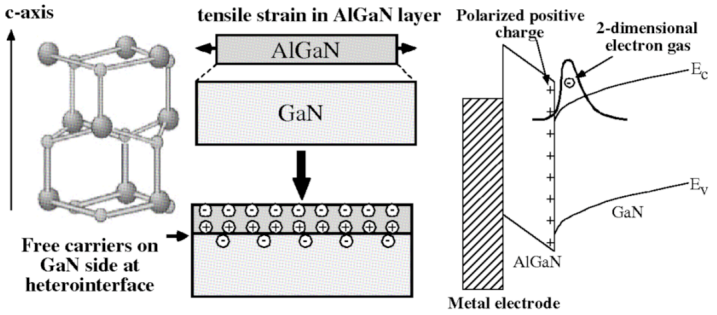

Figure 1.6: $AlGaN/GaN$ heterostructure and its band diagram. When the $AlGaN$ layer is under tensile strain, free carriers are accumulated at the heterointerface owing to the piezoelectric effect caused by the strain and a spontaneous polarization effect, taken from [14].

The total polarization charge in a $AlGaN/GaN$ heterostructure as a function of Al content is given by

$$|\sigma(x)| = |P_{PE}(Al_xGa_{1-x}N) + (P_{SP}(Al_xGa_{1-x}N) - P_{PE}(GaN)|. \quad (1.8)$$

Free electrons tend to compensate the positive polarization induced charge which is bound at the lower $AlGaN/GaN$ interface. For undoped $AlGaN/GaN$ structures, the sheet concentration $n_s(x)$ can be calculated by using the total bound sheet charge $\sigma(x)$,

$$n_s(x) = \frac{\sigma(x)}{e} - \left(\frac{\epsilon_0\epsilon(x)}{d_{AlGaN}e^2}\right)[e\Phi_b(x) + E_F(x) - \Delta E_C(x)] \quad (1.9)$$

where $\epsilon(x)$ is the relative dielectric constant of $Al_xGa_{1-x}N$, d_{AlGaN} is the thickness of the barrier, $e\Phi_b(x)$ is the Schottky barrier of the gate contact,

$E_F(x)$ is the Fermi level with respect to the GaN conduction band edge energy and $\Delta E_C(x)$ is the conduction band offset at the $Al_xGa_{1-x}N/GaN$ interface where a 2DEG forms. The conduction band offset can be calculated from the energy gaps of GaN $(x = 0)$ and $Al_xGa_{1-x}N$:

$$\Delta E_C(x) = 0.7[E_g(x) - E_g(0)] \tag{1.10}$$

where the band gap of $Al_xGa_{1-x}N$ is

$$E_g(x) = xE_g(AlN) + (1-x)E_g(GaN) - x(x-1)1.0eV. \tag{1.11}$$

AlN and GaN bad gaps are 6.13 and 3.42 eV, respectively.
In fig.1.7 the conduction band profiles of $AlGaN/GaN$ and AlN/GaN heterostructures are reported along with the calculated electron wave-function. It is apparent that the inclusion of a thin layer of AlN at the $AlGaN/GaN$

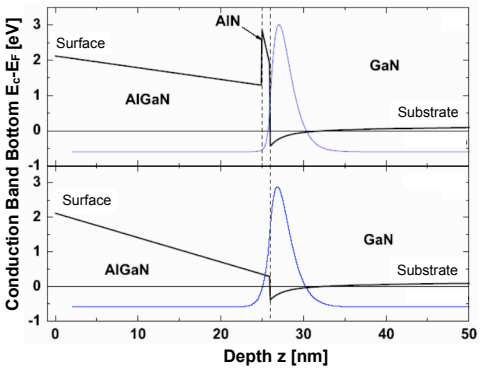

Figure 1.7: Conduction band profile and electron wavefunction calculated for an $AlGaN/GaN$ (upper panel) and an AlN/GaN heterostructure (bottom panel).

interface has a crucial effect on mobility as it reduces the penetration of the electronic wave-function, being the conduction band offset larger for AlN/GaN junctions compared to $AlGaN/GaN$. Furthermore, as AlN is binary, the presence of the AlN exclusion layer suppresses short range scattering eliminating alloy disorder where electrons are localized.
Among all scattering mechanisms, the short range scatterings are those that mostly affects mobility. The electron mobility is $\mu = e\tau_t/m^*$, where τ_t is the transport lifetime. This is the time an electron travels before changing its momentum. It is known [15] that the transport scattering rate is re-

lated to the scattering angle by the relation, $\frac{1}{\tau_t} = \int P(\theta)(1 - cos\theta)d\Omega$ where $P(\theta)$ is the scattering probability at an angle θ. From this relation it is clear that large angle (short range) scattering is efficient in reducing τ_t, and hence the mobility. At low temperature, the most influent scattering mechanisms are interfacial roughness and dislocations. The former is relevant for high density gases since the electrons move closer to the heterojunction. Nevertheless, in our case, the inclusion of the AlN layer lowers the wavefunction penetration thus diminishing also interfacial roughness scattering. Regarding dislocations, these emerge from the lattice mismatch between GaN and substrate. The two most commonly used substrates for GaN epitaxial growth are sapphire and silicon carbide. The problem is that GaN is poorly lattice matched to both sapphire and silicon carbide resulting in defects which degrade electronic device performance. Though the employment of SiC substrates allows to reduce the dislocation density of at least two order of magnitude compared to sapphire, being the difference between lattice parameters smaller, the use of Si as an alternative substrate is having considerable success as it holds much promise for electronic device development [16].
Alloy scattering is a further short range scattering mechanism and it is due to the non uniform distribution of constituents of the ternary alloy. Since the scattering probability depends on the Al concentration x, with the form $P \propto x(x-1)$, it is completely suppressed in presence of the exclusion layer AlN $(x = 1)$ [17, 18].
When there is no intentional doping in $AlGaN/GaN$ heterostructures, the ionized impurity scattering is not due to remote donor impurities inducing the free electron gas, usually present in modulation doped heterostructures. As for our heterostructure, the charge transfer involves the formation of polarization charges that can be considered as a scattering source equivalent to the δ-doping layer in $GaAs/AlGaAs$ systems.

A preliminary electrical characterization of the 2DEGs investigated was carried out by using classical low-field magnetoresistance. Transport properties of the 2DEGs were studied by means of four-terminal resistivity and classical Hall measurements in a cryogenic system equipped with a low magnetic field $(0.7\ T)$ at temperatures between 10 and 300 K. For this purpose, standard Hall bars were fabricated by optical lithography. By measuring

the longitudinal (ρ_{xx}) and the transverse (ρ_{xy}) resistivity, the conductivity and the carrier density were derived:

$$\sigma = \frac{1}{\rho_{xx}} \tag{1.12}$$

$$n_{2D} = \frac{B}{|e|\rho_{xy}}. \tag{1.13}$$

Thus, we calculated the mobility at low field from the relation, $\mu = \sigma/|e|n_{2D}$. The most promising of these 2DEGs were investigated also in the range of Quantum Hall Effect (high magnetic field). In next chapters, we report further descriptions of the measurements carried out.

1.3 Quantum point contacts

The knowledge of the 2DEGs properties described in the previous section is of extremum importance for the study of mesoscopic physics. Indeed, thanks to lithographic processes, it is possible to further reduce the dimensionality of a 2DEG system, achieving mesoscopic devices. The quantum point contact (QPC) is one of the most studied low-dimensional device configurations.

QPCs are short one-dimensional constrictions connected adiabatically to large source and drain reservoirs with a width of the same order of magnitude as the Fermi wavelength and length shorter than the elastic mean free path of electrons [19, 20, 21]. There is more than one way of obtaining a QPC starting from a 2DEG, the different approaches will be described in the next chapter. As for this chapter, we will refer to a QPC as a constriction defined electrostatically by means of a couple of split-gates (see figure 1.8). In a split-gate quantum point contact the width of the channel is controlled by the gate voltage and can be made comparable to the Fermi wavelength. Van Wees et al. [22] and Wharam et al. [23] independently discovered a sequence of steps of magnitude $\frac{2e^2}{h}$ in the conductance trace of such a point contact as its width was varied by means of the voltage applied to the split-gates (fig.1.9). This resulted from the contribution to the conductance of $g \cdot e^2/h$ provided by each 1D subband in the constrictions, being g the overall degeneracy of the electronic states.

If the potential which describes the transition from the wide 2DEG re-

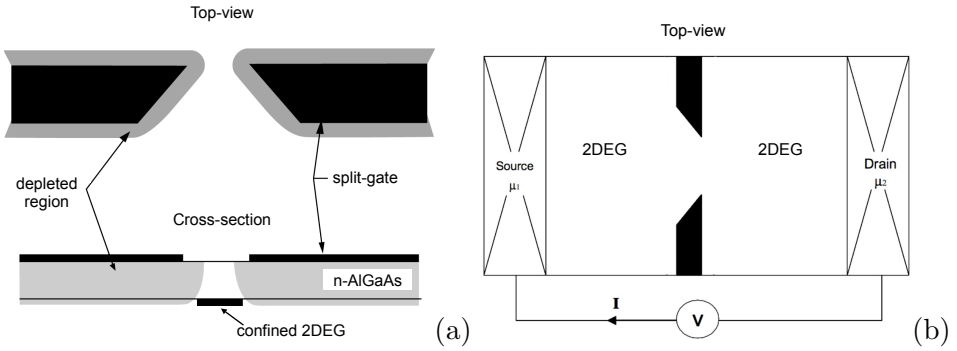

Figure 1.8: (a) Top-view and cross-section of a $GaAs/AlGaAs$ heterostructure with two metal split-gates which, negatively biased, deplete electrons underneath. (b) Top-view of a QPC: the two wide 2DEG regions act as reservoirs, emitting electrons through the QPC with energies up to their electrochemical potentials μ_1 and μ_2.

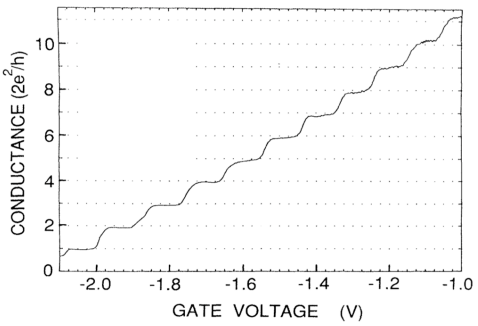

Figure 1.9: (a) Quantized conductance of a QPC at 0.6 K. The conductance was obtained from the measured resistance after subtraction of a constant series resistance of 400 Ω [22].

gions to the narrowest point in the constriction varies sufficiently smoothly (adiabatically), the potential variation in the x- and y-directions may be decoupled. The narrowest point of the constriction forms the bottleneck of the QPC device and it completely determines the transport properties. Thus the quantization of conductance through a QPC can be calculated by using a simple model with the Hamiltonian

$$H = \frac{p_x^2}{2m^*} + \frac{p_y^2}{2m^*} + eV(x,y), \tag{1.14}$$

where $V(x,y) = V(x) + V(y)$ is the electrostatic potential; $V(y)$ is the confining potential in the transverse direction, while $V(x)$ defines the potential along the direction of the current. For the confinement in the y-direction a parabolic potential $V(y) = \frac{1}{2}m^*\omega_y y^2$ can be chosen [24]. This $V(y)$ confinement gives the quantization of the lateral motion with wave-functions of the harmonic oscillator. The 1D electron motion in the x-direction is described by 1D subbands the energy eigenvalues of which are

$$E_n(k_x) = \left(n - \frac{1}{2}\right)\hbar\omega_y + \frac{\hbar^2 k_x^2}{2m^*} + eV_0, \qquad (n = 1, 2, \ldots) \tag{1.15}$$

including the sum of quantized energy due to the lateral confinement (n being the index of the 1D subbands), the kinetic energy of free electrons along the x-axis, and the electrostatic energy eV_0 in the QPC. Figure 1.10 shows the occupied electron states at two different gate voltages. It is known

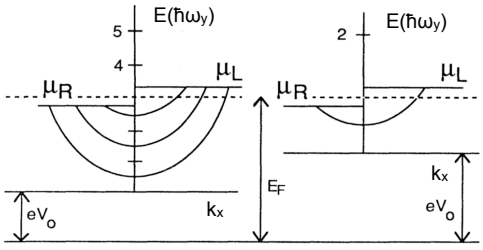

Figure 1.10: Occupied electron states in the channel at two different gate voltages in the case of an applied voltage difference across the QPC, $eV = \mu_R - \mu_L$.

[25] that the effect of gate voltage is twofold: a more negative gate voltage increases both the confinement $\hbar\omega_y$ and the electrostatic potential V_0 in the QPC. Both these effects contribute to reduce the number of occupied sub-

bands.

In order to evaluate the conductance G, we assume that in the source and drain reservoirs the electrons fill up states of the Fermi sea up to the respective chemical potential μ_R and μ_L. At $T = 0$, according to fig.1.10, electron states with positive (negative) velocity $v_n = (1/\hbar)[dE_n(k_x)/dk_x]$ are occupied up to μ_L (μ_R). When a small voltage is applied between source and drain ($eV_{sd} = \mu_R - \mu_L$), the net current of electrons through the QPC is carried by the uncompensated states in the energy interval $\mu_R - \mu_L$. At zero temperature, the resulting current, I, is

$$I = e\sum_{n=1}^{N}\int_{\mu_R}^{\mu_L}\frac{1}{2}eN_n(E)v_n(E)T_n(E)dE \tag{1.16}$$

where $N_n(E)$ is the 1D density of states and $T_n(E)$ is the transmission probability of the n^{th} subband. Using the near equilibrium approximation (small V_{sd}) the following statement can be done, $T_n(E) \approx T_n(E_F)$. Furthermore, let us assume that the channel is long enough to prevent the contribution of evanescent waves to the conductance. Then, all the occupied subbands counted in the sum over n must satisfy the condition for the last occupied level, $E_N(k_x = 0) < E_F$. At this point it should be noticed that the product of the group velocity $v_n = (1/\hbar)[dE_n(k_x)/dk_x]$ and the 1D density of states (including both spin orientations) $N_n(E) = 2/\pi[dE_n(k_x)/dk_x]^{-1}$ is energy independent and equal to $4/h$. This takes to the expression for the conductance ($G = I/V_{sd} = eI/(\mu_R - \mu_L)$),

$$G = \frac{2e^2}{h}\sum_{n=1}^{N}T_n(E_F). \tag{1.17}$$

The result of equation 1.17 is known as the two-terminal Landauer formula. Moreover, in the limit that no reflection occurs at both ends of the channel ($T_n = 1$), one has $\sum_{n=1}^{N} T_n = N$ where the number of occupied level at the Fermi energy is $N = int\left[\frac{E_F - eV_0}{\hbar\omega_y} + \frac{1}{2}\right]$. Therefore the Landauer conductance can be simplified as,

$$G = \frac{2e^2}{h}N \tag{1.18}$$

that is a very important and straightforward achievement since it states that the conductance of a QPC is given by the conductance quantum $\frac{2e^2}{h}$

times the number of occupied subbands, where the factor 2 is due to the spin degeneracy of the electron states. The quantization (1.18) is a general result for any shape of the confining potential. The reason is simply that the fundamental cancellation of the group velocity and the 1D density of states holds regardless of the form of the dispersion relation $E_n(k)$.

In real systems there are deviations from ideal conductance quantization. A short review of the main causes of non ideality in the conductance behavior including the annihilation of the quantized plateaus will be given below.
Upon increasing temperature it is found that the plateaus acquire a finite slope. At high temperature some electron states of the next subband become occupied, and not all electron states of the low-lying subbands are fully occupied anymore. The consequent thermal smeared Fermi-Dirac distribution takes the conductance (1.17) to the form

$$\begin{aligned} G &= \frac{2e^2}{h}\sum_{n=1}^{N}\int_0^\infty \left[\frac{df(E_n - E_F, T)}{dE_F}\right] T_n(E)dE = \\ &= \frac{2e^2}{h}\sum_{n=1}^{N} f(E_n - E_F, T) \end{aligned} \tag{1.19}$$

in which $f(E_n - E_F, T)$ is the Fermi-Dirac distribution function. The width of the thermal smearing function df/dE_F is about $4k_BT$, therefore the conductance steps should disappear for $T \geqslant \Delta E/4k_B$ (where ΔE is the subband spacing at the Fermi level). The effect of energy averaging on the quantized plateaus can be appreciated in figure 1.11 where the curves are acquired with increasing temperature. In conclusion, it should be noticed that higher index plateaus are more affected by thermal smearing effect since, as already mentioned, the subband spacing gradually decreases as the gate voltage is swept toward less negative values.

On the opposite temperature limit (at very low temperatures) an oscillatory structure may be superimposed on the conductance plateaus. This phenomenon can have different origins. In general the degree of flatness and the sharpness of the conductance steps depend crucially on the actual shape of the electrostatic potential. As a result, irregularities in the gate geome-

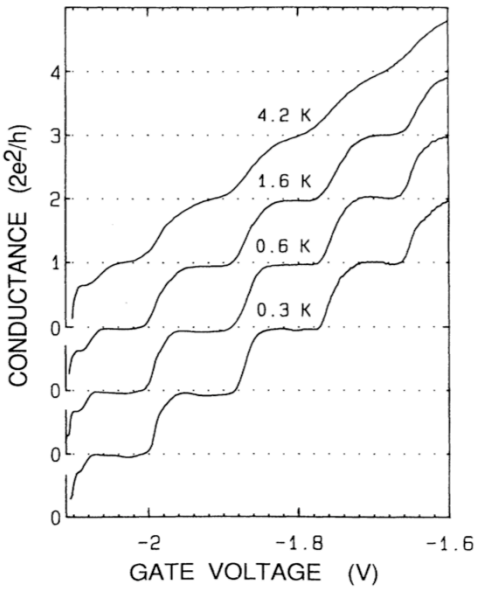

Figure 1.11: Vertically shifted conductance curve at different increasing temperature, from ref.[25].

try, variations in the pinning of the Fermi level at the free surface or at the interface with the gate metal, doping inhomogeneities or charge trapping in deep levels in the gate oxide are some of the uncontrolled parameters that can significantly affect the actual shape of the electrostatic potential [19]. From a quantum mechanical point of view the crucial point which we will focus on is the matching of electron wave function and its derivative at the entrance and the exit of the constriction, i.e. where the narrow point contact widens to the adjacent 2DEG wide regions. Gradual, *adiabatic*, transitions must be distinguished from *abrupt* transitions [26]. The case of adiabatic constriction has been studied by Büttiker [27]. If the constriction width W changes sufficiently gradually, the transport through the constriction is adiabatic, which means that there is no intersubband scattering, and quantization is preserved. Büttiker expands the electrostatic potential near the bottleneck as a quadratic saddle potential, $V(x,y) = V_0 - \frac{1}{2}m^*\omega_x x^2 + \frac{1}{2}m^*\omega_y y^2$, where x is the direction of the current whereas y is the direction of the transverse potential. Quantum mechanical transmission and reflection at the saddle allows for channels which are neither completely open nor completely closed, with a transmission probability T_{mn} (n and m are the incident

and outgoing channel indexes). The transmission probability has been calculated in [28, 29],

$$T_{mn} = \delta_{mn} \frac{1}{1 + e^{-\pi\epsilon_n}} \tag{1.20}$$

where $\epsilon_n = 2[E - \hbar\omega_y(n + \frac{1}{2}) - V_0]/\hbar\omega_x$. Because of the quadratic form of the potential there is no channel mixing, moreover equation 1.20 predicts a transmission probability nearly zero for $\epsilon_n \ll 0$ since $T_{nn} \approx e^{\pi\epsilon_n}$. Conversely, the transmission probability is close to one, $T_{nn} \approx 1 - e^{-\pi\epsilon_n}$ for $\epsilon_n \gg 0$. From ref.[27] it is also argued that well-pronunced steps occur if $\omega_y \geqslant \omega_x$, that is if the transition region for the opening of a quantum channel is small compared to the channel energy separation. The criterion for adiabatic transport has been written also as $dW/dx \lesssim 1/N(x)$, being $N(x) \approx k_F W/\pi$ the local number of subbands [19] and W the width of the channel. Ferry et al.[30] found a similar expression for the transmission coefficient (1.20) pointing out that an 'abrupt' QPC (large value of ω_x) can result in a smearing of the quantized steps exactly like that produced by finite temperature.

On the other hand, a sudden widening of the channel, or change in electrostatic potential, at both ends of the channel will induce a partial reflection of the electron waves. In a one-dimensional model the reflection probability of a potential step [11] is given by

$$R = \left| \frac{k_{x,1} - k_{x,2}}{k_{x,1} + k_{x,2}} \right|^2 \tag{1.21}$$

where $k_{x,1}$ and $k_{x,2}$ are the longitudinal wave numbers inside and outside the channel. The threshold for transmission of the n^{th} subband is $E_F = eV_0 + (n - \frac{1}{2})\hbar\omega_y$. Slightly above the threshold, the internal wave vector $k_{x,1} = \{2m^*[E_F - eV_0 - (n - \frac{1}{2})\hbar\omega_y]/\hbar^2\}^{-1/2}$ is very small, so the reflection probability R of eq.1.21 is close to unit; this means that the n^{th} subband does not yet contribute to the conductance. When the Fermi level is raised respect to the subband edge with increasing the gate voltage, $k_{x,1}$ is also increased and R gradually drops to zero, thus the conductance reaches its quantized value. If multiple reflections occur at both ends of the channel, it is expected to observe also transmission resonances. Assuming equal reflection probabilities at both ends of the channel [25], the conductance of a QPC

can be written as

$$G = \frac{2e^2}{h}\left[N + \frac{(1-R)^2}{1 - 2Rcos(2k_{x,1}L) + R^2}\right] \tag{1.22}$$

where L is the length of the channel. This equation describes the conductance G as being due to N low-lying subbands and the resonant transmission of the upper highest occupied subband. The equation 1.22 preserves quantization of conductance (provided that $2k_{x,1}L = integer \times 2\pi$) though predicts transmission resonances in the transition regions between quantized plateaus. Nevertheless it is seen that an adiabatic constriction improves the

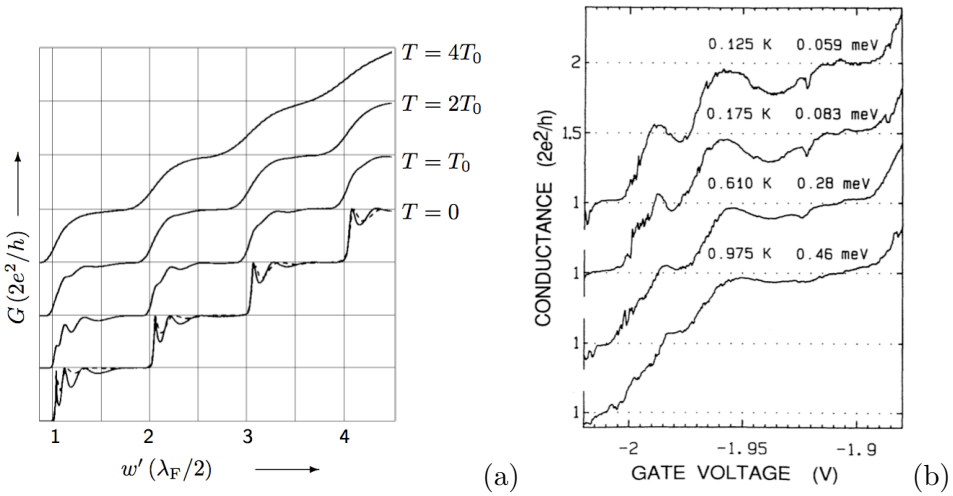

Figure 1.12: Temperature effect on QPC conductance transmission resonances: (a) theoretical results for a QPC with abrupt (rectangular) shape, from [31]. In figure $T_0 = 0.02E_F/k_B \approx 2.8K$. (b) Energy averaging effect on the second quantized plateau of an experimental conductance curve, taken from [25], for temperature ranging from 0.125 K (top curve) to 0.975 K (bottom curve).

accuracy of the quantization but it is not strictly required to observe the effect. Indeed, well-defined conductance plateaus have been found to persist even for abrupt constriction, especially if they are neither too short nor too long. In [19] it is accepted that there exists and optimum length for the observation of a clear quantization, $L_{opt} \approx 0.4(W\lambda_F)^{1/2}$. Indeed for shorter constrictions the plateaus acquire a finite slope due to the transmission of evanescent modes. Instead, in long constrictions transmission resonances could destroy the quantization of conductance.

Oscillations of conductance such as those reported in fig.1.12 can also be

produced by quantum interference processes involving impurity scattering near the constriction due to inhomogeneities in the 2DEG system or in general to random fluctuations of the potential [30],[32]. In practice it is difficult to distinguish geometrical from impurity effects because transmission resonances depend strongly on the shape of the lateral confinement and on the presence of a potential barrier in the constriction.

1.3.1 Magnetotransport in QPCs

In this section the effect of the application of an external magnetic field B on a narrow constriction has been considered. At first the case of a general direction of the vector $\mathbf{B}$ is treated, thereafter, we will discuss the three main orientations of the field with respect to the geometry of the device. We will see that regardless of the electrical or magnetic origin of the transverse modes, the zero-field conductance quantization still persits showing a smooth transition from the zero-field 1D subbands to the magnetoelectric subbands.
Magnetic field acts on the constriction modifying states and dispersion law. In the limit of infinite length, thus neglecting the potential along the x-axis, the Hamiltonian of an electron in a 1D constriction, confined in the z-direction of growth can be written as

$$H = \frac{(\mathbf{p} - e\mathbf{A})^2}{2m^*} + V(y, z). \tag{1.23}$$

In the simplest case, we consider the magnetic field parallel to the direction of motion of conduction electrons, i.e. the x-direction, $\mathbf{B} = (B, 0, 0)$. Thus, using the gauge $\mathbf{A} = (0, 0, By)$, the Hamiltonian becomes

$$H = \frac{p_x^2}{2m^*} + \frac{p_y^2}{2m^*} + \frac{(p_z + eBy)^2}{2m^*} + V(y, z) \pm \frac{1}{2} g_s \mu_B B. \tag{1.24}$$

where $\pm\frac{1}{2} g_s \mu_B B$ term takes into account the effect of interaction of the electron spin with the magnetic field. Assuming that the z-dependence in the Hamiltonian gives the quantized levels originating the 2DEG [33], the eigenvalues from eq.1.24 are:

$$E_n(k_x) = \left(n - \frac{1}{2}\right) \hbar\omega_y + \frac{\hbar^2 k_x^2}{2m^*} + eV_0 \pm \frac{1}{2} g \mu_B B \tag{1.25}$$

where the last term is the Zeeman term. Therefore, the main effect of a parallel magnetic field on the electron transport in a 1D constriction is to lift the spin degeneracy of electrons, thus producing $\frac{G_0}{2} = \frac{e^2}{h}$ equally spaced steps in the conductance.

The second case regards the magnetic field in the z-direction, i.e. perpendicular to the 2DEG plane. Thus, we use the gauge $\mathbf{A} = (-By, 0, 0)$. In this case, since there is a component of the Lorentz force in the plane of motion of electrons, the field competes with the elctrostatic confinement potential and forms hybrid magnetoelectric subbands:

$$E_n(k_x) = \left(n - \frac{1}{2}\right)\hbar\omega + \frac{\hbar^2 k_x^2}{2m} + eV_0 \pm \frac{1}{2}g\mu_B B, \tag{1.26}$$

with $m = m^*\omega^2/\omega_y^2$, $\omega = \sqrt{\omega_y^2 + \omega_c^2}$ and $\omega_c = eB/m^*$. The 1D nature of the subbands is still present, though the dispersion laws are strongly affected by the field. The effective mass appears to be heavier, nonetheless the subbands are parabolic with a energy spacing linearly dependent on the magnetic field ($\hbar\omega$). As a result, as $\hbar\omega$ becomes greater, the energy of the higher-excited subbands exceeds the Fermi level leading to the so-called magnetic depopulation. To understand the way in which the 1D nature of the system is preserved, it should be stressed that the cancellation of the 1D density of states and the group velocity still holds, provided that the number of states N in the constriction becomes, $N_c = int\left[\frac{E_F - eV_0}{\hbar\omega} + \frac{1}{2}\right]$. Previous equation states that at high fields the number of subbands is determined by the combination of the potential barrier V_0 and ω_c, being proportional to $1/B$. Figure 1.13 (a) represents the number of occupied subbands N_c as a function of $1/B$ for several values of the gate-voltage, i.e. the lateral confinement. Figure 1.13 (b) presents experimental results of the perpendicular magnetic field effect on electron transport. It can be noticed that quantization of conductance is preserved though the width of plateaus is widened as the field is made stronger and stronger. This reflects the increase of subband spacing with the increasing of the field. At higher values of the field, the spin degeneracy is lifted in agreement with the Zeeman term of Hamiltonian (eq.1.26), making half-integer plateaus become apparent.

At very high magnetic field values the electronic transport can be explored in the quantum Hall regime. In that case the two-terminal conductance [35]

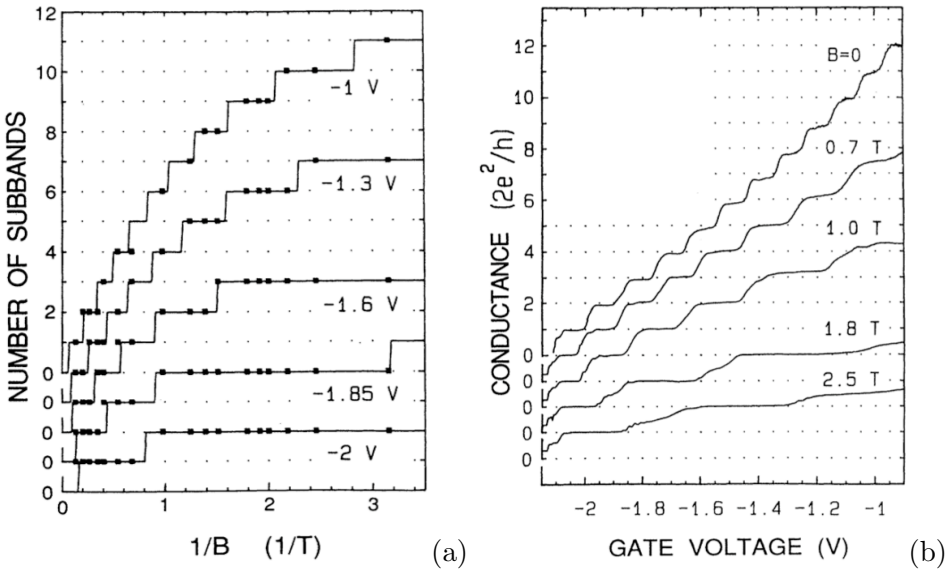

Figure 1.13: (a) Number of occupied subbands as a function of inverse magnetic field obtained at several fixed values of the gate voltage. (b) Quantization of conductance observed at several fixed values of the magnetic field at 0.6 K. Curves have been offset for clarity and taken from [34].

is given by

$$G = N_c \cdot \frac{2e^2}{h}, \tag{1.27}$$

whereas the four-terminal conductance, obtained considering the potential drop across the constriction (μ_L and μ_R in fig.1.14 (a)), can be expressed as

$$G_4 = \frac{N_c N_{wide}}{N_{wide} - N_c} \cdot \frac{2e^2}{h}, \tag{1.28}$$

where N_c is the number of 1D-channels in the constriction and N_{wide} is the number of edge states in the wide 2DEG. Therefore a regular quantization in multiple of $2e^2/h$ is predicted from both eq.1.27 and 1.28 at low fields (large N_{wide}). However, since N_{wide} decreases linearly with $1/B$, as the magnetic field increases, the four-terminal conductance 1.28 is governed by the number of edge states, i.e. Landau levels, in the 2DEG regions. Therefore $G_4 \approx N_{wide} 2e^2/h$ at very high field (and low N_{wide}). Indeed, it can be shown that, for sufficiently large magnetic field that Landau levels are formed, well defined edge states develop near the boundary of a 2DEG system. These edge channels, whose width is of the order of the magnetic length, are 1D

states. There are as many edge states as there are filled Landau levels in the bulk (the central 2D area) of the 2DEG. Figure 1.14 illustrates in a pictorial

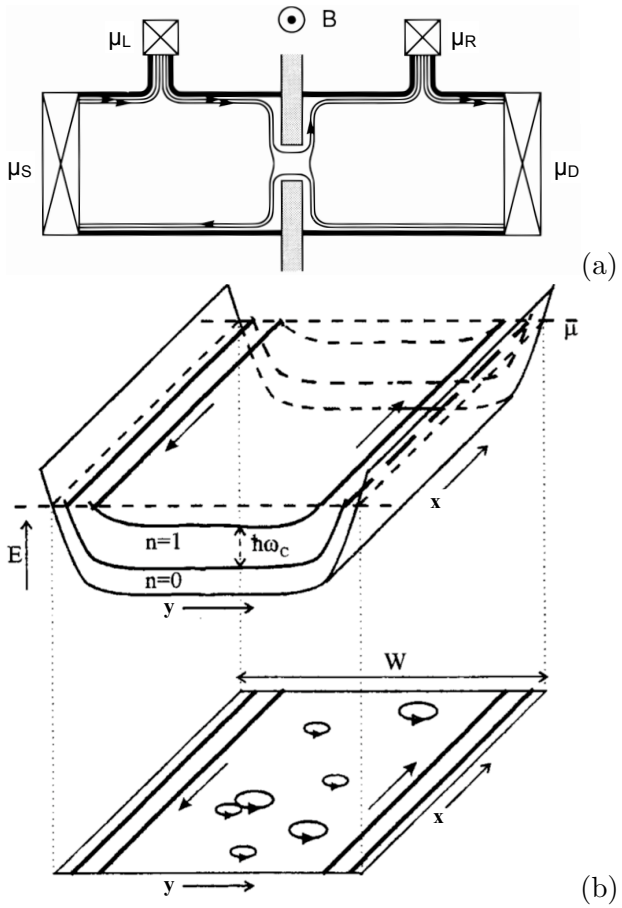

Figure 1.14: (a) Four-terminal geometry device with a a saddle-shaped potential formed by a split-gate (shaded), from ref.[36]. (b) A pictorial view of the edge states in a 2DEG subject to a large magnetic field. The topmost figure shows the system in the energy space while in the lower panel the states are represented in the real space. Note the relation between Landau levels and edge states near the boundary.

way the most important characteristic of the edge states both in the energy space and in real space, showing the relation between the edge states and the Landau levels from which these are formed. This picture also shows that electrons residing in the Landau level states in the center of the system, with their center-of-orbit being stationary, will not contribute to the current.
Lastly, it is considered the case of an in-plane magnetic field, perpendicular to the direction of current, $\mathbf{A} = (0, -Bz, 0)$. It has been demonstrated

in ref.[33] that the magnetic field produces a dramatic evolution of the 1D subbands due to the interplay of the field with the vertical confinement potential given by the heterojunction (along the z-direction). In this case the Hamiltonian is:

$$H = \frac{(p_x - eBz)^2 + p_y^2 + p_z^2}{2m^*} + V(y,z). \tag{1.29}$$

The eigenvalues E_ℓ for the quantized levels of the quantum well depend on the wave vector along the direction of current k_x. In this situation we do not expect a parabolic dispersion, it is found instead

$$E_{\ell,n}(k_x) = E_\ell + \hbar\omega_y \left(n + \frac{1}{2}\right) + \frac{(\hbar k_x - eBz_\ell)^2}{2m^*} + eV_0 \tag{1.30}$$

which describes a shifted parabola whose minimum depends on the magnetic field and z_ℓ, that is the coordinate of the electron wave-function maximum in the z-direction, (see fig.1.15).

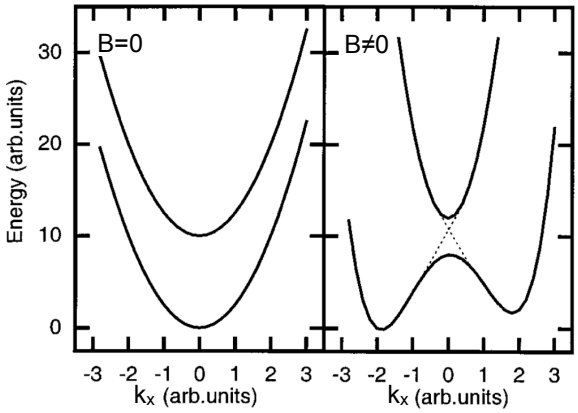

Figure 1.15: Dispersion relation a 1D constriction in absence (left hand panel) and in presence (right hand panel) of an in-plane magnetic field perpendicular to the current. The degeneracies of the crossing parabolas gives gaps in the dispersion law at higher order of the perturbation, leading to the suppression of the conductance quantization, from [33].

So far it has been discussed the effect of high magnetic field on the electron transport of a QPC. In the following the case of lower field intensities will be discussed showing how the magnetic field is crucial in reducing the different scattering mechanisms that suppress the electron mobility.

1.3.2 Suppression of backscattering

In the ballistic regime the existence of a nonzero resistance in a QPC has to be ascribed to the fact that not all the electrons injected in the 2DEG from the source current are transmitted through the constriction, but a fraction is backscattered into the source contact. It can be demonstrated that a relatively weak magnetic field leads to a suppression of the geometrical backscattering caused by the finite width of point contact and that is responsible for the observed negative magnetoresistance at small fields, as reported in fig.1.16. Figure 1.16 shows that the reduction of geometrical

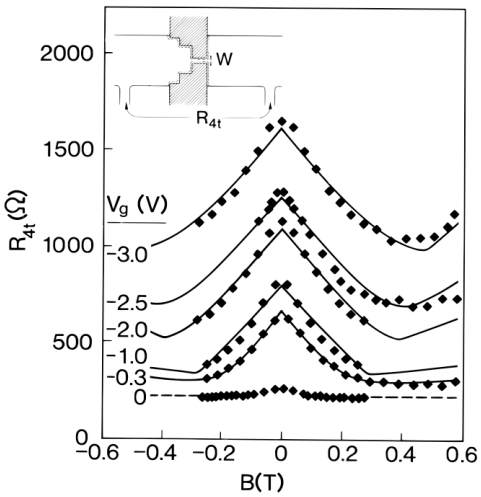

Figure 1.16: Four-terminal longitudinal magnetoresistance, R_{4t} of a constriction for a series of gate-voltages. The inset shows schematically the device geometry, with the two voltage probes used to measure R_{4t}. Taken from [35].

backscattering manifest itself as a negative magnetoresistance in a four-terminal measurement, $R_{4t}(B) - R_{4t}(0) < 0$. However the voltage probes in the experiment have to be positioned on the 2DEG regions, far away from the constriction. The reason is that it is necessary that electrons establish a local equilibrium near the voltage probes so that the measured four-terminal resistance does not depend on the properties of the probes. The negative magnetoresistance is observed in weak magnetic fields once the narrow constriction is defined (for $V_g < -0.3V$ in fig.1.16). At stronger magnetic fields a crossover is observed to a positive magnetoresistance. Until now we have considered the two-terminal resistance, i.e. the inverse of the conductance

G (eq.1.18). As a result, as long as the leads of the voltage probes are sufficiently far from the constriction, at zero magnetic field, the two quantities (R_{2t} and R_{4t}) differ just for the ohmic contact resistance R_c. This picture changes in presence of a weak but finite magnetic field. In a small magnetic field, R_{2t} given by,

$$R_{2t} = \frac{h}{2e^2}\frac{1}{N_{min}}, \tag{1.31}$$

has a weak dependence on B since N_{min} also does. Indeed N_{min} is the number of occupied subbands in the constriction which remains approximately constant as long as the cyclotron diameters exceeds the width of the channel, $2l_c > W$. To understand the origin of the negative magnetoresistance due to suppression of geometrical backscattering, we can consider a constriction like that depicted in the cartoon of fig.1.17. Indeed the effect we are taking into account does not concern backscattering caused by the potential barrier, as that described in section 1.3. In a magnetic field the left- and right-moving

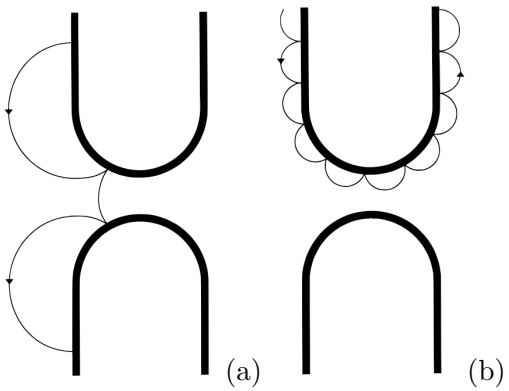

Figure 1.17: Magnetic field reduction of backscattering in a weak (a) and strong (b) field, [19].

electrons are spatially separated by the Lorentz force at opposite sides of the constriction. In fig.1.17 (b) skipping orbits correspond to edge states, thus backscattering of electrons from these states would require scattering across the width of the constriction that is less probable as the cyclotron radius l_c is reduced becoming smaller than the width. In this sense magnetic field suppresses geometrical constriction resistance in the ballistic regime.
The two terminal resistance is the sum of the four-terminal longitudinal resistance R_{4t} and the Hall resistance $R_H = (h/2e^2)N_{wide}^{-1}$ due to the wide 2DEG regions (N_{wide} is the number of occupied Landau levels in the 2DEG

regions). Thus we can write:

$$R_{4t} = \frac{h}{2e^2}\left(\frac{1}{N_{min}} - \frac{1}{N_{wide}}\right). \tag{1.32}$$

We assume for simplicity that the wide regions are not affected by the presence of constriction. Thus, at small fields N_{min} is approximately constant, while $N_{wide} \approx E_F/\hbar\omega_c$ decreases linearly with the field. Therefore equation 1.32 does predict a negative magnetoresistance in this regime ($B \lesssim B_{crit} = 2\hbar k_F/eW$). In the strong-field regime ($B > B_{crit}$) the number of occupied subband in the constriction, $N_{min} \approx (E_F - \Delta E_c)/\hbar\omega_c$, starts to decrease with the field, so that a positive magnetoresistance is restored,

$$R_{4t} \approx \frac{h}{2e^2}\left(\frac{\hbar\omega_c}{E_F - \Delta E_c} - \frac{\hbar\omega_c}{E_F}\right). \tag{1.33}$$

In this discussion on the effects of the magnetic field on the electron transport, two further effects should be mentioned which become relevant in the diffusive and quasi-ballistic regime ($l \lesssim L$). These are *classical size effects* due to the boundaries of the channel and *weak localization* that is a quantum mechanical effect in the diffusive transport. Both mechanisms will be discussed for 2D systems though the effect of reduction of dimensionality will be take into account.

The 'classical size effects' concern the reflection of electrons on the boundaries or the walls of a channel. This reflection can be of two types depending on the boundaries. Either electrons can be scattered and reflected isotropically (*diffusive boundaries*), or the particles are specularly reflected at the wall (*specular boundaries*). In the latter case, since parallel component of the momentum is conserved and the energy does not change (perpendicular component of the momentum changes only its sign), the mobility is not affected by the scattering. The criterion to have specular boundaries is that the roughness size has to be smaller compared to the Fermi wavelength λ_F. It is clear that this requirement can be easily fulfilled in semiconductor 2DEGs whose λ_F varies on the scale of tens of nanometers.

While it is easy to get that specular boundaries scattering does not affect Drude conductivity ($\sigma_0 = n_s e^2\tau/m^*$), diffusive walls act as another scattering source. To evaluate the effect more quantitatively, we consider a second

wall at a distance W. The effective length of the mean free path of electrons will be

$$\frac{1}{l_{eff}} \approx \frac{1}{l} + \frac{1}{W}, \tag{1.34}$$

yielding an effective scattering time, $\tau_{eff} = l_{eff}/v_F$, that reduces the Drude conductivity approximately to

$$\sigma = \frac{n_s e^2}{m^*} \frac{l_{eff}}{v_F} = \frac{n_s e^2 l}{m^* v_F} \cdot \frac{W}{l+W} = \sigma_0 \cdot \frac{W}{l+W}. \tag{1.35}$$

A more accurate expression can be found in ref.[19], nevertheless two limits can be distinguished. If the width is much smaller than the mean free path, $W \ll l$, then $\sigma \approx \sigma_0 \cdot W/l$, in the opposite limit, $W \gg l$, there is a weak dependence on the width, $\sigma \approx \sigma_0 \cdot (1 - l/W)$.
In order to appreciate the influence of magnetic field on the channel boundary scattering let us consider the figure 1.18 that illustrates schematically what happens in the specular and diffusive boundary scattering. In fig.1.18

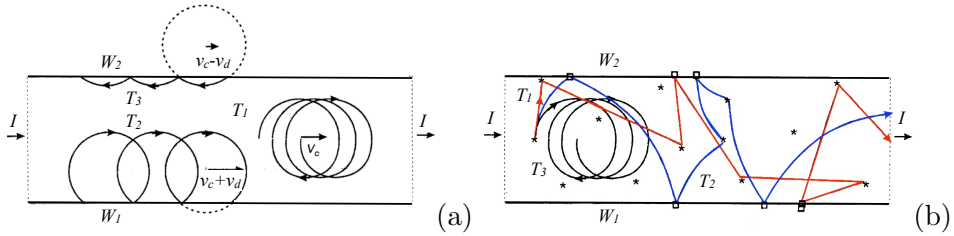

Figure 1.18: (a) Electrons moving in a magnetic field between two specularly reflecting walls W_1 and W_2. (b) Electron trajectories for three different values of the magnetic field between diffusively scattering walls.

(a), the combined effect of the walls induces a zero net effect on the magnetoresistance. Indeed, assuming for example that the distance W is greater than the cyclotron diameter $2l_c$, then trajectory T_1 will not feel the wall. Instead trajectory T_2, being a skipping orbit, has a velocity component v_d determined by the Fermi velocity that increases $(v_d + v_c)$ due to the specular reflection and the circular motion produced by the magnetic field. The result is an increase of the transported current along this wall. On the contrary, trajectory T_3 on the opposite wall W_2 experiments a decreased velocity $v_d - v_c$. The overall effect is that the local increase of the current along wall W_1 is exactly cancelled by local decrease along wall W_2. This

framework can be clearly extended to the narrow channel limit. It can be demonstrated that magnetotransport of a narrow system is not affected by specular reflection at the walls.
Considering now the case of diffusive boundary scattering, trajectories in fig.1.18 (b) represent three characteristic paths, taken at different values of the magnetic field B. Trajectory T_1, at zero magnetic field, demonstrates the effective decrease of the mean free path, as in equation 1.34. Increasing the magnetic field, such that $l_c \sim W$ (trajectory T_2 in fig.1.18 (b)), will enhance the probability of scattering with the wall, thus causing a decrease of the conductivity respect to the zero-field case. Nonetheless, a further increase of the field ($l_c \ll W$) will reduce the cyclotron diameter to a value below the channel width. This imply that majority of the orbits will not experience the walls anymore (trajectory T_3). Thus it is no longer possible to discriminate between specular and diffusive scattering, and only the bulk properties of the channel determine the conductance [19].

So far a classical diffusive effect on the electron transport has been discussed ($\lambda_F, l, l_\phi \ll L$). We focus now on the opposite limit, $\lambda_F, l \ll L, l_\phi$, and consider how quantum interference affects the electron transport. Basically the phenomenon of *weak localization* results from the quantum induced enhanced probability for electrons experiencing several elastic scatterings to return to their initial position. This leads to some kind of electron localization resulting in a reduction of the conductance of the system. The quantum probability of an electron to leave from a position r and to return back to the same position r, is given by the sum all over the possible paths probabilities, including both randomly chosen paths and complementary trajectories (fig.1.19). As a matter of fact the probability for an electron to make a closed path from the position denoted with 0 in fig.1.19 to the same point, considering two time-reversed trajectories (clockwise t_+ {0,1,2,4,3,5,0} and anticlockwise t_- {0,5,3,4,2,1,0}) is

$$\begin{aligned} P_t(0 \to 0) &= A_{t_+}^2 + A_{t_-}^2 + A_{t_+} A_{t_-} cos(\phi_{t_+} - \phi_{t_-}) + A_{t_-} A_{t_+} cos(\phi_{t_-} - \phi_{t_+}) = \\ &= 4A_t^2. \end{aligned} \tag{1.36}$$

In the previous expression $A_{t_\pm}$ and $\phi_{t_\pm}$ are the probability amplitude and the acquired phase-difference for the path $t_\pm$, respectively. As a result the amplitude probabilities of the two time-reversed trajectories are not inde-

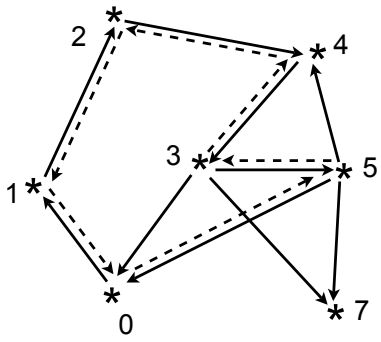

Figure 1.19: Solid line shows randomly chosen electron paths leading from 0 and returning to the same position. The dashed line is the time-reversed path of the {0,1,2,4,3,5,0}.

pendent. In particular, the identical length of the two paths implies that the phase-differences acquired during the travel will be exactly the same. In addition the symmetry of the elastic scattering events dictates that also the amplitude of the two partial waves will be the same ($A_{t_+} = A_{t_-} = A_t$). Summing the contributions of all paths gives,

$$P_{total}(0 \to 0) = \sum_t P_t(0 \to 0) = 4 \sum_t A_t^2 \tag{1.37}$$

where a factor 2 is due to the summation of the two paths for each t, t_+ and t_-, the remaining factor of 2 is a direct consequences of the coherent, in-phase addition of time-reversed paths. In conclusion the phase coherent summation of the time-reversed trajectories in a diffusive medium leads to an increased probability for electrons to return to their initial position. It implies that electrons tend to remain at their initial site thus increasing the resistance. The interpretation of the magnetic field effect is twofold. From a classical point of view, it makes the time-reversed trajectories to become increasingly dissimilar for increasing field strength, as the Lorentz force induced curvature will be different for the two time-reversed paths. Quantum mechanically the magnetic field leads to time-reversal symmetry breaking, indeed it can be demonstrated that weak localization will start to become suppressed whenever the phase difference is $\Delta\phi = \frac{2\pi}{\Phi_0}\pi \left(\frac{l_\phi}{2\pi}\right)^2 B_c$[1]. From this observation a characteristic field B_c can be defined where the suppres-

[1]Quantum mechanically the magnetic field affects the momentum $\vec{k}$ via the vector potential $\vec{A}$ defined as $\vec{B} = \vec{\nabla} \times \vec{A}$, using the minimal substitution $\vec{k} = \vec{k}_0 - e/\hbar\vec{A}$. The

sion starts to become effective $B_c \sim \frac{\Phi_0}{l_\phi^2} = \frac{h}{el_\phi^2}$. Concluding, weak localization can be suppressed by applying magnetic field such that the zero-field time-reversed trajectories become dissimilar in acquired phase due to time reversal symmetry breaking. These considerations are valid for the 2D case, however the effects strongly increase in systems of reduced dimensionality, being the largest in 1D.

1.3.3 Nonlinear conductance in quantum point contact

Non linear transport is achieved when a finite dc bias V_{sd} is applied across the source and drain contact of a QPC [37, 38, 39]. In this circumstance it is expected that the voltage results in a net imbalance between the chemical potential (μ_s and μ_d) of the 2DEG regions respect to the 1D subband bottoms. Assuming a symmetric drop between the two contacts, $\mu_s = E_F + \frac{1}{2}eV_{sd}$ and $\mu_d = E_F - \frac{1}{2}eV_{sd}$, half plateaus appear at conductance values approximately midway between the integer plateaus [40]. This occurs for V_{sd} values such that the number of conduction subbands in the forward and backward direction of current differs by 1. Indeed, it has been demonstrated [38] that at finite (intermediate values of) V_{sd} the quantization is given by $G = \frac{2e^2}{h}\left(n + \frac{1}{2}\right)$. At higher values of V_{sd} integer plateaus are restored as a consequence of the fact that the number of forward and backward subbands differ by 2. Patel et al. [38] presented the first evidence of the half plateaus in the differential conductance with an applied V_{sd}. They reported both the evolution of the differential conductance as a function of V_g for a fixed dc V_{sd}, and the differential conductance taken at constant gate voltage sweeping the dc bias V_{sd}. Plateaus of conductance of $G(V_g)$ curves appear as convergence of different $G(V_{sd})$ traces. An example of non linear differential conductance is reported in figure 1.20, taken from ref.[39], where integer plateaus at zero

---

electron traveling at the Fermi energy from position 1 to 2 along the path $\vec{l}$ acquires a phase $\Delta\phi_{1\to2} = \int_1^2 \vec{k}\cdot d\vec{l} = \int_1^2 \vec{k}_F \cdot d\vec{l} - \frac{e}{\hbar}\int_1^2 \vec{A}\cdot d\vec{l}$. Consider now the time-reversed of the trajectory $\vec{l}$: the resulting closed trajectory implies that the integral should be interpreted as a loop integral enclosing the area S, for the phase it yields $\Delta\phi_{1\to2} = \vec{k}_F \cdot L - 2\pi\frac{e}{h}\oint \vec{A}\cdot d\vec{l} = \vec{k}_F\cdot L - 2\pi\frac{e}{h}\iint \vec{B}\cdot d\vec{S} = \vec{k}_F L - 2\pi\frac{e}{h}\Phi$, where Φ is the magnetic flux through the area S. The quantity h/e is the flux quantum, $\Phi_0 = h/e$. Thus the clockwise acquired phase results $\Delta\phi_{cl} = \vec{k}_F L - 2\pi\frac{\Phi}{\Phi_0}$, instead the counterclockwise phase is $\Delta\phi_{ccl} = \vec{k}_F L + 2\pi\frac{\Phi}{\Phi_0}$. It clearly results that the difference in phase acquired traveling clockwise and counterclockwise along the time-reversed paths is $\Delta\phi(B) = 4\pi\frac{\Phi}{\Phi_0} = 4\pi\frac{BS}{\Phi_0}$. Note that the magnetic field enforces the two time-reversed trajectories to have a different phase difference.

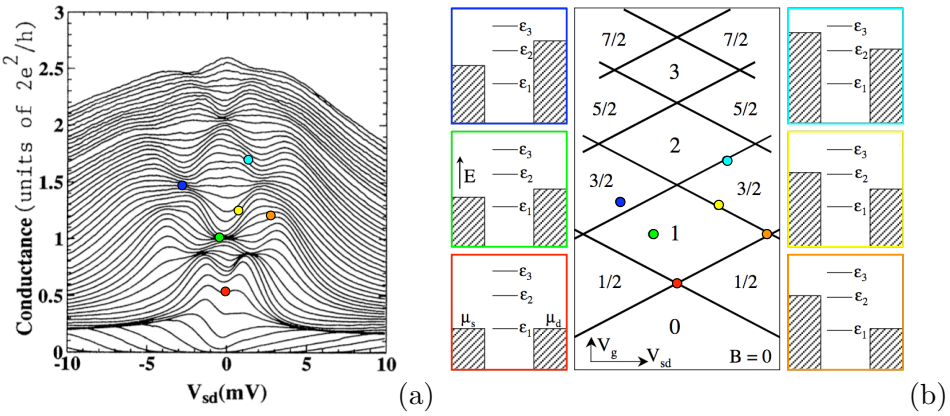

Figure 1.20: (a) Non linear conductance $G(V_{sd})$ as a function of V_{sd} for several gate-voltage values, from ref.[39].(b) Schematic transconductance of a QPC, [41]. Coloured squared lateral panels are the energy diagrams of situations indicated with circles in panel (a) and panel (b).

source-drain bias are followed by half-integer plateaus at finite V_{sd}. From the non linear conductance measurement the energy spacing between different subband bottoms can be estimated. As a matter of fact, from the numerical transconductance, that is the derivative of conductance as a function of gate-voltage ($dG/dV_g = \partial^2 I_{sd}/\partial V_{sd}\partial V_g$), the peculiar diamond shape plot is obtained. A schematic view of a typical transconductance plot is illustrated in the line drawing of fig.1.20 (b) [41]. The diamonds in fig.1.20 (b) represent the zeros of transconductance, corresponding to plateaus in non linear conductance, the black lines represent the maxima of transconductance corresponding to transition between plateaus in the conductance spectra. In the line drawing the different situations marked by colored dots are illustrated in the energy diagrams lateral panels. Each crossing point of the transconductance maxima (like red dot in fig.1.20 (b)) occurs at a gate-voltage value where a new 1D level (ϵ_n) is exactly aligned with the source and drain chemical potentials μ_s and μ_d. This situation corresponds to the onset of each plateau in the linear $G(V_g)$ (red panel of fig.1.20 (b)). Each centered diamond represents a quantized plateau, where μ_s and μ_d both lie between the same two energy bands (green panel in fig.1.20 (b) and green dot in panel (a) of the same figure). Lines which run diagonally upwards from left to right in the transconductance plot indicate that a level is exactly aligned with μ_d (cyan and orange panels). On the contrary those running

downwards from left to right have a band alligned with μ_s (yellow panel). Note that the position (in V_{sd}) denoted with the orange circle gives a direct measure of the subband spacing between first and second energy level in this particular case, $e\Delta V_{sd} = \epsilon_2 - \epsilon_1$ (see orange squared panel in fig.1.20 (b)).

Chapter 2

Experiment

In this chapter we describe the fabrication processes of the devices along with the low-temperature measurement techniques used for the investigation of the transport properties.

2.1 Devices

In this work, two main physical systems are studied: the 2DEGs formed in $Si/SiGe$ and $GaN/AlGAN$ heterostructures were introduced in the previous chapter. The 2DEGs samples were characterized by low magnetic field measurements in standard Hall bars at low-temperature. Further informations about the type of characterization of the 2DEGs will be given in the next chapters related to each system.
In order to fabricate nanostructures and/or to selectively deplete the electron gas in spatially defined regions, it is necessary to transfer a pattern on the two-dimensional system. For this purpose two different techniques have been used for Si and GaN 2DEGs.

Regarding Si-based nanostructures, these are obtained by carving the 2DEG in a double bend-like geometry by using *electron-beam lithography* (EBL) and *reactive ion etching* (RIE) using fluorinated gases. The heterostructures were etched to a depth of 100 nm from the surface. In panels (a), (b) and (c) of fig.2.1 we report, respectively, a schematic of a QPC geometry prior to gate deposition, a side-view schematic of the gated QPC and, finally, a scanning electron micrograph of a complete device. The QPC is

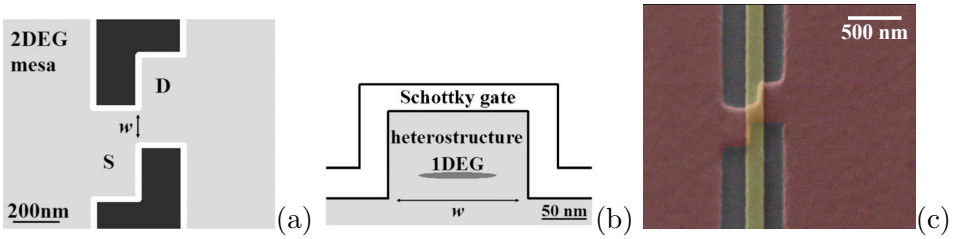

Figure 2.1: (a) Top-view schematics of a QPC geometry (prior to gate deposition). The QPC arises in the narrow conducting channel given by the overlap of the S and D sections. (b) Sideview schematics of the etched QPC with the Schottky gate. (c) Scanning electron micrograph of a QPC device at the end of the fabrication process.

formed by the narrow conducting channel (width $W \approx 160\ nm$ for the QPC reported in fig.2.1) which originates at the junction between two sections (labeled S and D in fig.2.1 (a)) protruding from the outer mesa structure. The S and D sections, 400 nm wide and 200 nm long, act as source and drain leads for the QPC. Due to sidewall depletion caused by the surface states generated by the fabrication process, the constrictions can have an effective width significantly smaller than the lithographic one. A 5/30 nm thick titanium/gold gate was patterned by EBL and lift off in the shape of a 100 nm wide finger gate crossing the etched double bend. The gate was carefully aligned to within 20 nm with the central constriction. The metal folds along the etched semiconductor surface actually forming a triple Schottky gate for the conducting channel (see fig.2.1 (b)) [42]. We have fabricated several widths and slightly different geometry QPCs by using the same approach. As an example, a straight and narrow quantum wire (QW) is reported in fig.2.2.

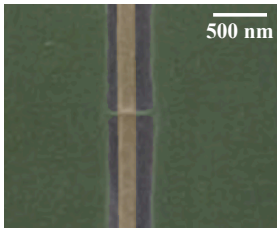

Figure 2.2: Scanning electron micrograph of a QW device consisting of a very narrow channel with a straight metallic strip gate deposited on top.

Etched constrictions have strong lateral confining potentials. In addi-

tion, the surface states completely screen the electric field due to the gate on the lateral walls. As a consequence, acting on the gate voltage, we can vary the carrier concentration without affecting the width of the quantum point contact. Therefore, in our devices we can follow the effect of depleting the 1D channel at a fixed mode energy separation.

As for the GaN nanostructures, a split-gate induced lateral confinement has been chosen. Mesoscopic devices were achieved by using both optical and electron beam lithography. First step is the lithographic definition of ohmic contacts, then a $Ti/Al/Ni/Au$ deposition and annealing at $850°C$ by *rapid thermal annealing* (RTA) follow. Mesa insulation is performed by *ionic implantation* and then the surface is passivated by *plasma enhanced chemical vapor deposition* (PECVD) of a 70 nm thick SiN layer. The SiN layer serves both for protection of the heterostructures and as gate dielectric. Patterned split gates are obtained by depositing the gate metal (Ti/Au) directly on top of the SiN passivation layer in order to get a metal-insulator-semiconductor (MIS) junction. The conductance modulation of the QPC

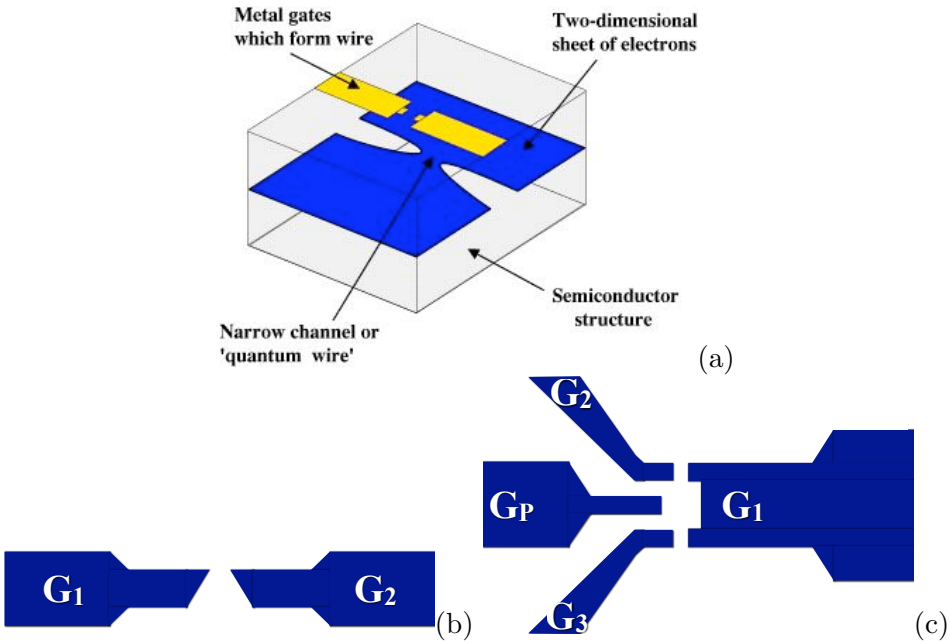

Figure 2.3: (a) Picture representing a split-gate QPC where yellow regions are the metallic gate and blue region is the two-dimentional sheet of electrons. (b) and (c) two schematics of the geometry of devices measured, a QPC formed by wedge-shaped split-gates and SET-type device formed by two QPC barriers, labelled as $G_1 - G_2$ and $G_1 - G_3$.

can be obtained by negatively biasing the split gates to deplete the 2DEG underneath (see fig.2.3 (a)). By increasing the negative voltage beyond the depletion threshold it is possible to extend laterally the depleted regions and to squeeze the 1D channel until the pinch-off condition. The most appealing feature of this confinement technique is that the channel width and electron density can be varied continuously (however not independently) by increasing the negative gate voltage. An additional feature is that by using this configuration also the spacing of modes is gate-dependent.
In figure 2.3 (b) and (c) two schematic representations of the split-gate devices realized on GaN 2DEG are reported. The first is properly a constriction of variable width (W) formed by two facing wedge-shaped split-gates (labelled as G_1 and G_2). The other is defined by the couple of gate electrodes labelled as $G_1 - G_2$ or $G_1 - G_3$ having G_1 in common, providing an electrically defined island for single electron measurements. The third gate (G_P) allows the control of the island potential, capacitively coupling with it. In this thesis we have characterized the single barriers of the devices with geometry like that illustrated in fig.2.3 (c).
A four-terminal layout allowed us to get rid of series resistance due to ohmic contacts and to the portions of two-dimensional electron gas outside the constriction.

All devices measured in this thesis have been fabricated using facilities of the clean room located at the *CNR-IFN* institute.

2.2 Cryogenic systems

In order to observe quantum-mechanical phenomena related to ballistic transport in low dimensional systems it is necessary to perform experiments at cryogenic temperature. We made use of a standard *Heliox* refrigerator by *Oxford Instruments* with a base temperature of 0.38 K (see fig.2.4 (b)). This ^3He cryostat operating principle is illustrated in fig.2.4 (a). It is based on the condensation of ^3He. A pre-cooling stage (1K pot) is the main ^4He bath which is vacuum pumped until reaching a temperature of about 1.3 K. This absorbs the latent heat of condensation of incoming ^3He which thus condensates on the cold surfaces of the thin-walled pumping tube leading to the ^3He pot. The pot starts to cool down and to collect liquid ^3He. Once all ^3He is condensed in the pot, a charcoal pump begins to operate lowering

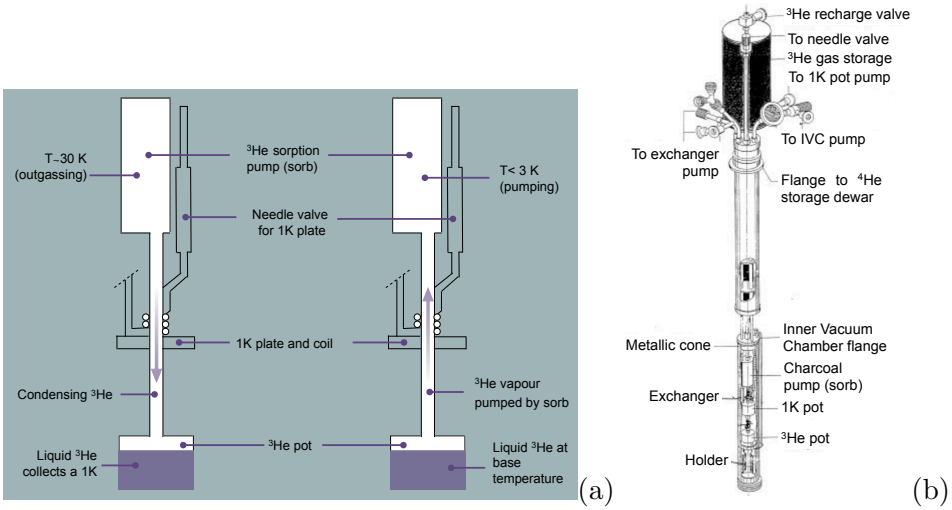

Figure 2.4: (a) Operating principle of an ^3He cryostat. (b) Perspective view of an *Oxford Instruments Heliox*.

further ^3He temperature to ~0.3 K. In this system the ^3He and the ^4He are separated circulation.

In detail, the insert of fig.2.4 (b) is lowered into a ^4He dewar, a small amount of exchange gas is put into the Inner Vacuum Chamber (IVC) in order to speed up thermal exchange until the cryogenic pump has reached the temperature of about 12 K. Then exchange gas is evacuated and the cryo-pump is heated up to 45 K to make all ^3He to be released. A this point the independent ^4He stage has to be activated: liquid ^4He enters the 1K pot through a needle valve and is vacuum pumped to decrease it temperature down to about 1.3 K. The ^3He, cryo-pumped by the sorb, is free to condense in the 1 K plate region of the central tube and runs down to cool the ^3He pot. After approximately 20 minutes most of the gas has been condensed and the ^3He pot is nearly full of liquid ^3He at approximately 1.3 K (see left hand side of fig.2.4 (a)). Subsequently, the heater on the sorb is switched off so that this is cooled to below 10 K and begins to reduce the vapour pressure above the liquid ^3He. The temperature lowers to its base temperature in the ^3He pot (right hand side of fig.2.4 (a)). A temperature controller allows to check thermometers temperature located on the sorb, on the 1K pot and closed to the ^3He pot which is in contact with the sample. Using the cryostat system located at the *IFN CNR* institute a single cryogenic cycle lasts several hours. Then a recycle is necessary to re-condensate

^3He that in the meantime has been pumped back into the sorb. A part of the measurement, especially those involving the use of a magnetic field, has been held in collaboration with the group of Prof. F. Beltram in the *NEST* laboratory of *Scuola Normale Superiore di Pisa*. The cryogenic system used there is an advanced model of that just described. In that case it allows a continuous cycle of about 48 hours. The cryogenic temperature is slightly lower being 0.25 K.

2.2.1 Sample mounting in the cryostat

The samples with the QPC devices are split into small pieces and glued into a chip-carrier using conductive silver paint. The pads of no more than two samples are bonded to the 16 pins chip-carrier which has a copper ground base to favor thermal contact with the sample. The chip-carrier itself is mounted on a copper holder of the cryostat. In order to improve thermal conduction between the carrier and the holder a grease suitable for low-temperature is utilized. Then the holder is screwed on the lower part of the ^3He pot. The overall part is closed with a cylindrical shield and covered with aluminum foils in order to shield high frequency noise and increase reflectivity to reduce heat input. Great care must be paid not to put in contact the aluminum foils with the inside of the IVC. This is indeed the last brass shield whose metallic cones are greased with vacuum grease to ensure seal vacuum.

2.2.2 Electrical connections

Electrical wirings connect the sample pads at low temperature to a room temperature metallic box for the connection with external instrumentation. In order to shield the sample from noise sources at low temperature, different stages of filtering must be installed anchored to fixed temperature. Therefore, CRC filters with a cutoff frequency of 10 MHz have been mounted inside the box containing the connections at 300 K, while resistances of 200 Ω are connected in series to the wires anchored to the 1K pot temperature. In the latest close to the sample, thermocoax cables are used. In addition other 200 Ω resistances are soldered beneath the chip-carrier.

With the aim of lowering the measurement temperature down to 20 mK

a part of my research time has been devoted to the installation, mounting and wiring assembly of a brand new dilution refrigerator (DR) at *IFN-CNR*. The cryostat is the model *Microkelvin 50-100* of the *Leiden Cryogenics BV*. It is a 50 mm insertable dilution refrigerator unit with a cooling power of 100 μW inside the mixing chamber at $\sim$ 100 mK. The development of the cryostat has requested great care in filtering line and hence the invention of a chip-carrier able to accommodate low-temperature filters.
In the following section a brief description of the operating principle of a dilution fridge will be given, whereas for the instructions of use of this particular model we remand to the manual of the refrigerator[1]. In addition attempts done for the operation of the DR in terms of noise filtering and housing of samples will be mentioned.

2.2.3 Principle of operation and installation of a Dilution Fridge

In contrast to helium refrigerators discussed in section 2.2 where the latent heat of evaporation is used for cooling, in a dilution fridge the heat of mixing of the two helium isotopes is used to obtain low temperatures [43, 44] When a mixture of the two stable isotopes of helium is cooled below a critical temperature ($\sim$ 0.87 K) the liquid will eventually separates into two phases, one rich in ^3He, the 'concentrated phase', and the other rich in ^4He, the 'dilute phase'. Because of the lower density, the ^3He-rich liquid floats on top of the heavier ^4He-rich liquid. The concentration of ^3He in each phase is temperature-dependent, fig.2.5. Since the enthalpy of ^3He in the two phases is different, the transfer of ^3He from the concentrated phase into the dilute phase may provide highly effective cooling ($Q = \dot{n}\Delta H$). As the concentrated phase of the mixture is pretty much liquid ^3He and the dilute phase is effectively ^3He gas, while ^4He composing the bulk of the dilute phase is inert and noninteracting, this process can viewed as a 'evaporation' from the 'liquid' phase to the 'gas' phase.
When the refrigerator begins operation the 1K pot is used to condense the $^3He/^4He$ mixture in the dilution unit at a temperature $\sim$ 1.2 K. This is not sufficient for the mixture to form the phase boundary, that occurs only once the temperature falls below the tri-critical point at 0.86 K [43]. This

[1] MCK-50-100/400 on the web site:
http://www.leidencryogenics.com/index.asp?PAGE_ID=21

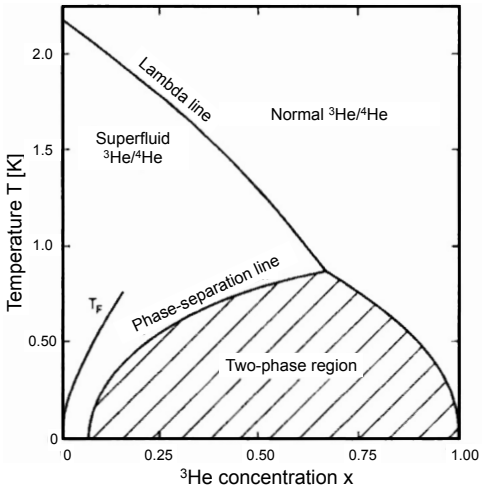

Figure 2.5: Phase diagram of liquid ^3He-^4He mixture at saturated vapor pressure.

cooling is provided by the still; incoming ^3He is cooled by the still before it enters the heat exchangers and mixing chamber [45]. Gradually, the rest of the dilution unit cools to the point where phase separation occurs. In order to reach the base temperature it is important that the ^3He concentration and volume of the mixture are chosen so that the phase boundary occurs inside the mixing chamber and the liquid surface lies in the still (see fig.2.6), otherwise the dilution fridge will not cool to base temperature.
During continuous operation, the ^3He must be extracted from the dilute phase (to prevent saturation) and resupplied to the concentrated phase. The ^3He is pumped away from the liquid surface in the still, where at ~ 0.6 K ^3He evaporates preferentially (1000 times faster than ^4He). ^3He leaving the mixing chamber is used to cool the returning flow of concentrated ^3He in a series of heat exchangers. A room temperature vacuum pumping system is used to remove^3He from the still and compress it before passing it through cold traps (at 77 K) and returning it to the cryostat. The inflowing mixture is pre-cooled by the main helium bath and condensed on the 1K pot. A flow impedance (in the form of a capillary tube) is used to maintain a sufficiently high pressure in the 1K pot region for the gas to condense. The sample is mounted in the mixing chamber (MC) to ensure adequate thermal contact. In figure 2.7 a picture of the MCK50-100 dilution refrigerator utilized is reported: in panel (a) is illustrated the 50 mm stainless tube of the insert,

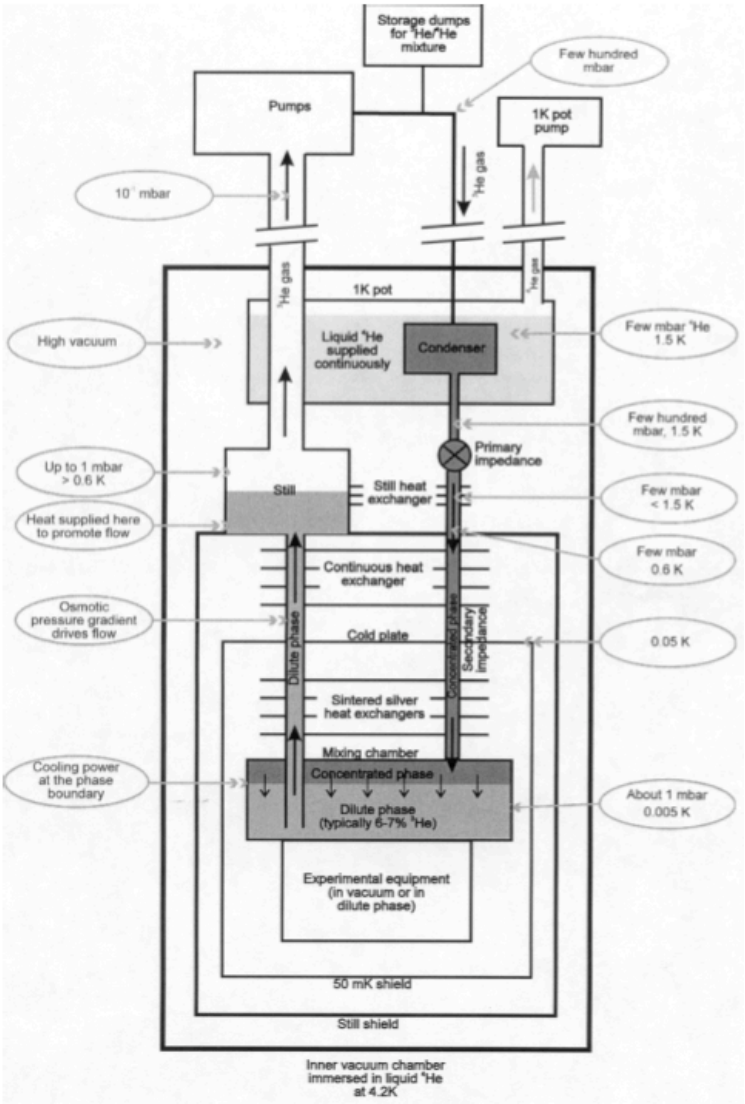

Figure 2.6: Operating principle of a dilution refrigerator.

in panel (b) the unit composed by the 1K pot, the still, the heat exchanger body and the mixing chamber. Finally in panel (c) the head of the insert gone down into the dewar.

The dilution refrigerator has been designed with a two-part external gas

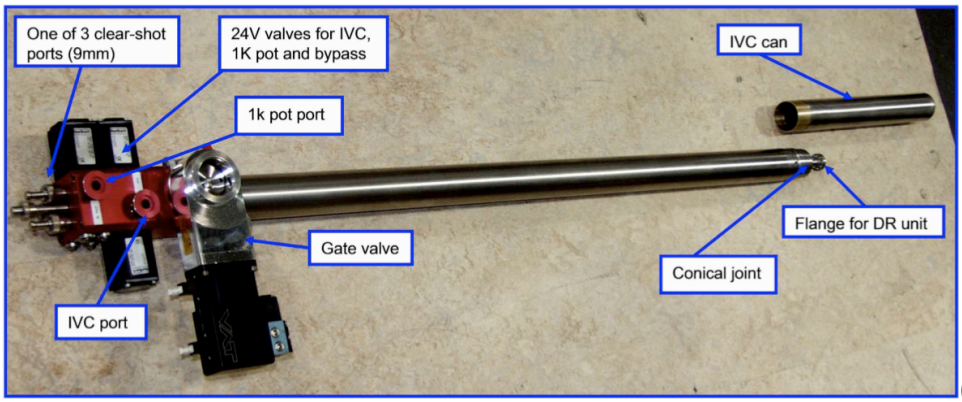

(a)

(b)

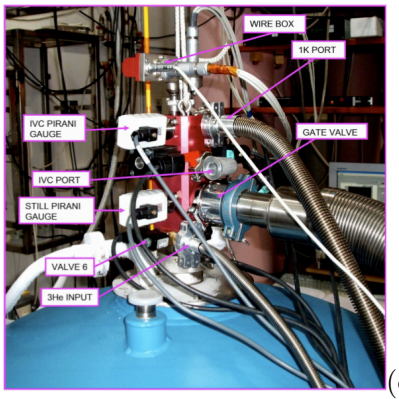

(c)

Figure 2.7: Insert (a), unit (b) and head of the insert (c) of the MCK50-100 dilution refrigerator.

handling system (GHS). One part (the circulation system) serves for to the circulation and handling of the mixture, and the other (the auxiliary system) to auxiliary pumping operations. Both systems are connected to their relevant components on the cryostat and dilution fridge insert by flexible

pumping lines. The gas handling system consists of a stainless steel cabinet made of hollow squares tubes welded so as to make two leak-tight reservoirs (fig.2.7 (b) and (c)). The upper one is used for storing ^3He. It has a volume of 20 *liters*. The lower one is used for the ^4He-rich mixture and has a volume of 70 *liters*. The MaxiGauge vacuum gauge controller placed be-

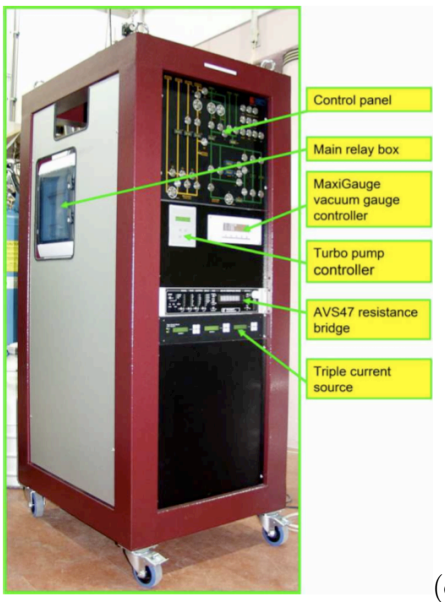

(c)

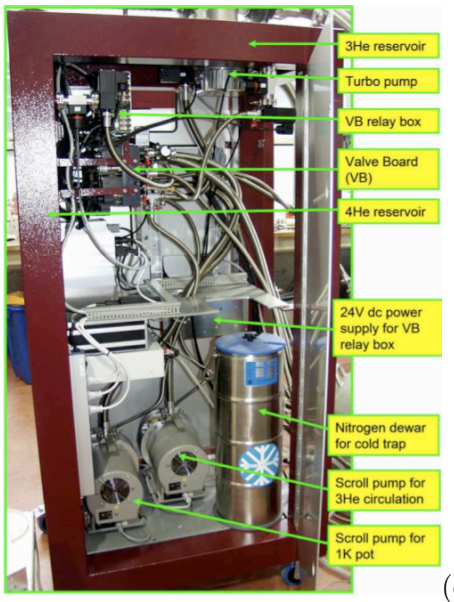

(d)

Figure 2.8: (a) Operating principle of an ^3He cryostat. (b) Picture of an *Oxford Instruments Heliox*.

low the control panel (fig.2.8 (a)) is fitted to measure the still pumping line pressure and the IVC pressure. A resistance bridge (AVS47) allows the temperature reading and control. The Triple Current Source (TCS) has three independent low-noise outputs for heating the sorb-pump, the still and the MC. Inside the GHS (fig.2.8 (b)) a turbo pump and a rotary pump for the circulation of ^3He mixture and an open rotary pump for the auxiliary gas handling system. This pump vents to air, and so should never be opened to areas containing mixture; it is used primarily to pump the 1K pot (pulling ^4He gas from the main bath).

When electrical measurements are performed using a dilution refrigerator, filtering electrical lines connecting a room-temperature apparatus to a cryo-electronic device is of prime importance. Anchoring the lines to elec-

trical heat sinks can help in reducing the noise generated by themselves however it does not prevent the electromagnetic noise from parts at higher temperature from propagating along them. The effective thermalization of the device at a given temperature requires the noise to be sufficiently attenuated by filters. The filtering system must be effective over a wide band spectrum and must be properly thermalized. The main issue is to choose the anchoring temperatures of the filters, taking into account the available space and cooling power at each stage of the refrigerator, together with the noise generated by the filters themselves. The noise of a filter has to be sufficiently attenuated by those of the filters placed closer to the device (at lower temperature) [46, 47]. Because of lack of available space to install filters at anchored temperatures, we placed them at room temperature and at the lowest temperature, i.e. in the mixing chamber. Emi π-filters with a cutoff frequency of 10 MHz and an attenuation of 20 dB have been installed in a metallic box at room temperature where all wires are collected from the DR. Twenty twisted shielded pairs of wires enter the mixing chamber through the bottom part of the unit ending in a connector ring with 40 pins. The mixing chamber consists of a 30 mm diameter conical plug that allows for sample up to 24 mm diameter inside, directly immersed into the mixture. The filtering installation at low temperature has been a quite ingenious deal: a double level chip-carrier with a circular geometry has been designed and realized to house a 24 pins 11×13 mm^2 sample and RC filters directly inside the MC. In figure 2.9 a scheme of an electrical line carrying the signal from

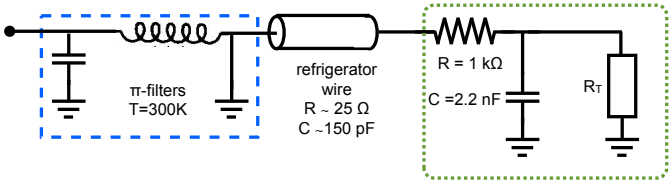

Figure 2.9: Simple scheme of a wire connecting instrumentation at room temperature to the sample at low temperature.

room temperature to the sample R_T at the lowest temperature has been shown. The installed filters are reported in figure.

2.3 Measurement set-up

For the differential conductance measurements, a four-terminal voltage bias configuration has been used. A typical device layout is reported in the SEM picture of figure 2.10: ohmic contacts are labelled as D, S, V^+ and V^-. These are the drain and source contacts for the application of the excitation ($V^{ex} = V_{AC} + V_{DC}$ in fig.2.10) and the measurement of the current, and the two voltage probes for the measurement of the voltage drop across the device, $\Delta V = V^+ - V^-$, indicated as V_{sd} in the following chapters. G_1 and G_2 in fig.2.10 are the gate contacts. The most commonly used measurement setup is that depicted in the figure below. The oscillator output voltage

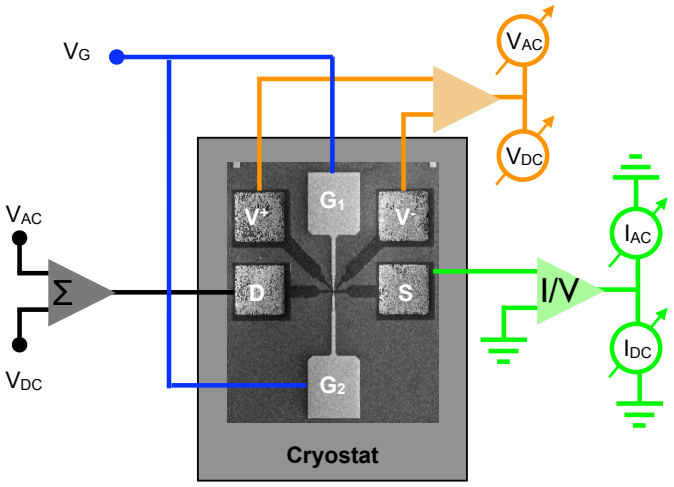

Figure 2.10: Simple sketch of the measurement setup.

V_{AC} of a SR830 lock-in amplifier is divided by 10^4 and then added to a DC voltage V_{DC} generated by a DS360 waveform generator, divided by a factor 10^3. This signal is applied to the drain contact. It is adjusted so that the excitation bias is kept $eV^{ex} < k_BT$. In our experiment $V_{AC} \approx 10\mu V$ at a frequency of 17 Hz. The source ohmic contact is connected to a current pre-amplifier ($\times 10^9$ V/I), providing a virtual ground to the sample, which feeds into the lock-in (SR830) to measure the AC component of the current and into an HP multimeter for the DC component. The gate electrodes are polarized by using a voltage generator, Keithley SCS4200, able to generate bias up to $\pm 200V$ with an accuracy of $5mV$. Indeed quite high and low-noise signals are necessary in the measurements of GaN-based QPCs,

due to the high pinch-off voltages. Gates are biased relative to the source contact. The additional voltage probes allows for the measurement of the the voltage drop across the device, $V_{sd} = \Delta V$. A second lock-in (SR530) frequency locked to the first and another DC voltmeter collect the amplified ($\times 10^2$) signal, $\Delta V = V_{DC}^{mis} + V_{AC}^{mis}$ (see fig.2.10). Thus, this is the device conductance, $G_{dev} = I_{AC}/V_{AC}^{mis}$.
To achieve a good signal quality especially at low temperatures, great care has to be taken with filtering of electrical signals. As already mentioned, all signal lines enter the cryostat only through π filters located at room temperature stage (with a cut off frequency of about $10MHz$). The voltage dividers have to be mounted closed to these filters. Additional RC filters have been applied to the extremely noise sensitive lines connecting the gate electrodes. These RC filters have a cut-off frequency of $\sim 8Hz$. In fig.2.11 a scheme of the filtering box and the AC+DC adder-divider box used are reported. To prevent eddy current, the ground of the box containing BNC

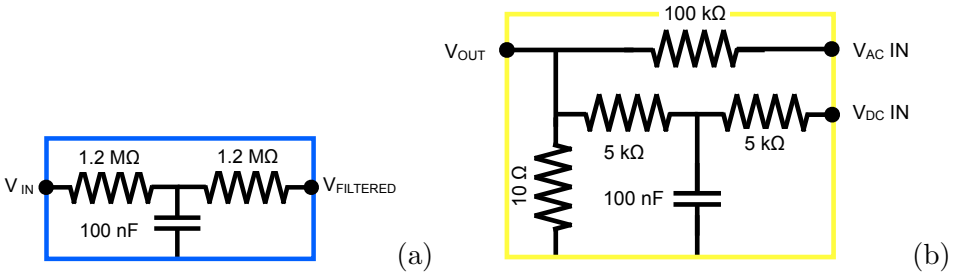

Figure 2.11: (a) Low-pass filtering box used for gate lines, the cutoff frequency is $\sim 8Hz$. (b) AC+DC adder-divider box: the voltage output is $V_{OUT} = \frac{V_{AC}}{10^4} + \frac{V_{DC}}{10^3}$. The DC component is filtered ($f_{cut} \sim 2kHz$).

plugs must be in electrical contact with the cryostat itself and with the rack of instruments. In addition, in order to shield rf-noise a metallic web surrounding both the cryostat and the $L - He$ dewar is used. Lastly battery powered amplifier and plastic o-ring connecting the rotary pumps to the cryostat are implemented to avoid the $50Hz$ signal. About filtering in the cryostat at base temperature refer to previous sections.

Before the measurements at 0.3 K, a number of measurement tests have to be done at 300 K and then at 4.2 K. A rapid check of the ohmic contacts and of the gate leakage current is carried out at room temperature. At 4.2

K two- and four-terminals DC IV characteristics of the device are obtained. The gate leakage current is measured in the whole interval of operation of the gates. If all these tests pass, a preliminary AC differential conductance measurement is done.
During the cool down of devices from room temperature, grounding cups are put on the ohmic and gates contacts.

Chapter 3

Conductance in *Si*-based etched quantum point contacts

In this chapter we report results and discussion of the electrical characterization carried out on several etched-Si-based nanostructures. The conductance behaviour has been analyzed as a function of the source and drain bias voltage, V_{sd}, as well as of the gate voltage, V_g, and the external magnetic field, B. We report the investigation of the transport properties of the 2DEG for one of the samples studied. Both classical and quantum Hall effect at low temperature were exploited.

3.1 Introduction

Silicon nanostructures are excellent systems to develop semiconducting nanodevices [48, 49, 50, 51, 52, 53] extremely important for quantum computing applications due to several aspects [54]. Firstly, scalability and controllability of Si devices made silicon the most relevant electronic material. Moreover, silicon is a very attractive object of study for quantum dot realization thanks to the longer intrinsic spin coherence time compared to gallium arsenide. In addition the availability of the zero-spin Si isotope allows the suppression of decoherence caused by the coupling of electrons with nuclear spin [55, 56, 1].

Nevertheless, the presence of multiple valleys in silicon conduction band is the major source of decoherence for defined spin-states in Si-quantum dots [57]. The $Si/SiGe$ two-dimensional electron gas (2DEG) differs from the $AlGaAs/GaAs$ one by the presence of multiple valley minima. Indeed, in a Si channel grown on a cubic $SiGe$ under biaxial strain, there are two equivalent minima of the conduction band. As a consequence in an independent electron picture and double valley degeneracy, conductance quantization in units of $4e^2/h$ is expected. Indeed, $4e^2/h$ quantization was reported in early investigations [58, 59, 60].

In this chapter Si-based 2DEGs and devices are studied. Firstly, we will report low-field measurement results, giving the relevant parameters of the 2DEGs, and the measurements at high magnetic fields. Then, we will report transport characterization of devices with different geometries and sizes through the measure of the differential conductance. Afterwards we will focus on the behaviour of the conductance of a quantum point contact in the low-G regime ($G < 4e^2/h$) and of a straight nanowire. We will report measurements of the linear and non linear differential conductance in presence of a perpendicular and parallel magnetic field at temperature of $\sim 260\ mK$.

3.2 Samples

Table 3.1 reports the results of the electrical characterization of the 2DEGs used in terms of mobility and sheet density as obtained from classical Hall effect measurements at $T = 15\ K$. Low-field analysis has been performed in the $(15 \div 300)\ K$ temperature range. However, it is expected that the carrier density remains approximately constant below about $25\ K$ (see fig.4.1) while the mobility increases of about 30-40% lowering the temperature down to $300\ mK$.

To compare classical Hall effect with quantum Hall effect carried out at low temperature ($\sim 260\ mK$), we report a measurement of the longitudinal ρ_{xx} and transverse ρ_{xy} resistivity performed on Sample A (fig.3.2). From the analysis of the period of Shubnikov de Haas oscillations as a function of $1/B$ a value of $9.4 \cdot 10^{11}\ cm^{-2}$ has been found, in agreement with low field measurement [61]. In correspondence of the minima of longitudinal resistivity ρ_{xx}, Hall resistivity ρ_{xy} exhibits some inflections that correspond to $h/\nu e^2$

	n_{2D} (cm^{-2})	μ (cm^2/Vs)
Sample A	$9.4 \cdot 10^{11}$	$1.5 \cdot 10^4$
Sample B	$9.2 \cdot 10^{11}$	$1.0 \cdot 10^4$
Sample C	$9.8 \cdot 10^{11}$	$2.7 \cdot 10^4$

Table 3.1: Parameters extracted from classical Hall effect measurements at $T = 15\ K$.

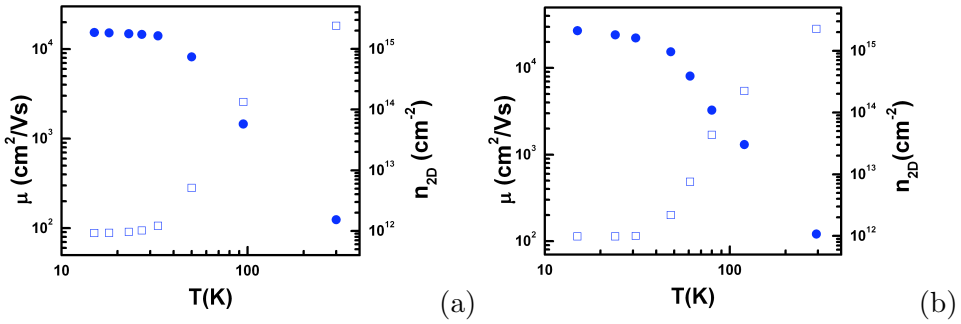

Figure 3.1: (a) Mobility μ and (b) carrier density n_{2D} as a function of temperature for Sample A and Sample B, respectively.

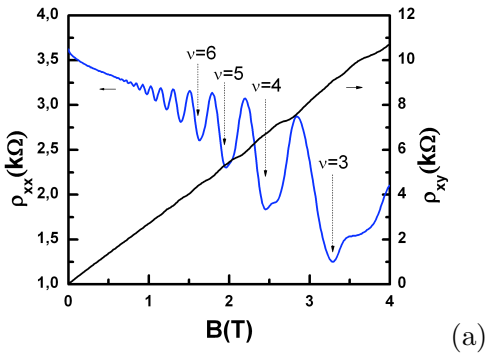

Figure 3.2: (a) Longitudinal and transverse resistivity as a function of magnetic field. Analysis of the period of SdH oscillations gives a value of $9.4 \cdot 10^{11}\ cm^{-2}$ for the electron density. (b) Longitudinal conductivity against filling factor ν.

values of the resistance, where ν is the Landau level number. Quantum lifetime τ_q can also be estimated from oscillation amplitude dependence versus magnetic field at a given temperature [62]. Since theory predicts for the amplitude of the SdH oscillations the relation $\Delta\rho_{xx}/\rho_0 = 4\chi(T)exp(-\pi/\omega_C\tau_q)$, the plot in logarithmic scale of the quantity $\Delta\rho_{xx}/4\chi(T)\rho_0$ against $1/B$ should give a straight line whose slope is related to the single particle lifetime, τ_q, and whose intercept at $1/B = 0$ is expected to be zero. Extracting the relative amplitude of oscillations of ρ_{xx} as a function of the inverse magnetic field $1/B$ (*Dingle plot*) a linear dependence has been found (fig.3.3). From the linear fit slope we calculated the quantum scattering time τ_q to be 0.91 ps.

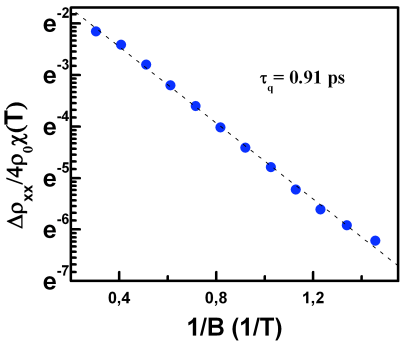

Figure 3.3: Dingle plot: relative oscillations amplitude as a function of $1/B$. Linear fit gives a quantum scattering time of 0.91 ps.

The ratio of transport scattering time (τ_t) and quantum scattering time (τ_q) has been used in the study of semiconductor transport to discriminate among various scattering mechanisms. This ratio gives the measure of what kind of scattering mechanism is predominant: large or small angle scattering. Indeed, if $P(\theta)$ is the probability density that an electron is scattered through an angle θ, being

$$\frac{1}{\tau_t} = \int P(\theta)(1 - cos\theta)d\theta, \tag{3.1}$$

the presence of the angular weighting factor $(1 - cos\theta)$ enhances the contribution of large angle scattering events over small angle scattering [63]. On

the other hand, quantum scattering rate is

$$\frac{1}{\tau_q} = \int P(\theta) d\theta. \tag{3.2}$$

As the weighting factor is not included, all the scattering angles are counted equally [64]. The ratio τ_t/τ_q is larger than unity in systems where small angle scattering dominates whereas it is nearly unity in systems where the scattering is isotropic. Thus, for high-quality 2DEG, ratio of τ_t/τ_q can reach 100 compared to that found in lower mobility samples in which the ratio is observed to approach unity. In our 2DEG, we have extracted τ_t from low field mobility, $\tau_t = \mu m^*/e$, to be about 1.6 ps. It follows that the ratio τ_t/τ_q is 1.8, suggesting that large angle scattering is a relevant mechanism in limiting mobility.

3.2.1 Nanostructures

Several etched-Si nanostructures were investigated during the thesis work consisting in straight narrow wires and point contacts. The ones that will be considered in details here are a $\sim$ 40 nm-wide straight quantum wire on sample A, namely QW, reported in the SEM picture of fig.3.4 (a) and two QPCs resulting from the narrow conducting channel that originates at the square-shaped 2DEG mesa protrusions, namely QPC1 on sample B and QPC2 on sample C, shown in fig3.4 (b) and (c), respectively.

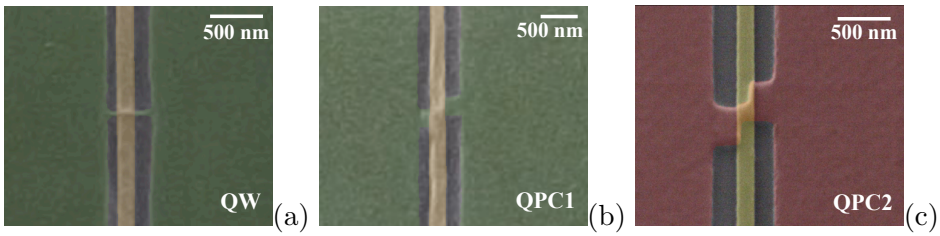

Figure 3.4: (a) Quantum wire (QW) 450 nm long and $\sim$ 40 nm-wide with a $\sim$200 nm wide metallic gate realized on sample A. SEM pictures of the two constrictions (b) QPC1 and (c) QPC2 resulting from the geometrical overlap of two square shaped 2DEG regions, realized on sample B and sample C, respectively. The lithographical width of the metallic gate strip is (b) $\sim$180 nm and (c) $\sim$100 nm.

3.3 Quantum transport is *Si*-based nanostructures

In the present section we report main results obtained from the study of mesoscopic transport of devices in fig.3.4. We will show that a standard quantization of conductance manifests in the quantum wire (QW) of fig.3.4 (a) at a temperature of 4.1 K, whereas upon lowering the temperature, effects going beyond the model of non interacting electrons in a 1D system appear. Then, we will deepen the investigation of the low conductance region of the other two devices (i.e. below the value $G \approx 4e^2/h$), focusing on the reproducible behaviors and their origins.

In fig.3.5 the linear conductance of the QW as a function of V_g is presented at three different temperatures, i.e. $T = 0.26, 2$ and 4.1 K, from right to left. In this device we were able to span a large interval of conductance, up to $G = 4 \cdot G_0$ ($G_0 = \frac{2e^2}{h}$). The curve at the highest temperature shows

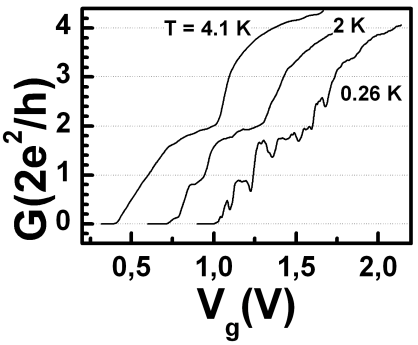

Figure 3.5: Linear conductance QW taken at different temperatures. Curves are horizontally shifted.

two prominent conductance plateaus at values $G = G_4$ and $G = 2 \cdot G_4$, where $G_4 = 4e^2/h$. Indeed a quantization of conductance in units of G_4 is expected for a 1D system in a silicon 2DEG due to the twofold valley degeneracy present in the conduction band [65, 66]. Upon lowering the temperature a fine structure emerges in the linear conductance. As a matter of fact in the 2 K curve a quantization in units of $G_0 = 2e^2/h$ is found: two clear conductance plateaus develop at $1 \cdot G_0$ and $2 \cdot G_0$. Third plateau is missing, while a large rounded plateau is present at $4 \cdot G_0$. At $T = 0.26$ K peak-like and dip-like structures largely affect the linear conductance curve,

superimposing to the conductance spectra taken at $T = 2\ K$. These features, thoroughly investigated in the following sections, are attributed to transmission resonances or interferences due to multiple reflections occurring at both ends of the channel due to the abrupt interface between the 1D-2D transition regions of the confining potential (discussed in the first chapter) or caused by multiple scattering from impurities. Despite the presence of peaks and dips in the G trace, the formation of a G_0 plateau in the lowest temperature ($T = 2$ and $0.26\ K$) conductance curves is apparent. As we will demonstrate in the following section, we interpret these structures as a manifestation of conductance quantization in units of $G_0 = 2e^2/h$ and ascribe these findings to a complete removal of valley degeneracy.
In figure 3.6 we report linear conductance spectra for two quantum point contacts shown in fig.3.4 (b) and (c) versus gate voltage for various temperatures increasing from from right to left: $T = 0.4$, 0.6, 0.9, 1.4 and $1.6\ K$ in panel (a) of fig.3.6 and $T = 0.26$, 0.5, 0.9, 1.5 and $4.1\ K$ in panel (b). All

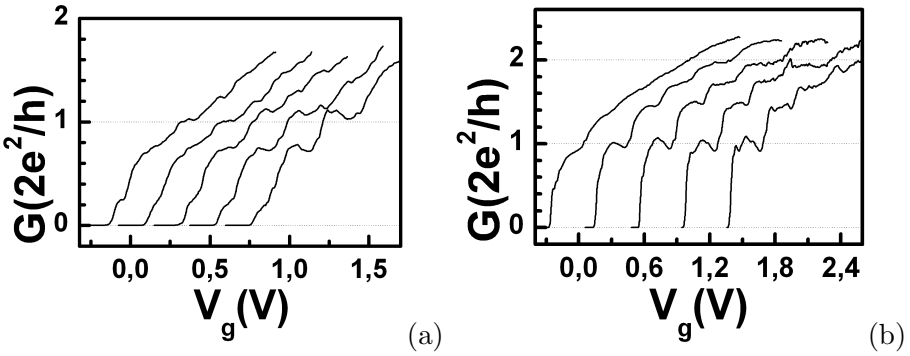

Figure 3.6: Linear conductance of QPC1 (a), QPC2 (b) taken at different temperatures. All curves are horizontally shifted.

curves reported in fig.3.6 are horizontally shifted and show G values lower than $4e^2/h$, i.e. below the conductance quantum expected for a quantum device realized in a tensile Si channel. However none of these exhibit a clear quantization in units of G_4 ($G_4 = 4e^2/h$). Beyond the unexpected behaviour, it is noteworthy the presence of broad peaks in the G traces of fig.3.6. This behaviour is evident especially at low temperatures as the characteristic peak-like structures are energy averaged by increasing temperature [25, 67, 68]. Similarly to the case of the measure reported in fig.3.5, the appearance of these structures has to be attributed to transmission res-

onances caused by multiple reflection occurring at the entrance and exit of the channel. In detail fig.3.6 (a) shows two structures at about $V_g = 0.1\ V$ and $V_g = 0.35\ V$ (lower temperature curves have been shifted) that have been interpreted as interferences due to electrons geometrical backscattering on the basis of magnetic field measurements discussed later on; both structures belong to the first quantized conductance plateau (see $T = 1.4\ K$ and $T = 1.6\ K$ curves). Regarding linear conductance of QPC2 (fig.3.6 (b)) as temperature is raised the resonance structures are smeared out and the formation of a G_0 plateau is evident. Following steps are less conspicuous. It is worth noting that all acquired curves in different cooldowns have some characteristic reproducible features which are imputed to intrinsic mechanisms, like the geometrical backscattering due to the confining potential. On the other hand there is a fine structure which varies among different cooldown. This is contingent on the peculiar charge distribution under the gate electrode, indeed it depends on the actual potential profile due to the presence of trapped charge under the gate or to a pinning of the Fermi energy due to the presence of accidental impurities.

In the following we will focus on the conductance behaviour of two particular devices, the QPC1 and the QW. Measurements of linear and non linear conductance and their evolution with an applied magnetic field will be illustrated.

3.3.1 Conductance of Quantum Point Contacts

Linear and non linear conductance

The main features of conductance of QPC1 shown in fig.3.4 (a) has been reported in fig.3.7 (a) and (b) for $G < 2 \cdot G_0$ ($G_0 = 2e^2/h$), where the typical curves of linear G versus V_g and non linear G versus V_{sd} taken at $0.3\ K$ are shown. We have already mentioned the reproducibility of the key characteristics of the G traces on several cooldowns: plateau-like and peak-like structures manifested at conductance values that changed slightly in different thermal cycles. Now we focus on the reproducibility of curves from run to run of the same thermal cycle.
In fig.3.7 (a) two sets of linear conductance data are reported as a function of the gate bias V_g. The curves were acquired in the same thermal cycle: the 'sweep-up' traces by sweeping the gate voltage from pinch-off toward

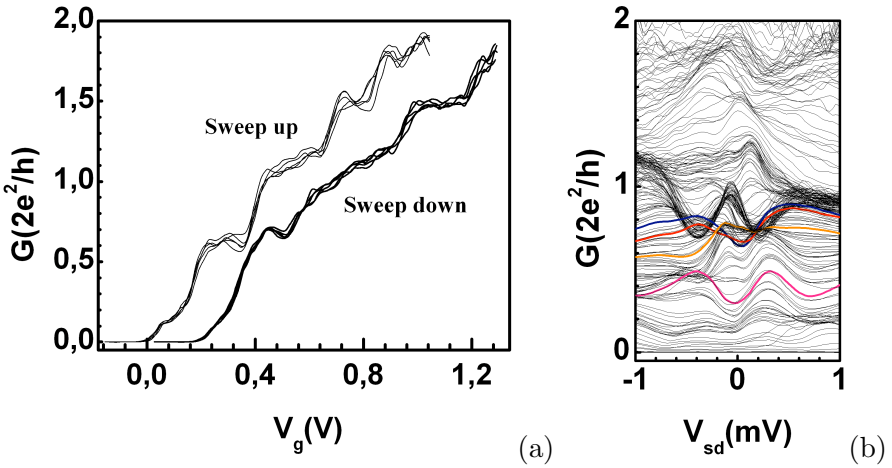

Figure 3.7: (a) Linear conductance curves as a function of the gate voltage. The measurements were acquired in the same thermal cycle by sweeping the gate voltage towards positive values from pinch-off (sweep-up) or in the opposite direction (sweep-down). (b) Non linear conductance versus source-drain bias and gate voltage. The gate voltage has been swept from negative towards positive values (sweep up). Coloured line curves correspond to values of V_g defined in the text.

positive values and the 'sweep-down' curves by sweeping the gate in the reverse direction. For clarity all the sweep-down curves are shifted horizontally toward positive gate voltage. Inspection of the curves show that the main features are quite reproducible, while details change from run to run. Notice, however, the variation of the relative height of the first two steps as compared to a different cooldown shown in fig.3.6 (a). Persistent features are represented by several step-like structures, on which peak-like fine structures are superimposed that somewhat change from run to run. Moreover, shape and conductance values of the peculiar features markedly depend on the sweeping direction. For sweep-up acquisition the curves present well developed structures at about 0.65, 1.1, 1.5 and 1.8 G_0 conductance values; in the sweep-down curves the 0.65 G_0 and 1.5 G_0 structures are still well visible while the structure around 1.1 G_0 conductance is smoother. Regardless the sweeping direction in all the G curves a shoulder at 0.15 G_0 is present, which is smoother in the sweep down traces. All the G measurements reported afterward were acquired by varying the gate voltage always in the sweep up direction.

A further noteworthy finding is the appearance of a zero bias anomaly (ZBA) in the differential conductance G as a function of source-drain voltage

V_{sd}, as shown in fig.3.7 (b) for values of the gate bias ranging from -0.04 V to 1.105 V. It is seen that in the central region a fine structure is present, a ZBA whose lineshape varies strongly upon changing V_g. The behavior as a function of V_g can be summarized as follows. In the V_g range corresponding to the the development of the first prominent step in the sweep-up conductance curves of fig.3.7 (a), the differential conductance evolves exhibiting first two narrow peaks positioned almost symmetrically around $V_{sd} = 0$ ($V_g = 0.16$ V pink line curve), then a narrow peak, centered at $V_{sd} \sim -0.1$ mV ($V_g = 0.3$ V orange line curve). Then, for V_g values corresponding to the minimum between the first and second step of fig.3.7 (a), red and blue line curves, the central peak tends to disappear. Concomitantly with the development of the second step in fig.3.7 (a) the peak centered at $V_{sd} \sim -0.1$ mV increases again becoming a prominent one and shifting towards -0.07 mV. A the same time the curve acquires a symmetric lineshape. The peak weakens again for V_g values corresponding to the end of the second step in fig.3.7 (a).

Deviations of the experimental conductance from canonical quantized values [69, 70, 71], the presence of additional structures in the G curves [25, 72], the missing of plateaus [73] and *ZBA* [7, 74] have been observed and reported in the *GaAs* systems. Some effects appear intrinsic to mesoscopic devices, as for example the additional plateau below G_0, the so-called *0.7 anomaly* [72, 75, 76], whose microscopic origin is still being debated although a general consensus is forming in favour of explanations in terms of many-body effects. Other features, instead, have been related to extrinsic mechanisms such as an asymmetric distribution of the electron density in the two sides of the QPC [73] or scattering events [25]. Indeed scattering or partial reflection of electron waves, due to defects or irregularity in the potential or reflection at both ends of the conducting channel, produce both transmission resonances in the G curve and a lowering of the conductance. It is well known that the application of an external magnetic field can give precious information on the scattering mechanisms affecting the conductance and on the origin of the structures present in the G curves. To that end, magneto-transport data in presence of both perpendicular and parallel magnetic field were acquired and presented in the following.

Perpendicular magnetic field

In fig.3.8 the linear conductance is reported as a function of the gate voltage in the V_g interval corresponding to the first two prominent structures in fig.3.7 (a), for perpendicular magnetic field varying in the $(0 \div 8.8)\ T$ range, panel (a), and $(0 \div 2)\ T$ range, in the particular of panel (b). Following

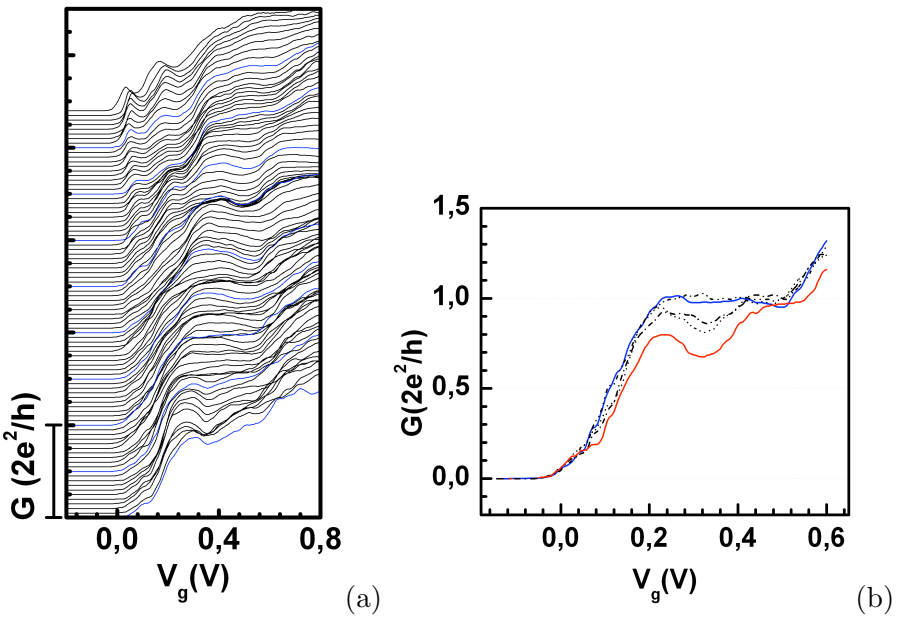

Figure 3.8: Linear conductance as a function of the gate voltage acquired in perpendicular magnetic field. (a) Conductance curves for magnetic field ranging from 0 to 8.8 T with steps of 0.1 T, from bottom curve to upper curve. Curves are vertically shifted for clarity. Blue line curves correspond to magnetic field intensities of 0, 1, 2, 3, 4, 5, 6, 7 and 8 T. (b) The reported curves are relative to magnetic field equal to 0 (red line), 0.5, 1, 1.5 and 2 T (blue line).

procedure used in ref.[58] four-terminal conductance curves were corrected for a suitable series resistance in order to take into account the influence of edge states propagating along the 2D regions [19]. A magnetic field dependent, gate voltage independent background resistance has been chosen to obtain the expression for the quantization of conductance. From ref.[19], $R_{4t} = \frac{h}{2e^2}\left(\frac{1}{N_{min}} - \frac{1}{N_{wide}}\right)$, where N_{min} is the number of occupied magneto-electric subbands in the constriction and N_{wide} is the number of occupied Landau levels in the 2DEG wide regions. Since we have previously measured the carrier density n_{2d}, we were able to determine, for each value of explored magnetic field, the number N_{wide} of the occupied Landau levels

(from an interpolation of the function $N_{wide} = \frac{h}{4e}\frac{n_{2d}}{B}$) and hence the value of the background resistance $R_b = \frac{h}{2e^2}\frac{1}{N_{wide}}$ to be added to R_4 in order to obtain the quantized resistance $R_2 = \frac{h}{2e^2}\frac{1}{N_{min}}$.
From fig.3.8 (b) it is evident that, upon increasing the magnetic field, a filling and a consequent flattening of the conductance curves takes place. For magnetic field intensities higher than about 1 T a single conductance plateau at $G = G_0$ is present and remains constant up to $B = 3.5$ T (see fig.3.8 (a)). After that value of magnetic field, a shoulder in the conductance curve below the first G_0 plateau occurs evolving in a $0.5G_0$ plateau as the magnetic field is increased. Negative magnetoresistance and recovery of flat quantized conductance plateaus in perpendicular magnetic field are the signatures of a backscattering reduction occurring in the QPC [19], whose cause can be inferred comparing the cyclotron radius with the device size. In our case at $B = 1.1$ T the diameter of the electron classical orbit (cyclotron radius ~ 110 nm/B) is equal to the size of the 200 nm-wide square-shaped 2DEG protrusions that connect the constriction with the source and drain contacts: therefore for this magnetic field the geometrical backscattering taking place with the boundary of the etched protrusions begins to be significantly reduced. For larger fields, i.e. for cyclotron radius smaller than the size of the 2DEG protrusions, backscattering from the boundaries of the etched area is inhibited by skipping orbits.
In fig.3.9 the numerically derivative dG/dV_g of data of fig.3.8 (a) is reported in a colour map plot as a function of V_g and B up to 8 T. In the map blue regions correspond to lower values of dG/dV_g whereas orange regions are transconductance peaks. A plot of this type can be used to identify the transition edges between plateaus. The separation between peaks, ΔV_g, is linear in the external magnetic field (see dashed blue lines in fig.3.9). We will further discuss about this energy splitting in the following section comparing perpendicular with parallel magnetic field data.

Data showing the effect of the perpendicular magnetic field on the nonlinear conductance and on the ZBA in the same range of parameters V_g and V_{sd} for $B = 0$ and $B = 3$ T are reported in fig.3.10. Nonlinear conductance measurements acquired at $B = 0$ and 3 T for gate bias ranging from -0.04 to 0.9 V are reported in fig.3.10 (a) and (b). Traces of fig.3.10 (a) are some selected curves of fig.3.7 (b). In panels (c) and (d) the color maps of dG/dV_g curves, obtained numerically from G traces of panels (a) and (b), are plot-

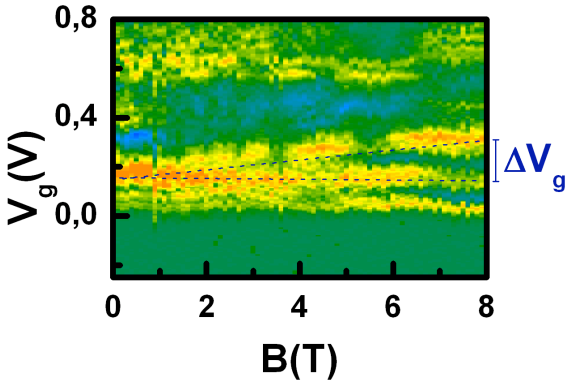

Figure 3.9: Calculated dG/dV_g of data of fig.3.8. Blue regions correspond to lower values whereas orange regions are higher values of dG/dV_g.

ted as a function of gate and source-drain bias. Blue regions correspond to lower dG/dV_g values while yellow regions correspond to higher ones. As can be seen from fig.3.10 (a) and (c) the curves acquired at $B = 0\ T$ are characterized by the presence of a fine structure in a narrow region around zero bias. Indeed for V_g larger than $\sim 0.2\ V$ a narrow peak at $V_{sd} \sim 0$ becomes prominent: its lineshape varies strongly upon changing V_g. This behaviour resembles that of the zero-bias anomaly (ZBA) reported in ref. [77]. This fine structure is seen to disappear at $B = 3\ T$, as shown in panel (b): the conductance at zero bias increases monotonically towards the G_0 plateau in correspondence of which several G traces merge. Concomitantly for large V_{sd} the conductance evolves towards nearly half G_0. The transconductance map clearly shows the characteristic diamond shape present when conduction in the QPC is trough non interacting 1D energy mode [39]. Following considerations of ref. [37] the energy separation between 1D subbands can be obtained from the intersections between the white lines marking in the $V_g - V_{sd}$ plane the transition edges between plateaus. We have estimated a value of about 1.3 meV for the distance between the first and the second level. The energy conversion factor η converting the gate voltage to the energy, $\Delta E = \eta \Delta V_g$, has been derived using Zeeman splitting energy discussed later on.

A conductance quantum equal to G_0 instead of $2 \cdot G_0$ requires a partial removal of degeneracy in the Si conduction band minima. The overall data taken in our device point to a conductance quantization in $G_0 = 2e^2/h$

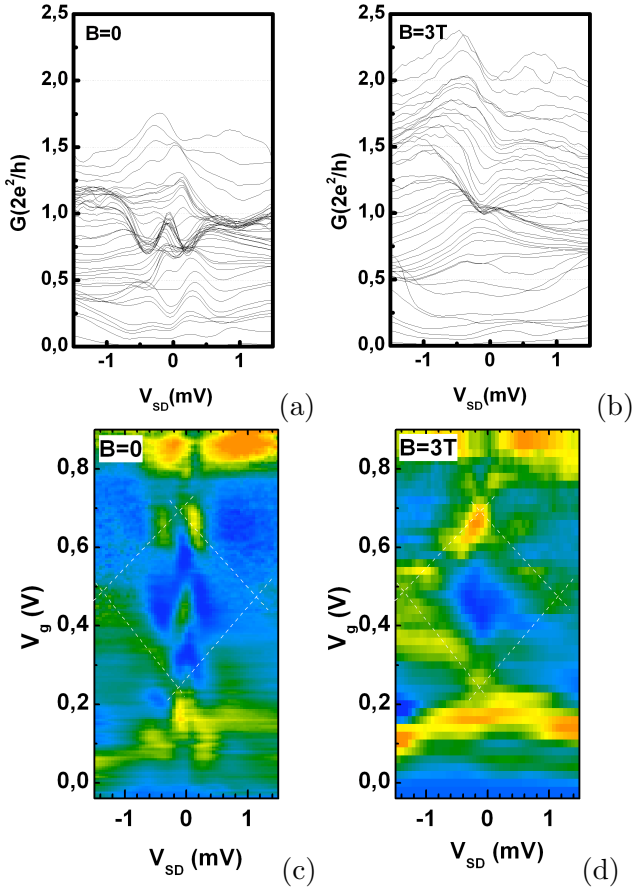

Figure 3.10: Non linear conductances vs dc source-drain bias for fixed gate voltage at (a) $B = 0$ and (b) $B = 3\ T$. Gate voltages were in the $(-0.04 \div 0.9)\ V$ range. (c) and (d) Maps of the transconductance obtained numerically from the curves of panels (a) and (b). In both transconductance maps the blue regions correspond to lower values whereas yellow regions are higher values of dG/dV_g. The description of the white lines is in the text.

units due to lifting of the twofold degeneracy of the z-valley in Si. From the diamond in the trasconductance map reported in fig.3.10 (d) we found an energy separation of the first two 1D modes equal to $\sim 1.3\ meV$, that we identify with the valley splitting at $B = 3\ T$. The reason is that this energy separation can be ascribed neither to Zeeman spin-splitting of valley-degenerated modes nor to the energy spacing of magnetoelectric subbands. We demonstrate our result as follows. A single non degenerate subband can be characterized by three quantum numbers: the transverse mode number n, the spin quantum number s and the valley quantum number v (where s and v can be ± 1) [78].

$$E_{n,s,v} = \left(n - \frac{1}{2}\right)\sqrt{(\hbar\omega_c)^2 + (\hbar\omega_0)^2} + \frac{1}{2}sg\mu_B B + \frac{1}{2}v\Delta_n(V_g, B) + eV_0 + \frac{\hbar^2 k^2}{2m^*}, \tag{3.3}$$

where Δ_n is the valley splitting. $\hbar\omega_0$ is the energy spacing between modes in absence of magnetic field, $\hbar\omega_c$ is the contribution from magnetic confinement equal to $\hbar eB/m^*$. eV_0 is the minimum of the confining potential, $g\mu_B B$ is the Zeeman energy and $\hbar^2 k^2/2m^*$ is the contribution of electron motion along the channel. In ref. [1] a phenomenological model has been proposed in which the valley splitting depends on both the external electrostatic and magnetic confinement,

$$\Delta_n(V_g, B) = \sqrt{\Delta_{ext}^2 + (\Delta_B B)^2}. \tag{3.4}$$

Indeed from eq.3.4 a zero-field valley splitting enhanced by electrostatic confinement of the electronic wave function is expected. In addition the external field B provides magnetic confinement of the wave function within the magnetic length, $l_m = \sqrt{\hbar/eB}$. However, in principle, the dependence of valley splitting energy on magnetic field is not relevant, therefore in the following we will not consider it. In fig.3.11 a schematic drawing of levels alignment is reported for $B = 0$, panel (a) and $B \neq 0$, panel (b). For $B = 0$, the energy separation between modes is $\hbar\omega_0$; if a valley splitting exists, each orbital level n splits in two valley-non degenerate states separated by Δ_n, see fig.3.11 (a), in the hypothesis that $\hbar\omega_0 > \Delta_n$. As for the case $B \neq 0$, the energy separation $\hbar\omega$ increases with magnetic field according to eq.3.3. In addition, each valley-split level in turn separates in two spin-split states, eq.3.3 (see fig.3.11 (b)). For a magnetic field of 3 T and for $g^* = 2$ a spin-

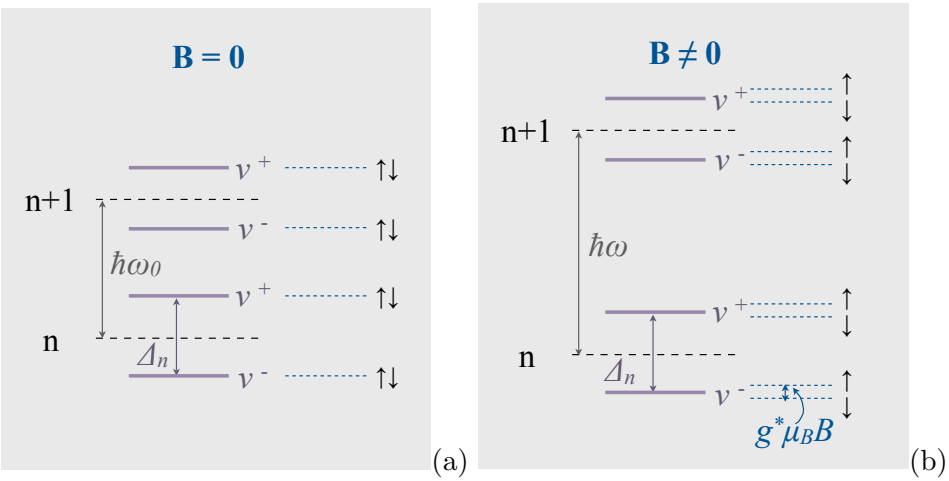

Figure 3.11: Schematics of the levels alignment: (a) For $B = 0$ the energy separation between modes is $\hbar\omega_0$, Δ_n is the energy valley splitting of the nth level. (b) For $B \neq 0$ the energy separation between modes is $\hbar\omega$, Δ_n is the energy valley splitting of the nth level and $g^*\mu_B B$ is the energy spin splitting of each valley-non degenearate state.

splitting of only 0.3 meV is expected. Therefore, Zeeman spin splitting can not take into account the energy separation of 1.3 meV observed in the data reported in fig.3.10 (a) and (b). Moreover at the same value of magnetic field, $B = 3\ T$, $\hbar\omega_c$ has been calculated to be 1.8 meV, leading to an energy separation between orbital modes $\hbar\omega > 1.8\ meV$ i.e. a value larger than the measured energy spacing in our QPC.

Parallel magnetic field

Conductance evolution in presence of a parallel magnetic field was also investigated. In fig.3.12 we report the linear G curves as a function of the gate voltage for parallel magnetic field in the $(0 \div 7.9)\ T$ range. The curves are acquired with a step of 0.1 T and vertically shifted for clarity. Peak-like and plateau-like structures are present in the G traces in the whole investigated range of magnetic field. The two main prominent structures in the conductance trace already described in fig.3.7 (a) show a complex evolution at low field; for B larger than 1.5 T the G traces are characterized by two clear plateau-like structures whose V_g positions shift linearly with the strenght of the magnetic field while the corresponding conductance evolves towards 0.5 G_0 and $1G_0$ values. Concerning the shoulder at 0.15 G_0, it evolves in a

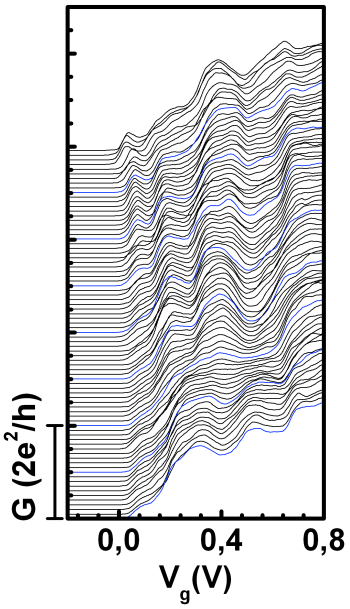

Figure 3.12: Linear conductance as a function of the gate voltage V_g acquired in a parallel magnetic field increasing from 0 (bottom curve) to 7.9 T (top curve). Traces are vertically shifted. Blue line curves correspond to magnetic field intensities of 0, 1, 2, 3, 4, 5, 6 and 7 T

more detectable peak whose conductance maximum raises toward 0.25 G_0 for magnetic field above 5 T. Linear conductance data in parallel magnetic field shown in fig.3.12 confirm our picture: even if conductance is affected by backscattering, at large field G traces are characterized by two prominent plateau-like structures at 0.5 G_0 and 1 G_0 values whose positions shift almost linearly with magnetic field as expected for Zeeman effect.
Analogously to fig.3.9 for perpendicular magnetic field, we reported dG/dV_g relative to conductance curve of fig.3.12 in a colour map plot as a function of V_g and B, fig.3.13. Dashed blue line in fig.3.13 are lined up for the same

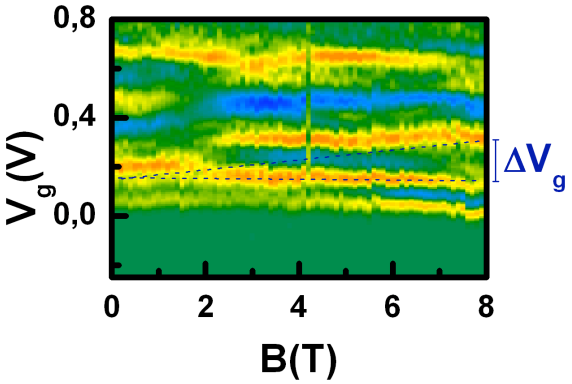

Figure 3.13: Calculated dG/dV_g of data of fig.3.12. Blue regions correspond to lower values whereas orange regions are higher values of dG/dV_g.

values of V_g and B as those of fig.3.9, reflecting the fact that the measured energy separation between transconductance peaks at $B = 8\ T$ is exactly the same for fig.3.9 and fig.3.13. It is worth noting that marked dashed blue line in fig.3.9 correspond to transitions from conductance $G = 0$ to $G = e^2/h$ and from $G = e^2/h$ to $G = 2e^2/h$, corresponding to the occupation of the first spin-resolved level and then of the second spin-resolved level. In conclusion, we attribute the measured splitting of transition edges ΔV_g of fig.3.13 to the Zeeman energy spin-splitting between non-degenerate levels. From the found Zeeman spin-splitting, we can determine the conversion factor η between gate voltage and energy using the relationship $\eta \Delta V_g = g^* \mu_B B$.

Concerning the valley splitting revealed by conductance measurements, we have measured a value equal to $\sim 1.3\ meV$ at 3 T. Valley splitting in *Si*-based mesoscopic structures is topic of great interest because it is related directly with spin coherence time and, consequently, with the possible use

of Si in spintronics [79, 80, 81, 82]. In the case of Si quantum wells with perfectly flat (100) interfaces a theoretical work elaborated in a framework of non interacting electrons predicts a valley splitting of the order of 1 meV [55]. In many experiments the measured valley splitting value was found to be smaller than the calculated ones [83, 84]. One possible explanation for the discrepancy between theoretical predictions and experimental findings is discussed in ref. [85] where it is proposed that atomic steps present at a quantum well interface suppress the valley splitting compared to ideally flat interfaces. Indeed while theoretically the valley splitting has an oscillatory behaviour as a function of the well width [55, 86], steps at real interfaces can suppress the splitting through an average on the well thickness. As reported by Goswami et al.[1] in Si based split gate QPC, electrostatic and magnetic confinement can contribute to reduce the number of monoatomic steps seen by the wavefunction obtaining an increase of valley splitting up to 1.5 meV. As for our investigated QPC, the physical removal of the region in which electrons are present provides a strong lateral confinement which plays a fundamental role in determining the observed valley splitting. Indeed it is an efficient method to enhance the valley splitting reducing its suppression operated by steps at heterostructure interfaces. Indeed the investigated QPCs were fabricated by using an hybrid approach in which confinement generated by physical etching of the 2DEG is combined with a Schottky gate for the elettrostatic control of the potential in the constriction [87]. Furthermore in this kind of devices, and in general in nanostructures defined by physically etching a 2DEG, we expect that the enhancement of valley splitting can be controlled by engineering the device geometry and size, independently of the electrostatic action of the gate electrode. With regard to magnetic field dependence of valley splitting, in fig.3.8 (b) we have found a filling up of the G_0 plateau corresponding to the first valley-split level with perpendicular magnetic field. However transition edges between valley-split plateau are not seen to shift with the application of the external field (see fig.3.8). As a consequence, we make a further assumption (compare with ref.[1]) claiming the occurrence of a zero-field valley splitting along with a field-independent valley splitting, Δ_n, in the investigated range of parameters (V_g and B).

In the following section we will report the conductance characterization of the nanowire device (QW), showing results very similar to those of the

QPC regardless of the different geometry of the confining potential.

3.3.2 Quantum transport of a *Si* Quantum Wire

In this section we present the main results obtained in the investigation of electronic transport in the quantum wire (QW) reported in fig.3.4 (a). The aim of this section is to show how similar behaviours manifest in devices with different geometries realized on different samples but using the same fabrication approach. In particular, we refer to valley-splitting occurrence in *Si*-etched based nanostructures. Therefore, we will describe linear and non linear conductance spectra emphasizing common aspects with the previous presentation of experimental data with and without the external magnetic field. Lastly, we will give an estimation of valley splitting in this QW using a different experimental approach for the calculation.

Linear conductance of this device has been already shown in fig.3.6 (c). In fig.3.14 we report a detail of the linear conductance below $2 \cdot G_0$ acquired at a temperature of 260 mK (black line curve) and 1.5 K (red line curve). The trace at lower temperature presents a series of characteristic peak-like

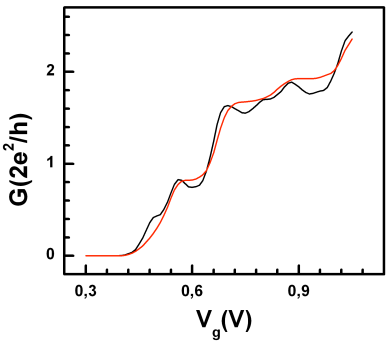

Figure 3.14: Detail of linear conductance curves as a function of the gate voltage. Measurement temperature were 260 mK (black line curve) and 1.5 K (red line curve).

structures resembling transmission resonances that occur at the 1D-2D transition regions of the confining potential [25]. These structures are energy averaged as soon as the temperature is increased or a voltage bias between source and drain is applied. Both curves present two prominent plateaus whose amplitude is evidently affected by transmission coefficients below the

unity. By correcting linear conductance curves of fig.3.14 for a constant transmission coefficient equal to 0.83, exact quantization of conductance in units of $G_0 = 2e^2/h$ is restored (fig.3.15). We apply this correction to all

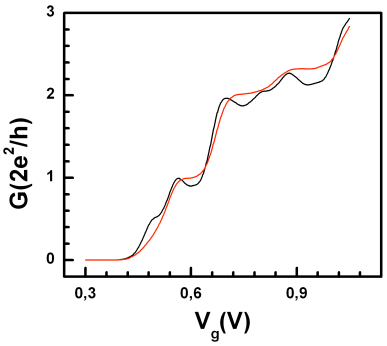

Figure 3.15: Linear conductance curve of fig.3.14 corrected for a constant transmission coefficient equal to 0.83 for both curves.

the data on the QW reported in the following.
In fig.3.16 non linear conductance traces $G(V_{sd})$ are reported as a function of V_{sd} for fixed values of V_g in the swept range of measure of fig.3.14, $(0.3 \div 1.05)\ V$, at a temperature of $0.26\ K$, panel (a), and $1.5\ K$, panel (b). Curves in panel (b) have been acquired for positive V_{sd} only. The presence

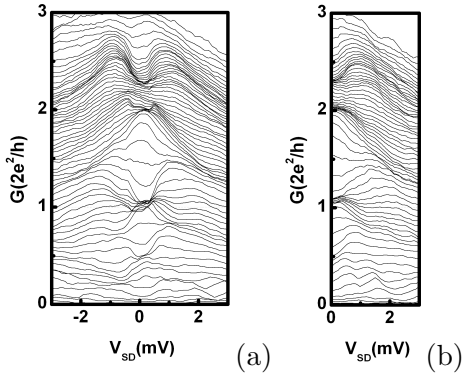

Figure 3.16: Non linear conductance traces $G(V_{sd})$ of the quantum wire (QW) as a function of V_{sd}, sweeping the gate voltage V_g from 0.3 to 1.05 V, at a temperature of $0.26\ K$, and $1.5\ K$, panel (b). Curves in panel (b) have been acquired for positive V_{sd} only.

of peaks in the linear conductance curve of fig.3.15 reflects in the $G(V_{sd})$ traces of fig.3.16 (a) as an overlapping of some curves near $G = 2e^2/h$ and

$G = 2 \cdot 2e^2/h$. As already noticed, with increasing temperature these structures are smeared out: at $T = 1.5\ K$ and $V_{sd} \sim 0$, $G(V_{sd})$ curves gradually merge toward values of $G = 2e^2/h$ and $G = 2 \cdot 2e^2/h$ (fig.3.16 (b)). For finite V_{sd} curves tend to converge toward half integer plateaus however an exact determination of the spacing between energy level is not possible.

Magnetic field conductance behaviour

Linear conductance of the quantum wire has been investigated in presence of a perpendicular magnetic field. The intensity of the field has been varied from 0 to 8 T with steps of 0.1 T. In fig.3.17 acquired curves are reported

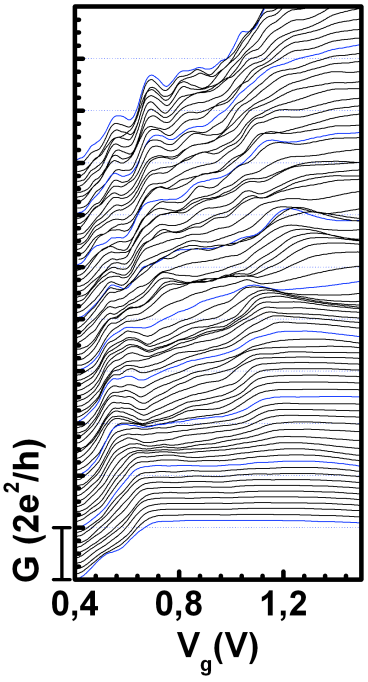

Figure 3.17: Linear conductance $G(V_g)$ acquired for increasing perpendicular magnetic field from 0 (top curve) to 8 T (bottom curve). Curves are vertically shifted. Blue line curve correspond to magnetic field of 0, 1, 2, 3, 4, 5, 6, 7 and 8 T. Vertical bar on the left represents unity of $2e^2/h$.

as a function of V_g and increasing the magnetic field from 0 (top curve) to 8 T (bottom curve). All traces have been vertically shifted so that blue line curves (corresponding to integer multiples of $B = 1\ T$) are vertically shifted of a quantity equal to $2e^2/h$. Four-terminal curves of fig.3.17 have been corrected performing the same procedure as that used for curves of

fig.3.8. The gate voltage in fig.3.17 covers a wide range of G, sweeping conductance at $B = 0$ from $G = 0$ to $G = 4 \cdot \frac{2e^2}{h}$ (shown up to $G = 3 \cdot \frac{2e^2}{h}$). The zero-field curve can be perfectly superimposed to that of fig.3.14. In this case, differently from fig.3.8 (b), a field as low as 2 T is not sufficient to restore a clear quantization. As a matter of fact, since the lateral width of the QW is about 40 nm, geometrical reduction of backscattering occur for B around 7 T (second blue line curve from bottom), being the cyclotron diameter $d_c \approx 45\ nm$ at $B = 7\ T$. Due to the presence of peaks and dips and hence to the lack of a clear quantization in the linear conductance curves up to about $B = 7\ T$, Zeeman spin splitting is distinctly resolvable only in the few bottom curves. In fig.3.18 we report the $B = 0$ and the $B = 8\ T$ linear conductance for comparison. In the orange line curve of fig.3.18 the

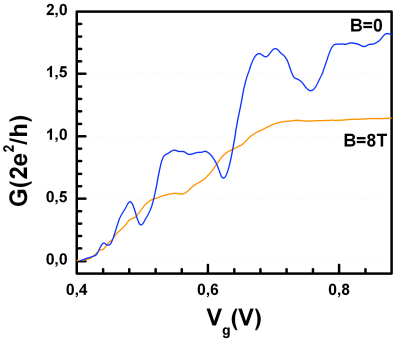

Figure 3.18: Linear conductance trace at zero-field (blue line curve) and 8 T (orange line curve).

formation of a fine plateau at $G = 0.5 \cdot G_0$ is incontrovertible and ascribed to the Zeeman splitting of spin degenerate 1D subbands. The found energy spacing $\eta \Delta V_g$ is in quantitative agreement with that found in fig.3.9 and fig.3.13. The amplitude reduction of plateaus with increasing magnetic field (appreciable both in fig.3.17 and in fig.3.18) is ascribed to the depopulation of magnetosubbands as B is varied [34] (discussed in the following). It is worth focusing on a detail of fig.3.18 which will be useful in the following discussion: note that the distance in energy (V_g) between the onsets of the $G \approx 0.5G_0$ and the $G \approx 1G_0$ plateaus in the $B = 8\ T$ (orange line) curve is approximately identical to that between the $G \approx 1G_0$ and the $G \approx 2G_0$ plateaus in the zero-field (blue line) curve.

A further key feature of the 1D nature of the system and a clear man-

ifestation of the existence of magneto electric subbands are the oscillations in the two terminal resistance of the narrow channel as a function of the magnetic field [88], reported in fig.3.19 (blue line curve). In the same figure, the Shubnikov-de Haas oscillations measured on a Hall bar of the same sample (already shown in fig.3.2) has been reported as a red line curve. Similarly to magnetic depopulation of Landau levels, in a finite-size system

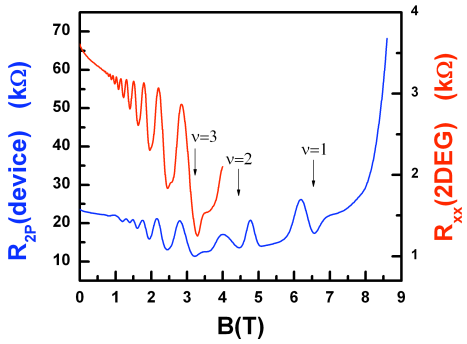

Figure 3.19: Two terminal magnetoresistance of the narrow channel (blue line curve) and of the 2DEG (red line curve) on the same sample.

the magnetic depopulation of subbands gives rise to oscillations in the magnetoresistance akin to the Shubnikov de Haas ones. Indeed, as the field is increased, a flattening of the subband dispersions occur until, eventually, the initial parabolic subband dispersions turn into practically dispersionless Landau levels, similarly to the 2D case. Differently from the 2D case, in which the number of occupied states n depends linearly on $1/B$, the effect of boundaries of the narrow channel makes n versus $1/B$ to be no longer linear. In figure 3.20 the minima of magnetoresistance oscillations corresponding to magnetic depopulation of subbands are reported as a function of the inverse magnetic field. In the high field region n exhibit a roughly linear dependence as a function of $1/B$. Departure from linear behaviour points to the lateral confinement effect on the quantized levels [88, 89]. Indeed the $n(B)$ presents a more complicated relation and it is no longer linear [88].

It should be noted that the linear dependence of n as a function of $1/B$ follows that of the 2D Shubnikov-de Haas oscillations minima (red squares in fig.3.19) suggesting a similar carrier density at high fields. However note the presence of double minima close to those depicted by arrows, indicating

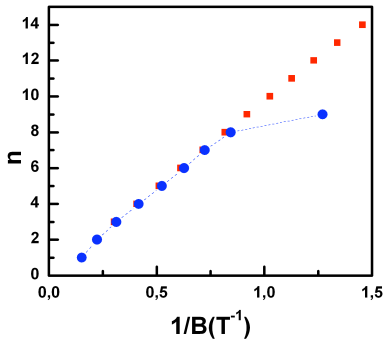

Figure 3.20: Sublevel index n versus inverse magnetic field B^{-1}. Blue circles refer to minima of the QW measured magnetoresistance reported as the blue line curve of fig.3.19. Red squares refer to the 2DEG Shubnikov de Haas oscillations minima of the red line curve of fig.3.19.

a splitting of energy levels ($\Delta\epsilon$) close to each subband. Considering that a minimum of the resistivity is obtained each time the Fermi level lines up to an energy level of the system,

$$E_F = \hbar\omega_c \left(n + \frac{1}{2}\right) \pm \frac{1}{2}\Delta\epsilon, \tag{3.5}$$

then the following relations can be written for the two split-energy levels, where $\Delta\epsilon$ is a general energy splitting between levels:

$$\begin{aligned} E_F &= \frac{\hbar e B_+}{m^*}\left(n + \frac{1}{2}\right) + \frac{1}{2}\Delta\epsilon \\ E_F &= \frac{\hbar e B_-}{m^*}\left(n + \frac{1}{2}\right) - \frac{1}{2}\Delta\epsilon. \end{aligned} \tag{3.6}$$

B_+ and B_- are the magnetic field positions of the minima of oscillations (indicated in fig.3.21 by symbols • , ▲ and ■ for $n = 3$, $n = 2$ and $n = 1$, respectively). From eq.3.6 the energy splitting between levels can be derived,

$$\Delta\epsilon = \frac{\hbar e}{m^*}\left(n + \frac{1}{2}\right)(B_- - B_+). \tag{3.7}$$

This quantity has been calculated for $n = 3$, $n = 2$ and $n = 1$ levels and results are reported in the table 3.2. In the same table a rough estimation of the Zeeman splitting energy is given for magnetic fields (indicated in the fourth column) close to the found splitting. From the numerical evaluation of

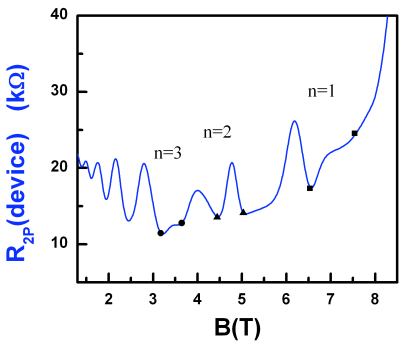

Figure 3.21: Two terminal magnetoresistance of the narrow channel, symbols indicate magnetic field positions relative to the alignment of the Fermi level with split levels. Symbols ● , ▲ and ■ refer to Landau level $n = 3$, $n = 2$ and $n = 1$, respectively.

	$\Delta\epsilon$	Δ_{Zeeman}	B^*
n	(from eq.3.7)	$= g^*\mu_B B^*$	(T)
3	0.97 meV	0.39 meV	3.4
2	0.89 meV	0.54 meV	4.7
1	0.88 meV	0.79 meV	6.9

Table 3.2: Calculated $\Delta\epsilon$ and Zeeman energy splitting Δ_{Zeeman} for the first three Landau levels.

the energy splitting $\Delta\epsilon$ and the Zeeman energy splitting Δ_{Zeeman} it becomes evident that the two quantity largely differ (at least for $n = 3$ and $n = 2$), therefore it is not possible to ascribe the found energy splitting to a spin-splitting of Landau levels due to the Zeeman effect. On the other hand, we believe that $\Delta\epsilon$ could account for the valley splitting of each level n inside the quantum wire [90]. The quantitative evaluation of the valley splitting energy, roughly $\Delta_n \approx 0.9\ meV$, agrees with results reported in literature [1]. Comparing results reported in the previous table, we have found that the valley splitting energy is approximately B-independent and that Δ_n and Δ_{Zeeman} become similar at $B \approx 7.6\ T$. As a matter of fact we have shown in fig.3.18 that the distance ΔV_g between the onsets of the two plateaus corresponding to the valley-split states of the first 1D level in the $B = 0$ curve is equal to the distance between the onsets of the two plateaus corresponding to the spin-split states. Considerations done for the QPC confinement potential of section 3.3 still hold for this device. As a matter of fact the strong lateral confinement reached by the physical removal of 2DEG portions produces a confinement of the electron wave-function that in principle could enhance valley-splitting energy, erasing the suppression of Δ_n operated by steps at heterostructures interfaces [1, 55]. The value of the valley splitting energy found for the QW investigated in this section, $\Delta_n \approx 0.9\ meV$, is in agreement with the result reported for the QPC1, $\Delta_n \approx 1.3\ meV$, within the confidence that we can attribute to the two distinct methods. Indeed, we have performed two different experiments in order to obtain a quantitative estimate of the valley splitting energy. Furthermore, it is noteworthy the fact that the investigated systems exhibit dissimilar geometries though the used approach is the same. Therefore the slight difference that we obtained is somehow resonable.

Low field measurements

A measure of the magnetoresistance at low magnetic fields can give an estimation of the phase coherence time τ_ϕ and the phase coherence length l_ϕ. We report the four-terminal resistance across the quantum wire for different values of the gate-voltage (from $V_g = 1.6\ V$, violet dotted curve to $V_g = 1.1\ V$, black dotted curve). In fig.3.22 it is evident a magnetic field reduction of the zero-field resistance of the quantum wire. The magnetic field positions of resistance minima seem not to depend significantly on the gate voltage. The

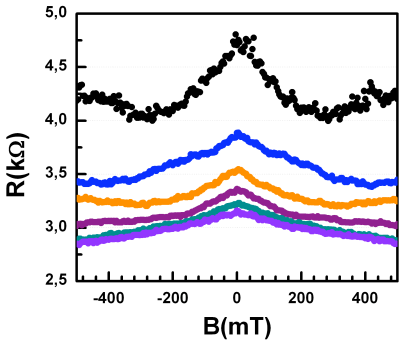

Figure 3.22: Low-field magnetoresistance of the QW of fig.3.4 (a) as a function of perpendicular magnetic field for gate voltage values equal to 1.6 V (violet dotted curve), 1.5, 1.4, 1.3, 1.2, 1.1 V (black dotted curve).

found behaviour can not be explained as the magnetic suppression of geometrical backscattering, as the critical field at which backscattering should be reduced is $B \approx 8\ T$ (from the condition $2l_c \approx W$). On the contrary, the found negative magnetoresistance is interpreted as the suppression of weak localization by a magnetic field in a 1D system [19]. Therefore we estimated τ_ϕ and l_ϕ by evaluating the critical field at which a minimum in the magneto resistance occurs. From the magnetoresistance curves of fig.3.22 we found $B_c \approx 0.29\ T$. In a 1D system in the pure metal limit ($W \ll l$ where W is the wire width and l is the mean free path) and weak field limit ($l_m^2 \gg Wl$, where l_m is the magnetic length), B_c is related to the phase coherence time by the relation $B_c = \frac{\hbar}{eW}\left(\frac{9.5}{W v_F \tau_\phi}\right)^{1/2}$ [19], so that we extracted $\tau_\phi = 5.1\ ps$ and, from $l_\phi = \sqrt{D\tau_\phi}$, $l_\phi = 304\ nm$.

3.4 Conclusions

In this chapter we have investigated $Si/SiGe$ nanostructures realized from modulation doped 2DEGs. The starting 2DEGs manifested similar characteristics in terms of mobility and carrier density. Results obtained from classical Hall effects have been reported. In addition high magnetic field characterization of 2DEG has been a useful tool: it has allowed us to extract the sheet carrier density n_s in a different range of magnetic field and the total scattering rate τ_q.

Devices of different geometries and sizes have been measured using low-frequency differential conductance measuremets.

In $Si/SiGe$-based 1D narrow conducting channels an independent electron picture for the carrier transport predicts a conductance quantization in integer multiples of $2 \cdot G_0 = 4e^2/h$ in presence of both spin and valley valley degeneracies. As a result, we have reported linear conductance quantization of the QW exhibiting plateaus in units of $4e^2/h$ at 4.1 K. On the other hand, by increasing experimental resolution upon lowering the temperature, our findings differ from these predictions.

All of the devices showed conductance curves affected by peak-like structures ascribed to both extrinsic and intrinsic causes, like presence of impurities, geometrical backscattering due to the confining potential or to the potential steps occurring at the entrance and the exit of the channel. These structures are seen to smear out or to disappear when increasing the temperature or the perpendicular magnetic field, depending on the origin of the structures. In any case none of the presented low-temperature curves exhibited conductance quantization in unit of $G_4 = 4e^2/h$. The application of a perpendicular magnetic field is seen to suppress geometrical backscattering occurring in the QPC1 and to restore a clear quantization in unit $2e^2/h$. From the analysis of the transconductance plot we estimated a valley splitting of 1.3 meV at a magnetic field of 3 T. Moreover non linear conductance measurements reveal the presence of a zero-bias feature.
For the narrow quantum wire, the channel width is too small and high magnetic field is necessary to suppress geometrical backscattering. In fact in this device suppression of geometrical backscattering occurs for fields as high as 7 T. This prevents a clear observation of the Zeeman spin splitting at lower fields. The investigation of the magnetoresistance oscillations in the quantum wire revealed an energy splitting of states in the channel. From quantitative considerations on the possible energy splittings we believe that the found splitting is the valley splitting between orbital levels.

In conclusion, we presented different etched Si-based devices: all devices manifested conductance behaviour compatible with the removal of the twofold valley degeneracy of conduction band present in a Si channel under tensile strain. We were able to give a quantitative estimation of the energy splittings of the order of ~ 1 mV using different measurements suitable for

each device. Results found for valley splitting are in quantitative agreement with those reported in literature.

Chapter 4

Transport Phenomena in $AlGaN/AlN/GaN$ heterostructures

*In this chapter we report experimental results of magnetotransport measurements of GaN-based nanostructures. The electrical characterization of the two-dimensional electron gas (2DEG) formed at AlN/GaN interface has been carried out by low- (*Classical Hall effect*) and high- (*Shubnikov-de Haas effect*) magnetic field measurements in different regimes of temperature (from 300 K to 0.25 K). In addition, quantum transport of low dimensional systems has been investigated at low temperature (0.25 K) and in presence of external magnetic field.*

4.1 2DEG characterization

The electrical characterization of the $AlGaN/AlN/GaN$ heterostructure has been carried out by using both low- and high-field magnetotransport in the $(300 \div 0.25)$ K temperature range; variable temperature Hall effect measurements were performed by using standard Hall bars between 300 and 16 K at a magnetic field of 0.7 T: dc-bias $I - V$ measurements were carried out in order to investigate carrier density, mobility and resistivity behaviours as a function of the temperature. Moreover, Shubnikov-de Haas (SdH) measurements were performed in order to test the quality of the 2DEG in these

samples. High-field characterization of the 2DEG has been carried out on mesa bars onto which nanostructured gates were patterned in order to study magnetotransport.

4.1.1 Classical Hall effect

Figure 4.1 shows the mobility μ and the carrier concentration n_{2D} as a function of temperature T. The found dependence of μ and n_{2D} is that expected for a two-dimensional electron gas [91]. Indeed, in 2DEGs realized in $AlGaN/GaN$ heterostructures, it is seen that these quantities are quite insensitive to temperature below about 80 K [16]. It should be noted the absence of a rapid increase of the carrier density at high temperature which indicates that no parallel parasitic conduction channel is present. From low field magnetotransport measurements, a carrier density of $1.1 \cdot 10^{13}$ cm^{-2} and a mobility of $2 \cdot 10^4 cm^2/Vs$ have been determined at 16 K. It is

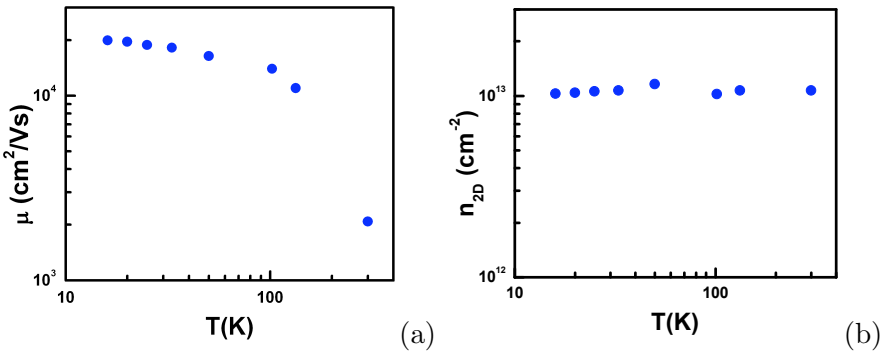

Figure 4.1: Mobility (a) and carrier density (b) as a function of temperature.

worth noting that this $AlGaN/AlN/GaN$ heterostructure exhibited record low temperature mobility compared to samples having the same value of the carrier concentration ($\sim 1.1 \cdot 10^{13}$ cm^{-2}) ever reported in literature [92, 93, 94, 95, 96, 97, 98, 99, 16, 100, 64, 101, 102, 103, 104, 17, 18, 106, 107, 108, 109, 110, 111, 112]. This gain in mobility is likely due to the insertion of an AlN layer which has twofold advantage: being AlN binary, it eliminates alloy scattering in the region where the 2DEG resides. Moreover, the higher conduction band offset of AlN respect to $AlGaN$ produces a lower penetration in the barrier and a larger confinement of electron wave function [102]. From zero-field mobility we have estimated a value of 2.5 ps

for the transport scattering time, $\tau_t = m^*\mu/e$, assuming $m^* = 0.22m_e$ for the effective mass of electrons [17].

In order to further investigate the properties of the 2DEG we exploited Shubnikov-de Haas effect (SdH) in the range of high magnetic field $(0 \div 12)$ T at a temperature of 0.25 K.

4.1.2 Shubnikov de Haas analysis

In figure 4.2 we report the magnetoresistivity measurement up to magnetic field intensities of 12 T, performed on a mesa bar upon which SET-geometry gates were deposited (see next section). Magnetoresistivity exhibits well de-

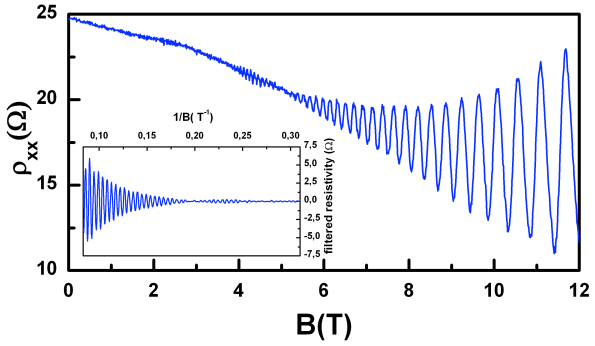

Figure 4.2: Measured magnetoresistivity as a function of magnetic field at a temperature of 0.25 K. *Inset:* filtered resistivity reported versus $1/B$.

fined oscillations as the field is swept from about 4 to 12 T. Since SdH oscillatory magnetoresistance is periodic with the inverse field $(1/B)$ we truncated the oscillations magnetoresistance (from 3 to 12 T) and removed both the low and high frequency components filtering the signal ρ_{xx} versus $1/B$ (band pass filter between 100 and 300 T), shown in the inset of fig.4.2. Then, an inverse-field interpolation of the curve has been carried out to have equally spaced points in $1/B$ and to perform a fast Fourier transformation (FFT). The FFT has been run by using a welch window and the result is reported in figure 4.3.

In figure 4.4 we report again the SdH magnetoresistivity measurement for magnetic field ranging from 1 to 12 T performed on a mesa bar of the same sample where gate electrodes forming a QPC were patterned. The

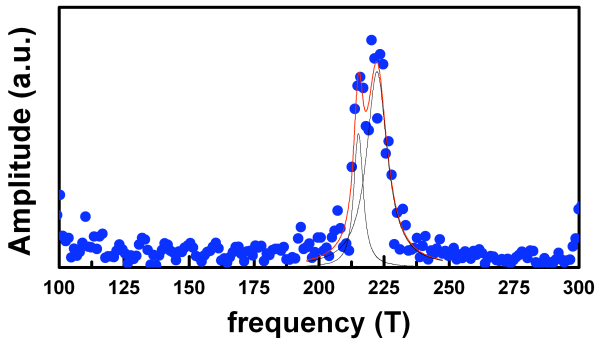

Figure 4.3: Calculated FFT of the curve reported in the inset of fig.4.2.

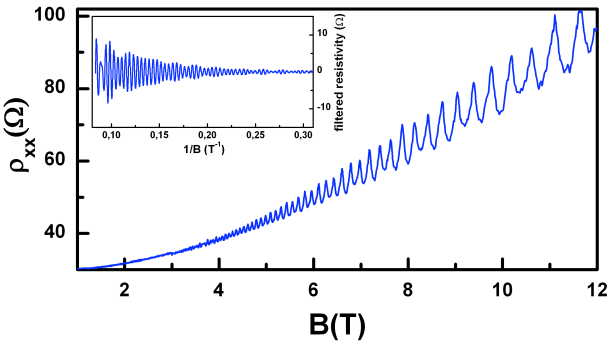

Figure 4.4: SdH oscillations: resistivity as a function of magnetic field ranging from 1 to 12 T. *Inset*: filtered resistivity against $1/B$.

quality of the magnetoresistivity measurement of fig.4.4 as a function of magnetic field is worse than that of fig.4.2: magnetoresistivity oscillations are not well defined and a monotonic increasing background is present. The FFT of the filtered resistivity (between frequencies corresponding to 200 and 300 T) produces a Lorentzian peak at a frequency of about 243 T, see fig.4.5.

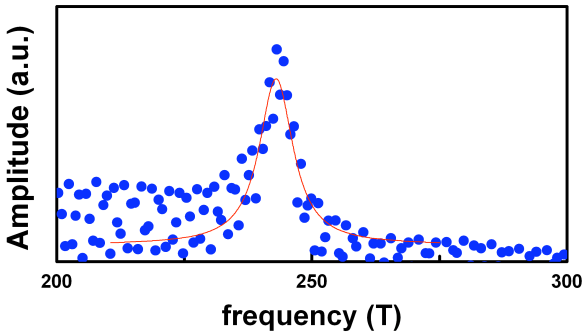

Figure 4.5: Calculated FFT of the curve reported in the inset of fig.4.4.

Measurements of the oscillation period of resistivity as a function of the inverse magnetic field $1/B$ are commonly used to determine the surface carrier density n_{2D}. It is known [113] that each discrete Landau level has a degeneracy $g = eB/\pi\hbar$ per unit area, including spin degeneracy. With increasing magnetic field intensity, the electrons are redistributed among a decreasing number of levels. The number of occupied levels at zero temperature is $n = n_{2D}/g$, where n_{2D} is the two-dimensional carrier concentration: n changes by one whenever the inverse of the field changes by $\Delta(1/B) = e/n_{2D}\pi\hbar$. When electrons of the 2DEG occupy the a single subband, $n_{2D} = k_F^2/2\pi$ and the above period gives the semiclassical expression for the period of the magneto-oscillations. Thus, by simply calculating the Fast Fourier Transform of the signal, it is possible to estimate the oscillation frequency $f = \frac{hn_{2D}}{2e}$, and hence n_{2D}.
Alternatively, one can state that minima of resistivity occur at those values of $1/B_n$ for which E_F is aligned to the n^{th} Landau level, $E_F = (n + \frac{1}{2})\hbar\omega_c$, where $\omega_c = eB/m^*$. Therefore, a second way to estimate the carrier density is to determine the slope from the linear dependence of n as a function of

the inverse magnetic field,

$$n = \frac{\pi\hbar n_{2D}}{e}\frac{1}{B_n} - \frac{1}{2}. \tag{4.1}$$

By exploiting the properties of the oscillation period of the magnetoresistivity, we determined the frequency from the FFT (fig.4.3 and fig.4.5). Figure 4.3 indicates that well-defined frequency components are predominant in the resistivity reported in fig.4.2. In detail, from the measurement reported in fig.4.2 it can be noted that the resistivity has oscillations periodic in $1/B$ and a beat around $B \simeq 5\ T$ ($1/B \simeq 0.20\ T$) that produces the double peak in the amplitude of FFT (fig.4.3). The frequencies of the two peaks are about 215.2 T and 222.3 T, corresponding to carrier density of $1.040 \cdot 10^{13}$ cm^{-2} and $1.075 \cdot 10^{13}$ cm^{-2}, respectively, assuming spin degenerate levels. Alternatively, assuming spin-non degenerate levels, we get $0.520 \cdot 10^{13}$ cm^{-2} and $0.537 \cdot 10^{13}$ cm^{-2}. The two possibilities will be discussed in the following section.

Concerning the data of fig.4.4, the quality of the measurement does not allow an analysis as accurate as that of fig.4.2: the oscillatory magnetoresistivity does not manifest any beating pattern therefore a unique frequency merges from the FFT, corresponding to a carrier density of $1.1 \cdot 10^{13}$ cm^{-2}, in agreement with classical Hall measurement reported in section 4.1.1. However the monotonic increasing background in the magnetoresistivity may indicate the presence of a low mobility parallel channel whose origin is still unknown.

Beating pattern analysis

In the Shubnikov de Haas oscillations reported in fig.4.2 we have observed a beating pattern resulting in a double-peak structure in the $1/B$ Fast Fourier Transformation of fig.4.3. Only a single node is resolved in the beat. In principle, there can be different origins for this beating pattern. The presence of inhomogeneities in the carrier density [114], the occurrence of magneto-intersubbands-scattering (MIS) supported by the occupancy of a second 2D level [99, 115, 116] or a zero-field spin splitting resulting from spin-orbit coupling [106, 117, 108] are possible causes producing a beat in the magneoresistivity of fig.4.2. We will consider the three hypothesis giving reasons of plausibility for each though, for a definite answer concerning the origin

of the observed behaviour, further measurements are required.

Although our sample is highly uniform, a spatially inhomogeneous carrier distribution can be present due to a pinning of the Fermi level in some regions, such as those where the metallic gate electrodes cover some areas above the heterostructure. This would result in slightly different electron concentrations in the 2DEG, producing a beating pattern in the Shubnikov de Haas oscillations and contributing to the FFT with the measured sheet carrier densities of $1.040 \cdot 10^{13}\ cm^{-2}$ and $1.075 \cdot 10^{13}\ cm^{-2}$.

The second considered hypothesis is that magneto intersubband scattering might produce a similar beating pattern in the oscillatory magnetoresistance [107, 115, 118, 116]. In recent years it has been discovered that the oscillatory magnetoresistance of a high mobility 2DEG with two populated subbands contains at least three components [119]: the SdH oscillations of the two subbands and an oscillation due to elastic scattering between the subbands. This third component was termed the magnetointersubband scattering. According to Coleridge [62], in the limit of low fields and low temperature, the MIS correction to the resistivity takes the form

$$\Delta\rho^{MIS} \propto exp\left[-\frac{\pi}{\omega_c}\left(\frac{1}{\tau_1}+\frac{1}{\tau_2}\right)\right] cos\left[\frac{2\pi(E_2-E_1)}{\hbar\omega_c}\right], \tag{4.2}$$

where E_1 (E_2) and τ_1 (τ_2) are the energy and quantum scattering time, respectively, of the first (second) occupied 2D subbands. Conversely, the oscillatory part of resistivity due to the SdH oscillations has a temperature damping factor $\chi(T) = \frac{(2\pi^2 k_B T/\hbar\omega_c)}{sinh(2\pi^2 k_B T/\hbar\omega_c)}$,

$$\Delta\rho_j^{SdH} \propto \chi(T) exp\left(-\frac{\pi}{\omega_c\tau_j}\right) cos\left[\frac{2\pi(E_F-E_j)}{\hbar\omega_c}+\pi\right]. \tag{4.3}$$

This MIS effect is due to increased elastic-intersubband scattering at subband Landau-level crossover. The MIS correction to the resistivity varies periodically in $1/B$, leading to an oscillation similar to the Shubnikov-de Haas oscillation [118]. The second of the two above equations (eq.4.3) is the typical SdH term: in presence of two subbands, $j = 1, 2$, it predicts two SdH frequencies [99], $f_j = \Delta E_j m^*/\hbar e = h n_j/2e$, (since $\Delta E_j = \pi\hbar^2 n_j/m^*$) relative to the two occupied subbands. The first equation (from eq.4.2) is the MIS term. It does not contain the thermal damping factor $\chi(T)$ and its oscillation frequency is proportional to the subband spacing, E_{12},

$f_{MIS} = (E_1 - E_2)m^*/\hbar e = f_1 - f_2$. Assuming, in our case, that the two frequencies of the double peak in the FFT of fig.4.3 correspond to $f_1 = 222.3$ T and $f_{MIS} = 215.2$ T, the following values for the carrier densities of the two subbands are obtained, provided that $f_2 = f_1 - f_{MIS}$: $n_1 = 1.07 \cdot 10^{13}$ cm^{-2} and $n_2 = 3.4 \cdot 10^{11}$ cm^{-2}. These two values would give a total carrier density of $1.1 \cdot 10^{13}$ cm^{-2} which is in agreement with the result found at low magnetic field (Hall effect). The energy separation between the two levels would be $\Delta E_{12} = E_2 - E_1 = f_{MIS} e\hbar/m^* = 112.7$ meV, assuming $m^* = 0.22 m_e$ and that the Fermi energy is 116.4 meV above the first conduction band minimum ($\Delta E_1 = E_F - E_1$). The hypothesis of MIS has to be supported by the occupation of a second subband in the sample. As a matter of fact the occupation of higher subbands has been predicted in [120] and observed in a number of works with high electron concentration, [95], [96], [104]. Zheng et al. have reported that the occupation of the first two subbands in a two-dimensional electron gas with a triangular quantum well took place when the 2DEG sheet carrier concentration reached $7.2 \cdot 10^{12}$ cm^{-2} [121]. If the observed beating pattern is caused by the MIS effect in our sample, the peak position of the second subband SdH oscillations in the FFT spectra should be $f_2 = f_1 - f_{MIS} = 7.1$ T. The peak of the oscillations is probably screened by the influence of low frequency components in the resistivity. Since the MIS correction to the resistivity (eq.4.2) does not contain temperature-damping factor as the oscillatory SdH resistivity, the MIS term may become dominant with increasing temperature [115]. Therefore in order to unequivocally identify the MIS component further investigations at different temperatures are required.

The third hypothesis is that of a spin-orbit coupling in the 2DEG, largely investigated in this kind of $Al_xGa_{1-x}N/GaN$ heterostructures, which manifests predominantly with a beating pattern in the magnetoresistivity [117, 108, 122, 106, 107, 123]. This spin-orbit interaction (SOI) gives rise to a zero-field spin splitting Δ_{so} at the Fermi energy. In $Al_xGa_{1-x}N/GaN$ 2DEGs realized on wurtzite structure crystals zero-field spin splitting can originate from two mechanisms. Firstly, it can be due to a macroscopic electric field in an asymmetric quantum well containing the 2DEG (*interface Rasbha effect*). Secondly, the lack of inversion symmetry of the wurtzite type lattice can result in a zero-field spin splitting as well (*bulk Rasbha effect*). In contrast to zinc-blend-type lattices, here the effective electric field is oriented

along the (0001) direction and thus parallel to the macroscopic electric field in the quantum well [114]. Concerning the first mechanism, the sources of asymmetry of the quantum well include asymmetric doping profile, differing chemical or alloy compositions of the confining materials on either side of the well, electric fields applied via front or back gates, and the barrier height difference associated with the inequivalence of the two interfaces of quantum well [124]. In our heterostructure there is no intentional doping thus both piezoelectric effect and spontaneous electric polarization generate free carrier in the quantum well. These induce a large electric field at the AlN/GaN heterojunction and a strongly asymmetric well. The structure inversion asymmetry of the wurtzite type lattice gives rise to a spin-orbit splitting in the conduction band states linear in k which appears in the Hamiltonian as an additional 'Rashba term' [125, 126],

$$H' = \alpha_{so}\vec{\sigma} \cdot [\hat{z} \times \vec{k}], \tag{4.4}$$

where $\vec{\sigma}$ are the Pauli matrices. α_{so} is the spin-orbit coupling stregth related to the spin-orbit energy $\Delta_{so} = 2\alpha_{so}k_F$ which is the splitting energy at the Fermi surface. This term can be interpreted as the interaction of the electron spin with an effective magnetic field, $\vec{B}_{so} = (2\alpha_{so}/g\mu_B) \cdot [\hat{z} \times \vec{k}]$, which is referred to as the Rashba field. Thus the Rashba term $H' = g\mu_B\vec{\sigma} \cdot \vec{B}_{so}$, analogously to the Zeeman term, has the effect of removing the twofold spin degeneracy of the subband at the Fermi energy along the direction of the effective field [124]. This will produce an energy splitting for the two different spin populations $n_\downarrow$ and $n_\uparrow$ at the Fermi energy $E_F = \hbar^2\pi n_{2D}/m^*$, closely linking the spin direction to the electron wave-vector, $\vec{B}_{so} \sim [\hat{z} \times \vec{k}]$. Therefore, if we assume that the found carrier concentrations correspond to the different spin populations, then $n_\downarrow = 0.520 \cdot 10^{13}\ cm^{-2}$ and $n_\uparrow = 0.537 \cdot 10^{13}\ cm^{-2}$. The obtained spin-resolved concentrations allow us to determine the spin orbit coupling parameter [117],

$$\alpha_{so} = \frac{\Delta n\hbar^2}{m^*}\sqrt{\frac{\pi}{2(n_{2D} - \Delta n)}}. \tag{4.5}$$

Here, Δn is the difference between spin up and spin down electron concentration. We obtained $\alpha_{so} = 2.28 \cdot 10^{-12}\ eV \cdot m$ which is the same order of magnitude as those found in other Rashba-like GaN-based heterostruc-

tures [106, 108, 127, 128, 129]. In addition we have estimated the spin-splitting energy Δ_{so} at zero magnetic field to be 3.71 meV. In our analysis we have ignored the Zeeman splitting $g^*\mu_B B$ because its contribution at low fields is negligible compared to Δ_{so} (at $B = 2\ T$ Zeeman energy is about an order of magnitude smaller than the spin-orbit energy produced by Rashba term). The found value for Δ_{so} is in excellent agreement with the total zero-field spin-splitting energy calculated by the frequency difference $E_\uparrow - E_\downarrow = \frac{2\pi\hbar^2(n_\uparrow - n_\downarrow)}{m^*} = 3.69\ meV$. Calculated parameters are listed in table 4.1.

$n_\downarrow\ (cm^{-2})$	$0.520 \cdot 10^{13}$
$n_\uparrow\ (cm^{-2})$	$0.537 \cdot 10^{13}$
$\alpha_{so}\ (eV \cdot m)$	$2.28 \cdot 10^{-12}$
$2\alpha_{so}k_F\ (meV)$	3.71
$E_\uparrow - E_\downarrow\ (meV)$	3.69

Table 4.1: Calculated parameters relative to measurement reported in fig.4.2.

In figure 4.6 we report a comparison between our data of the spin-orbit coupling parameter α_{so} (depicted as a blue star) and results found in literature on similar systems. The figure has been created starting from data collected

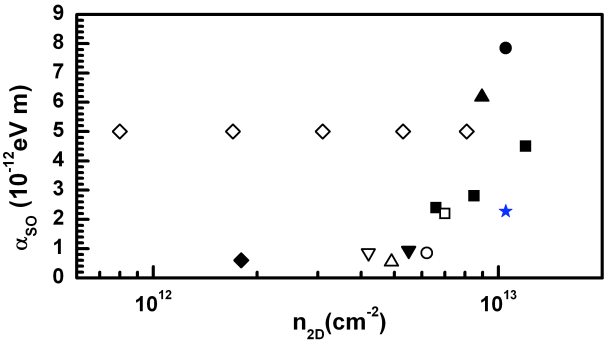

Figure 4.6: Collection of data reported from different authors on the spin-orbit coupling parameter. ○ ref.[130], △ ref.[131], ▲ ref.[106], ■ ref.[129], ▼ ref.[127], ♦ ref.[108], □ ref.[109], ▽ ref.[114], ◊ ref.[132], ● [128]; blue star is our data.

in reference [128]. From fig.4.6 it is evident that our result is in qualitative

agreement with literature.

Up to now we have discussed three possible origins for the observed beating pattern. We showed that the found behaviour can be attributed to inhomogeneities of the carrier density of the 2DEG, to magneto intersubband scattering occurring if two subband of the electron gas are occupied or, lastly, to spin-orbit coupling due to structural inversion asymmetry of the quantum well. Spin-orbit coupling in a 2DEG can be also studied by analyzing quantum correction to the conductivity, i.e. weak antilocalization (WAL). In the following paragraph we will show results obtained from WAL experiments.

Weak Anti Localization

A valid tool for the investigation of the SOI in GaN-based heterostructure is low-field magnetotransport. Indeed the signature of SOI is an increase of magnetoresistance with increasing of magnetic field in the range of $\sim mT$, called positive magnetoresistance, due to *weak antilocalization* [133]: in presence of SOI, spin-relaxation due to spin-orbit coupling and impurity scattering produces a positive contribution to the conductivity (antilocalization). Magnetic field suppresses this antilocalization [117, 134]. The effect of localization in weakly disordered semiconductors systems has been described in chapter 1 and can be viewed as the quantum interference between two waves propagating by multiple scattering along the same path but in opposite directions. When a magnetic field is applied, the phase picked up along the two paths have opposite sign, and as a consequence, a negative magnetoresistance is observed (see chapter 1). This effect is commonly known as weak localization. In system with strong spin-orbit interaction, the magnetoresistance reverses its sign, which is in contrast to the above, known as weak anti-localization [134]. In figure 4.7 (a) and (b) we report the low-field magnetoconductvity and magnetoresistivity measured on the same Hall bar of measure of fig.4.4. Here a peak at $B = 0$ is found in the magnetoconductivity (panel (a)) that can be attributed to WAL, whereas the increase for $|B| > 3.5\ mT$ can be assigned to WL being the dominant contribution at larger magnetic field. Indeed a crossover from negative magneto conductivity to positive magneto conductivity is expected for $B \approx B_{so}$ [109, 114]. It is worth noting that the percentage variation of the resistivity $\rho(B)/\rho(0)$

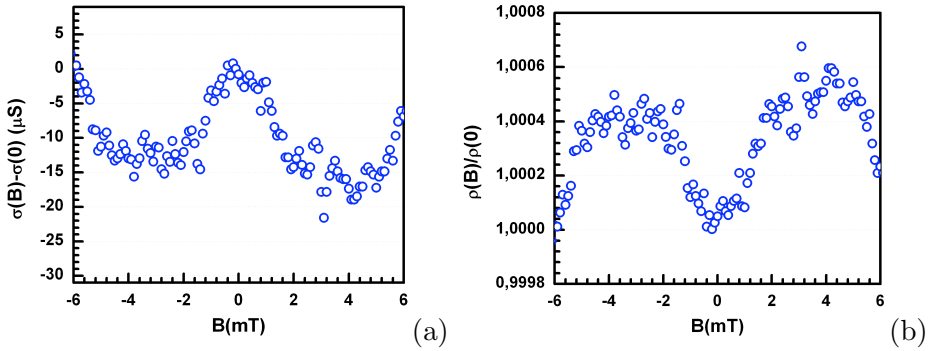

Figure 4.7: Weak antilocalization peak of low field magnetoconductivity (a) and positive magnetoresistivity (b).

is very small, though the difference of conductivity respect to the zero-field value, $\sigma(B) - \sigma(0)$, is of the same order of magnitude as those reported in literature (see fig.4.8) [109, 134].

From the magnetic field scale B_{so} the spin-orbit coupling value can be

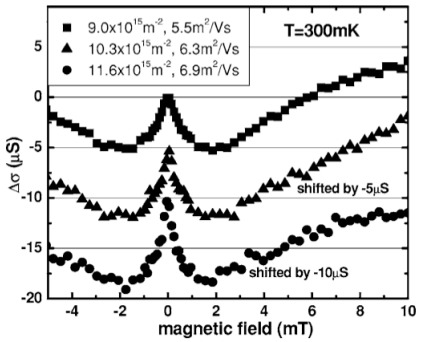

Figure 4.8: Weak antilocalization peak of low field magnetoconductivity from [109].

extracted since $B_{so} = (m^* \alpha_{so})^2 / e\hbar^3$ [109]. In this case we have calculated $\alpha_{so} = 0.8 \cdot 10^{-12}\ eV \cdot m$, taking to a spin-orbit splitting energy of $\Delta_{so} = 1.33\ meV$. This result shows that α_{so} extracted from the beating pattern (measure of fig.4.2) is not consistent with α_{so} determined from the WAL analysis (fig.4.4). However a general disagreement is found in literature between SdH and WAL analysis in evaluating the zero-field spin splitting [128]. In particular, our discrepancy between results obtained from the two different measurement approaches reproduces quite well the disagreement that

merges reviewing literature results. In ref.[128] data of Δ_{so} from several experimental works have been collected and compared in the plot reported in fig.4.9. Figure 4.9 shows $\Delta_{so} = 2\alpha k$ as a function of the carrier density extracted from the two different analysis; filled symbols correspond to values calculated from SdH measurements whereas empty symbols are from WAL measurements. In the plot of fig.4.9 we have added our results from SdH

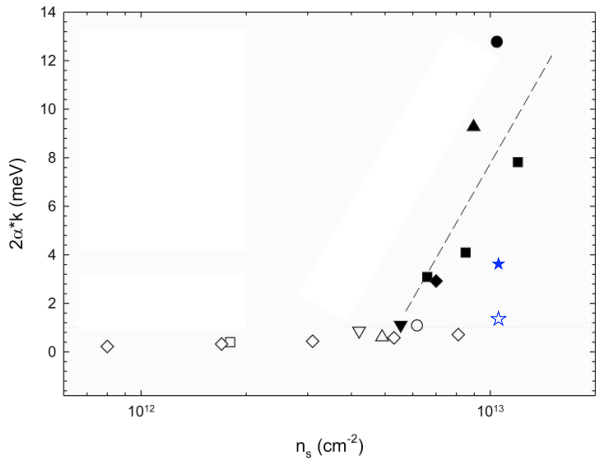

Figure 4.9: $\Delta_{so} = 2\alpha k$ term as a function of electron density. The graph has been modified from that taken from [128]. Filled and empty symbols correspond to results obtained from SdH and WAL analysis, respectively. Data reported in the plot refer to ● [128], ○ [130], △ [131], ▲ [106], ■ [129], ▼ [127], ♦ [108], □ [109], ▽ [114], ◊ [132]. The filled and empty blues stars are our results calculated from SdH and WAL measurements, respectively.

and WAL analysis as a filled and an empty blue stars, respectively.

In conclusion, our findings do not allow us to give a definite and unequivocal interpretation of gathered data. Indeed in a 2DEG the occurrence of WAL is an unambiguous sign of the presence of spin-orbit coupling. In contrast, a beating pattern in the Shubnikov de Haas oscillations can have other origins, e.g. an inhomogeneous carrier distribution, or magneto intersubband scattering [114]. On the other hand, in ref.[128] it is argued that SdH analysis seems to be more valid for sample with a carrier density above $6 \times 10^{12}\ cm^{-2}$. Therefore, in our 2DEG, since the electron concentration is of the order of $\sim 10^{13}\ cm^{-2}$, results obtained from SdH analysis are more confident compared to WAL analysis.

Dingle Plot

A linear Dingle plot is reported in fig.4.10, showing in logarithmic scale the oscillation amplitude of the Shubnikov de Haas resistivity of fig.4.2 $\Delta\rho/4\chi(T)\rho_0$ against the inverse magnetic field $1/B$. From the slope of the

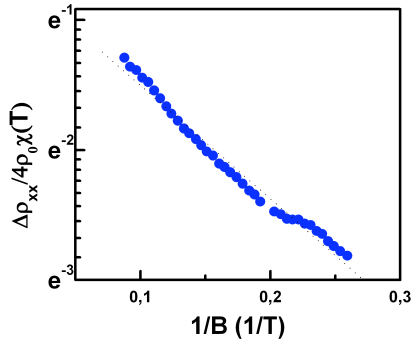

Figure 4.10: The Dingle plot gives a value of 0.4 ps for the quantum scattering time, τ_s.

linear fit we derived $\tau_q \approx 0.4\ ps$ which is in agreement with values found in literature [135, 136, 97]. However, it should be noticed that in our Dingle plot the shoulder at $B^{-1} \approx 0.2T^{-1}$, pointing to the presence of a beating, does not allow an exact determination of this value. In [63] it is argued that poor Dingle plots can be attributed to inhomogeneities in the sample, i.e. two or three regions with different densities giving rise to beats. However in the paper it is not considered the possible occurrence of a zero-field spin splitting which also gives beats (see previous paragraph). In fig.4.10 the intercept $1/B = 0$ of the Dingle plot is lower than zero. This can indicate the presence of a parallel path: nevertheless absence of strong parallel conduction is further supported by comparing the densities obtained from the classical Hall measurement ($1.1 \cdot 10^{-13}\ cm^{-2}$ at 16 K) with those from the SdH effect ($1.06 \cdot 10^{-13}\ cm^{-2}$ at 0.25 K). The slight difference between the two densities has to be addressed to the different measure temperature. Thus, we conclude that the smaller value of the intercept has to be attributed to other reasons than parallel conduction channel but the origin has not been understood yet.
In order to derive the ratio τ_t/τ_q in our 2DEG, the transport scattering time τ_t has been calculated to be 2.5 ps assuming $\mu = 20200\ cm^2/Vs$ for the zero-field mobility at $0.25K$ and $m^* = 0.22 \cdot m_e$ for the effective mass. The value

of 6.3 estimated for the ratio τ_t/τ_q indicates that large angle scattering is still the dominant mechanism of scattering [103]. Nonetheless it should be mentioned that this AlN/GaN structure exhibited record low temperature mobility for samples with comparable density. This improvement is thought to be due to the AlN interlayer. Indeed we outline that the presence of the binary AlN has the effect of eliminating alloy scattering in the region where 2DEG resides and it reduces the penetration of the electron wave function into the barrier thus reducing the interfacial roughness (IR) scattering contributions. In addition to the increased mobility value obtained with the improved AlN/GaN junction, also the value of 0.4 ps for τ_q is long compared to typical $Al_xGa_{1-x}N/GaN$ heterostructures. This points to an overall reduction of both small and large angle scattering in this structure although the ratio τ_t/τ_q is not high. Due to the relative small ratio τ_t/τ_q found, we conclude that the main scattering mechanism is dominated by short range interfacial roughness scattering [64, 98].

The quantum scattering time is a measure of the collision broadening of the Landau levels and is related to the half-width of the broadened Landau level through $\Gamma = \hbar/2\tau_q$ which in our case has been estimated to be 0.82 meV. Thus a relatively strong disorder leading to the Landau level broadening, $\hbar/2\tau_q \gg g^*\mu_B B$, can suppress the net electron spin polarization and therefore prevent the observation of spin split SdH oscillations. This effect is supposed to affect the oscillations of resistivity reported in fig.4.2 and fig.4.4.

The introduced results shows the importance of SdH measurements as they provide much more informations than what is typically obtained through classical Hall effect studies alone.

4.2 Mesoscopic transport in low-dimensional systems

In this section we present transport measurements on different geometry devices. These have two typologies of split gate configurations: two of them are constrictions with approximately adiabatic transverse confinement potential of various widths (140 nm device A in fig.4.11 (a) and 250 nm device B in fig.4.11 (b)); the last one is a constriction which results by negatively biasing two opposite gates (G1 and G3 whose distance is 225 nm) constituting one of the two barriers of a *Single Electron Transistor* (device C in fig.4.11 (c)). Mesoscopic devices investigated in this section were fabricated on the same sample whose 2DEG transport properties were discussed in section 4.1. We remind that this 2DEG has a low temperature (0.25 K) mobility of 20000 cm^2/Vs and a carrier density of about $1.05 \cdot 10^{13}$ cm^{-2}.

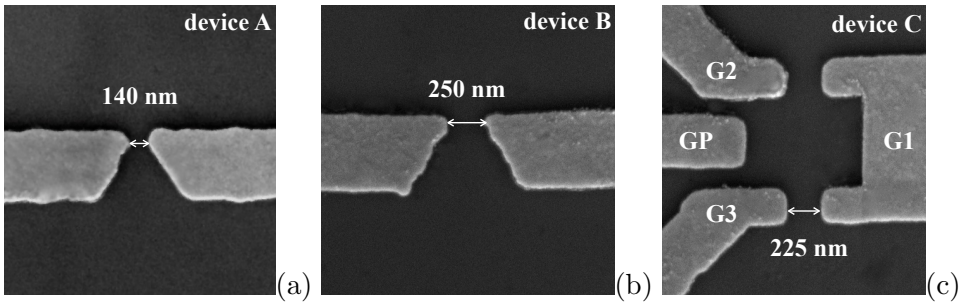

(a) (b) (c)

Figure 4.11: (a) and (b) SEM picture of two QPCs whose channel width is 140 nm (device A) and 250 nm (device B), respectively. (c) SEM picture of a SET geometry device. The investigated QPC is that formed by the split-gates denoted with G1 and G3 in panel (c) whose separation is 220 nm (device C).

In figure 4.12 linear conductance curves acquired on devices of fig.4.11 are presented. Figure 4.12 (a) shows a single linear conductance trace of QPC reported in fig.4.11 (a). In order to determine unambiguously the conductance values of each step, the derivative, $(dG/dV_g)^{-1}$, has been numerically evaluated and reported in the right hand side of the figure. In fig.4.12 (b) and (c) the conductance curves reproducibility in the same and in different thermal cycling has been investigated for device B and C of fig.4.11 (b) and (c), respectively. Groups of curves of different colours refer to different cooldown from room temperature to base temperature.

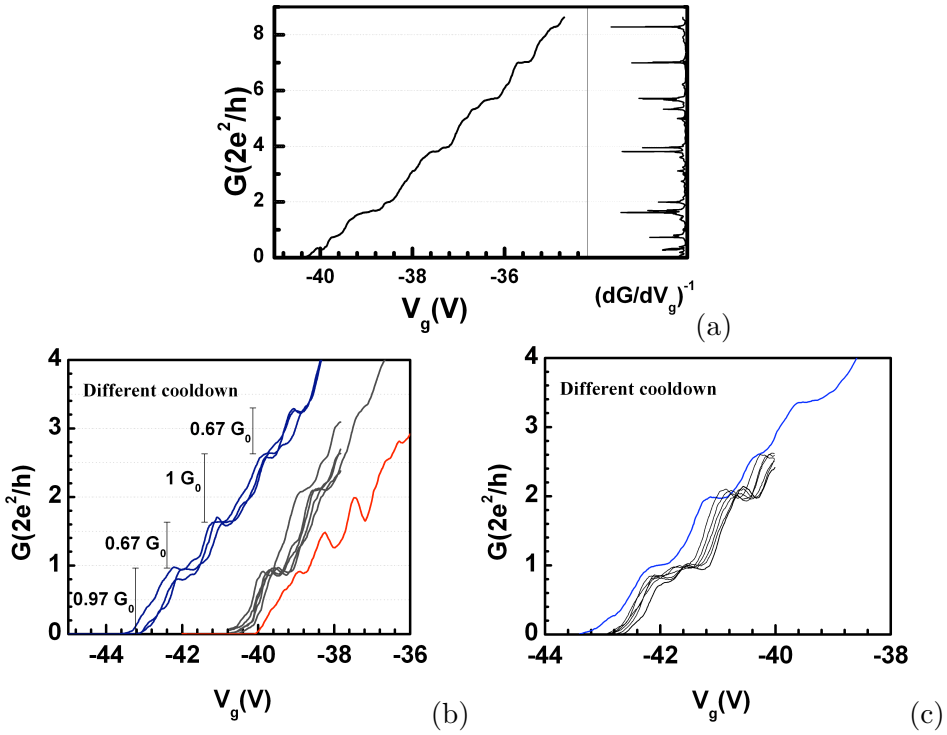

Figure 4.12: (a) Linear conductance of device A taken at 0.38 K. In the right hand side the derivative $(dG/dV_g)^{-1}$ of conductance is reported. (b) Linear conductance curves of device B: different colours line curves refer to different cooldown from 300 K to base temperature (0.38 K for blue line curves, 0.25 K for grey line curves and red one). (c) Linear conductance curves of device C: different thermal cycle from 300 K to 0.38 K, blue line curve, and to 0.25 K, black line curves.

Though the fine structure of conductance traces evolves differently depending on the peculiar device or on the specific cooldown, conductance step-like behaviour is found in all constrictions as an overall behaviour. Regarding reproducibility of the conductance curves upon different cooldown, it has been observed that thermal cycling between room temperature and base temperature ($0.3\ K$) resulted in a gradual deterioration of the quality of the quantization. As a matter of fact, in some cases reproducible and well-defined steps are found in the conductance, whereas in other cases, the conductance curve is affected by peak-like and dip-like structures resembling those found in the linear conductance curves of Si-based QPCs. A further behaviour found in the measured conductance is the shifting of the pinch-off voltage toward less negative bias voltages in successive thermal cycling (see fig.4.12 (b) and (c)). We have mentioned in the previous chapter that the pinch-off voltage $V_{P.O.}$ depends on the actual potential generated by defects and impurities; in the specific case of $AlGaN/GaN$-based devices, it is dependent on both the barrier layer $AlGaN$ and the quality of the dielectric layer (SiN). During different thermal cycling, the charge configuration of defects and impurities states varies in a non trivial way, producing an inhomogeneous and non reproducible variation of the potential. Given this non-reproducibility of the actual potential, only reproducible structures in the conductance measurements upon different cooldown can be considered intrinsic and caused by the 1D nature of the potential. Therefore differences in the colour curves reported in fig.4.12 (b) and (c) are attributed to different impurities potential distributions. As for the reproducibility of curves from run to run upon the same thermal cycling, only few changes are found in the conductance curves.

The overall picture denotes the following characteristic features: *missing* or *ill-defined plateaus*, *amplitude reduction* of plateaus, *resonance structures* affecting the conductance curves. In the following all these findings will be discussed. From fig.4.12 (a), neglecting the small satellite peaks, which point to the presence of a fine structure requiring further experimental verification, two features are noteworthy: the presence of quantized plateaus at values slightly lower than the expected integer multiples of $G_0 = 2e^2/h$ and the suppression of the third and fifth plateaus. In principle, a $2 \cdot G_0$ jump in the conductance trace can be caused by the presence of a double conduction channel for the electron transport having two 1D energy modes accidentally

degenerate. The double conduction channel can be formed by spatially separated tunnel coupled [33, 137] or spatially coincident [138, 139] 1D electron systems. In each case the presence of a second conduction channel gives rise to a second subladders of discrete 1D energy levels which contribute to the total conductance. Thus, if two transverse modes accidentally line up or are closer in energy than the experimental broadening, as soon as Fermi level crosses them the conductance shows $2 \cdot G_0$ jumps or ill-defined plateaus [33]. In spatially separated 1D channels missing plateaus are found if the phase coherence length exceeds the channel separation. Indeed in ref. [137] Smith et al. reported of the conductance of two parallel QPCs separated by a certain distance, while Roddaro et al. [33] studied the electronic transport of two 1D electron systems separated by a "soft" barrier originating from Coulomb interactions. On the other hand, in spatially coincident 1D electron channels originating from a quasi-2D electron gas the alignment of two particular transverse modes energies depends on the width of the QPCs [138]. However Fischer at al. observed a relative shift of the 1D subladders in the same QPC tuning the confining potential by purely electrostatic means, i.e. by cooling the sample from room temperature to low temperatures applying or not a positive gate bias. As for our case, a second transport channel could originate from the occupancy of the second energy level in the 2DEG, as it has been discussed in the previous section, since the Fermi energy is of the order of 115 meV in this 2DEG. However, as we concluded in the previous section, we can not be completely confident of the occupancy of the second level, therefore, at this stage, it is not possible to find the origin of *missing plateaus*. Moreover, since the lack of plateaus in the linear conductance curve manifests only in this device, the causes likely producing the observed behaviour must be valid locally. Therefore the hypothesis of a double occupancy of the 2DEG appears less plausible if it is not corroborated by other measurements.

Regarding the quantized plateaus found at conductance values smaller than the expected integer values (fig.4.12 (a) and (b)), these are likely imputed to a transmission coefficient lower than unity, due to scattering from impurities [140] or from an irregular geometry of the confining potential. In blue line curves of fig.4.12 (b) *amplitude reduction* has been observed only for even index plateaus (vertical bars indicates amplitude of first four plateaus), whereas odd plateau amplitudes are nearly G_0. A possible explanation of

these observations can be attributed to the presence of an accidental impurity placed off-axis respect to the center of the conduction channel. As a matter of fact, since odd index (even parity) electron wavefunctions $|\Psi|^2$ have their maxima on the axis of the QPC, while even index (odd parity) wavefunctions maxima are off-axis respect to the center of the channel, an impurity placed off-axis would scatter electrons from the second and the fourth modes without affecting electron from the first one [141]. This would reduce the spacing between the first and the second plateau and between the third and the fourth plateau without affecting the height of the first and the third. At higher conductance values broadened plateaus or ill-defined steps are observed in the blue line traces of fig.4.12 (b). High index missing or ill-defined plateaus are probably affected by the non-adiabaticity of the confining potential as the number of occupied modes increases [30]. Red line curve of fig.4.12 (b) presents a series of peaks and dips whose possible origins have been largely discussed in the previous chapter.
Concerning linear conductance curves of fig.4.12 (c), measured on device reported in fig.4.11 (c), these show rather regular steps of conductance with a quite good reproducibility from run to run and in different thermal cycling. The blue line curve manifest two well-developed and flat steps corresponding to conductance values of 1 and 2 G_0 and two less prominent plateaus of smaller amplitudes developing at higher conductances.

4.2.1 Deliberately asymmetric confining potential in QPCs

In order to understand the origins of the structures found in the linear conductance curves reported in fig.4.12, we performed an experiment in which we have deliberately introduced an asymmetry in the confining potential by means of a finite bias applied between the two split-gates. The method of differentially biasing the two halves split gates has been used for different purposes. Firstly, it allows to move the channel: scanning the confining potential it is possible to probe the presence of impurities or the formation of a quasi-bound state in the channel [142, 143]. Secondly, these studies are also a suitable tool to investigate the effect of variation of the transverse confining potential in terms of the shape of the parabolic well [144]. Indeed, by introducing the asymmetry, the number of modes contributing to the conduction varies and the well becomes shallower and shallower as the

asymmetry is increased.

In order to investigate the effect of the asymmetry of the transverse confining potential on the electronic transport, we have performed linear conductance measurements by differentially biasing both gates by ΔV_g, $V_{g1} = V_g + \Delta V_g/2$ and $V_{g2} = V_g - \Delta V_g/2$. In the following we will present all data acquired on the devices of fig.4.11 (b) and (c) relative to the linear conductance $G(V_g)$ as a function of V_g and ΔV_g. Several ways of visualization of data are shown in order to give a complete picture of the conductance behaviour. Figure 4.13 shows the conductance characteristics of device B as a function of V_g, upon varying the gate voltage difference, $\Delta V_g = V_{g1} - V_{g2}$, from $-20\ V$ (green line in fig.4.13 (a)) to zero (blue line), up to $+20\ V$ (red line in fig.4.13 (b)). The increment of ΔV_g between curves is $0.4\ V$. In order

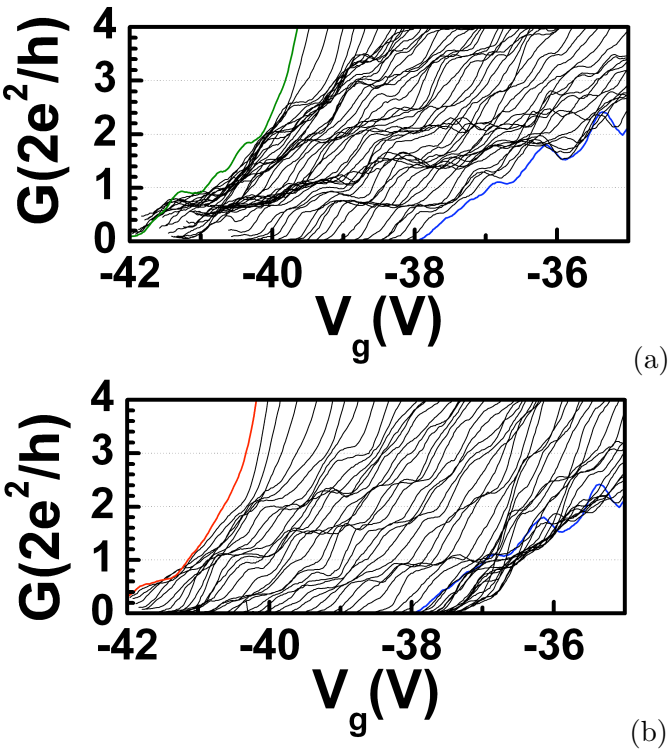

Figure 4.13: Linear conductance traces of device B as a function of V_g, sweeping ΔV_g from -20 V (green line in panel (a)) to zero (blue line in both panels) until +20 V (red line in panel (b)). Curves are horizontally shifted of a quantity equal to $0.144\ V$.

to better visualize the evolution of the conductance structures reported in fig.4.13, we also performed the numerical derivative dG/dV_g. In the colour

maps of fig.4.14 dG/dV_g is reported for two runs of the same measurement carried out in different cooldowns from liquid helium temperature to 0.25 K. In the colour map the orange regions are peaks whereas the green ones

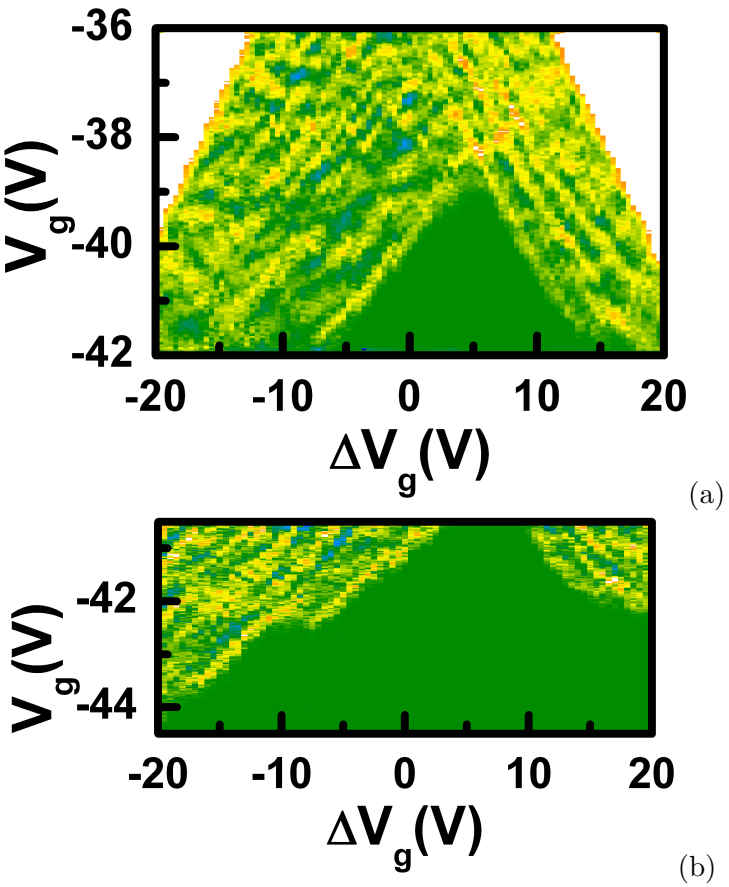

Figure 4.14: (a) and (b) Colour map of transconductance, dG/dV_g, as a function gate voltage difference, ΔV_g, and average gate voltage, V_g for two different thermal cycling. Data of panel (a) are relative to conductance curves of fig.4.13. Conductance data relative to transconductance of panel (b) are not shown.

are zeros of the transconductance traces. The former indicate transition edges between plateaus, the latter correspond to flat plateaus. The derivative dV_g/dG is an additional useful tool to follow the amplitude evolution of the conductance plateaus as a function of ΔV_g. In the colour map of fig.4.15 (dV_g/dG) yellow regions indicate where plateaus of the $G(V_g)$ traces are positioned in the $G - \Delta V_g$ plane.

In figure 4.16 we report results obtained from a similar measurement on

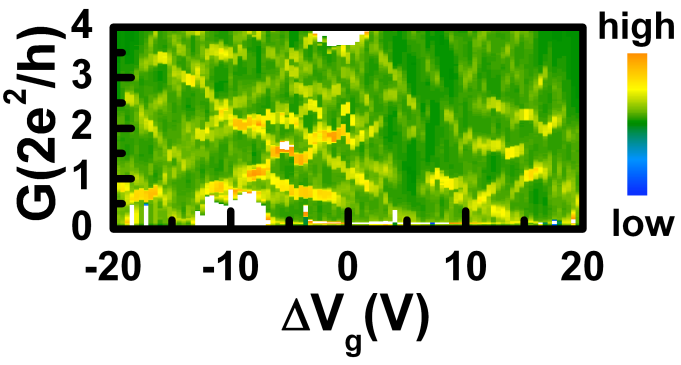

Figure 4.15: Colour map plot of dV_g/dG as a function of ΔV_g and G. Yellow parts are regions where the conductance is flat, that is where a plateau is located in the plane $\Delta V_g - G$.

device C. In panels (a) and (b) of fig.4.16 the conductance traces $G(V_g)$ are reported for ΔV_g ranging from -20 V (green line curve) to zero (blue line curve) and from +20 V (red line curve) to zero (blue line curve). Each curve has been taken for a ΔV_g value increasing with steps of 0.5 V. Traces are horizontally shifted of 0.175 V. The colour maps of panel (c) and (d) of the same figure represent the transconductance dG/dV_g as a function of ΔV_g and V_g and the derivative dV_g/dG as a function of ΔV_g and G.

The measurements reported and carried out by introducing an asymmetry in the transverse potential (fig.4.13, 4.14, 4.15 and 4.16) reveal a complex behaviour of the conductance. Nevertheless, the presence of similar features in different devices suggests that the observed evolution arises from intrinsic effects rather than from a random impurities distribution. Though a confident and complete interpretation of these findings has not been found yet, a detailed description of the reproducible features will be given in the following, focusing on the possible explanations for the results obtained.
The linear conductance curves of fig.4.13 and fig.4.16 show an overall quantized conductance with step-like structures changing their amplitude (G value) and moving in energy (onset V_g position) in a non trivial way as ΔV_g is swept. The mentioned characteristics produce peculiar patterns in the transconductance plot of figure 4.14 and fig.4.16 (c) and in the derivative dV_g/dG of fig.4.15 and fig.4.16 (d). As for the transconductance data reported in fig.4.14 and fig.4.16 (c) for device B and C, we point out the follow-

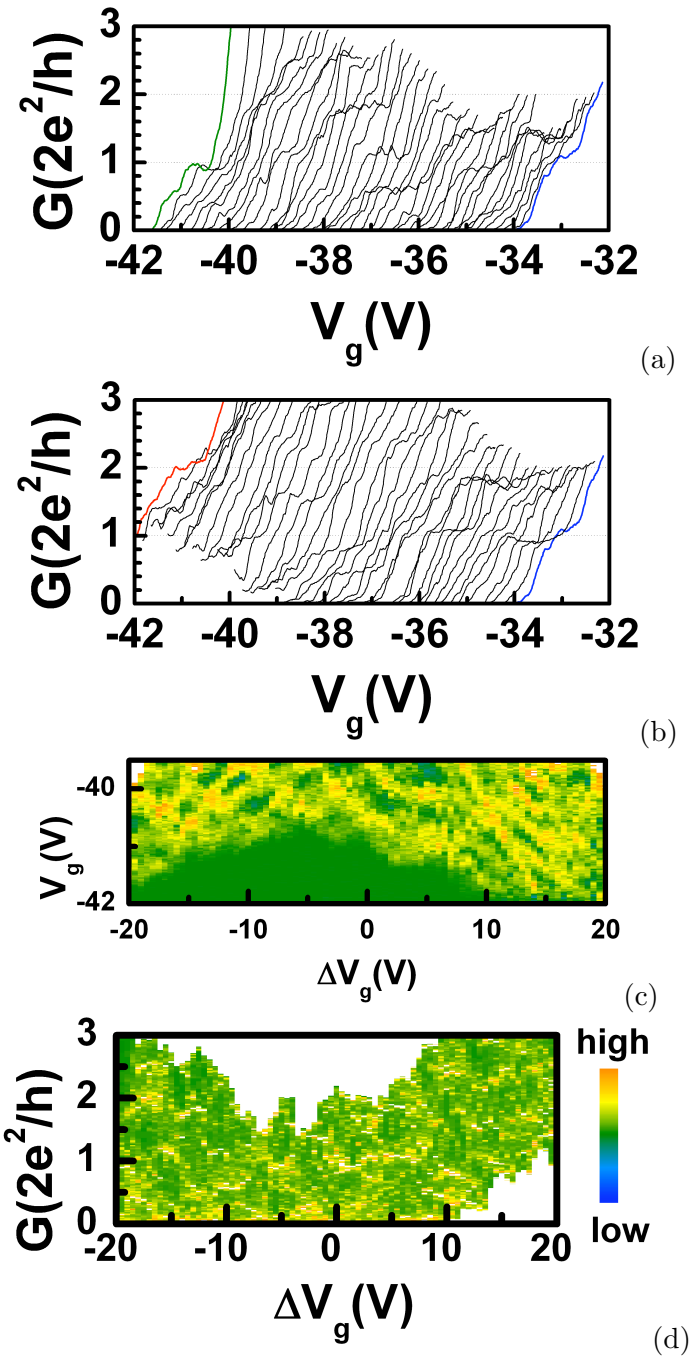

Figure 4.16: (a) and (b) $G(V_g)$ traces for device C as ΔV_g is varied from -20 V (green line), to zero (blue line) until +20 V (red line). Curves are horizontally shifted of 0.175 V. (c) Colour map of transconductance, dG/dV_g, as a function of ΔV_g and V_g. (d) Colour map of the dV_g/dG as a function of ΔV_g and G.

ing features: as the asymmetry between gates (ΔV_g) is swept, the pinch-off voltages vary almost linearly with the absolute value of ΔV_g. However the minimum value of the conductance onset does not occur for $\Delta V_g = 0$ but for $|\Delta V_g| \approx 5\ V$ (both in fig.4.14 and in fig.4.16 (c)), indicating that the condition $\Delta V_g = 0$ does not strictly correspond to a symmetric confining potential profile. Moreover the quantized conductance plateaus do not run parallel to ΔV_g axis, evolving linearly as this quantity is varied.
To explain the non trivial evolution of the pinch-off voltages as a function of ΔV_g, we consider the energy diagram reported in fig.4.17 which simply describes the effect of introducing an asymmetry in the confining transverse potential applying ΔV_g between the two gates. Indeed, as long as a negative bias is applied to both fingers of a split-gate QPC (like those of fig.4.11), the confining potential is transversely symmetric (see fig.4.17 (a), (b) and (c)). Consider V^* to be the gate voltage for which the chemical potentials of the metallic gate electrodes are lined up to the Fermi energy of the 2DEG, i.e. the electrons gas is completely depleted underneath the gates. When $|V_g| \gtrsim V^*$, a constriction for electrons starts to form in the y-direction and quantization of conductance is expected as a manifestation of quantized energy levels due to the transverse confinement. As a matter of fact, we have measured quantized plateaus whose conductance values have been shown to be slightly suppressed by transmission coefficients below the unity in some cases (fig.4.12). As soon as an imbalance ΔV_g is applied between the two gates, the parabolic transverse potential becomes asymmetric (see fig.4.17 (d) and (e)). Starting from a fixed value of V_g, for instance $V_g = V^0_{P.O.}$ in panel (c) of fig.4.17, applying ΔV_g (fig.4.17 (e)) has the effect of raising the energy level relative to V_{g1} and lowering the one relative to V_{g2} respect to the energy level identified with an orange dashed line, $V^0_{P.O.}$, in fig.4.17 (e). The orange dashed line in fig.4.17 (e) corresponds to the energy levels of the two gates when $|V_{g1}| = |V_{g2}| = V^0_{P.O.}$ (see panel (c) of fig.4.17). In panel (e) the potential profile for the case $|V_{g1}| = |V_{g2}| = V^0_{P.O.}$ (of panel (c)) has been reported too as a dashed line. Furthermore, ΔV_g acts laterally, depleting the 2DEG less near V_{g2} and more near V_{g1}, for the case of fig.4.17 (e)). This has twofold effect: firstly it lowers the bottom of the asymmetric confining potential, defining a 'new' pinch-off voltage, $V^{\Delta V_g}_{P.O.} = V_{P.O.} + \alpha(|\Delta V_g|)$; secondly it transversely shifts the conducting channel. Indeed as ΔV_g is increased the minimum of the confining potential is spatially varied of a

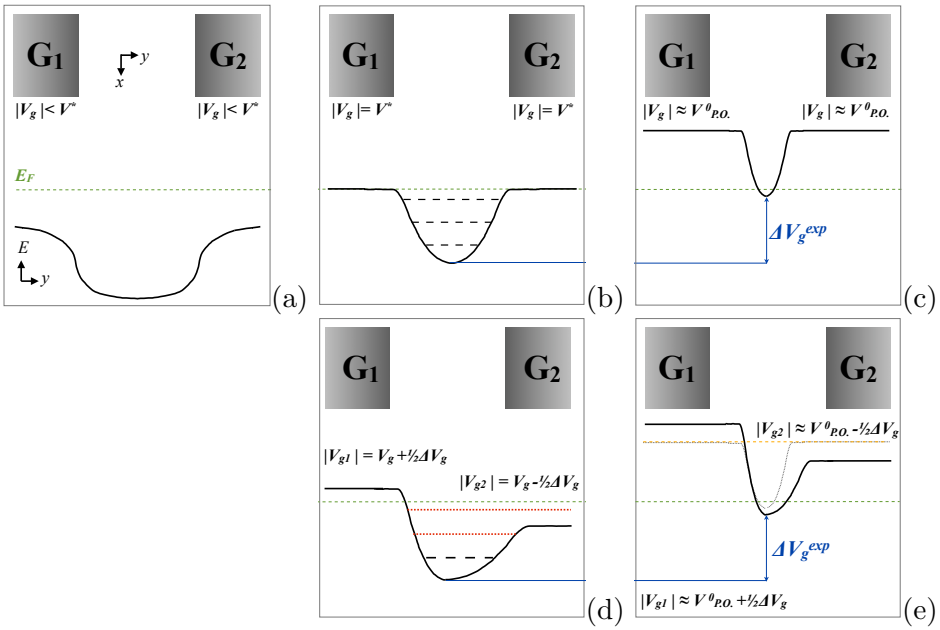

Figure 4.17: Energy diagram of the transversal confining potential for different values of the gate voltage: (a) $|V_g| < V^*$, (b) $|V_g| = V^*$, (c) $|V_g| \approx V^0_{P.O.}$, (d) $|V_{g1}| = V_g + \frac{1}{2}\Delta V_g$ and $|V_{g2}| = V_g - \frac{1}{2}\Delta V_g$ for gate G_1 and G_2, respectively, (e) $|V_g| \approx V^0_{P.O.} + \frac{1}{2}\Delta V_g$ and $|V_g| \approx V^0_{P.O.} - \frac{1}{2}\Delta V_g$ for gate G_1 and G_2, respectively.

quantity $y = \eta(V_{g1} - V_{g2})/(V_{g1} + V_{g2})$ where η is a positive constant [145]. This explains the suppression of the resonant-like features in the $\Delta V_g \approx 0$ linear conductance curves in fig4.13 with increasing ΔV_g. Indeed, electron scattering due to some accidental impurity in the channel can be reduced shifting the confining potential laterally so that electrons are not scattered anymore.

Upon decreasing the negative gate voltages on both gates (from panel (e) to (d) of fig.4.17), a new configuration of confining potential and distribution of transverse modes is found compared to the case of panel (b). Being the shape of the confining potential shallower, due to the less negative electrode, energy spacing between modes decreases. Furthermore, a smaller number of quantized levels can form in the well. Note, indeed, that as the imbalance between V_{g1} and V_{g2} is such that one branch of the potential profile drops below E_F (V_{g1} or $V_{g2} < V^*$), the electrode is no more effective in depleting the 2DEG underneath (see fig.4.17 (d)), and, as a consequence, the confining potential become shallow at a less negative voltage bias. Under this conditions, less and less 1D quantized levels form in the well before the 1D electron system switches into a 2D system [27]. As a consequence, the $G(V_g)$ traces of both device B and C show that the experimental V_g sweep range decreases as $|\Delta V_g|$ is increased, manifesting a rapid divergence of conductance for a large imbalance between the gates (see green and blue line curves of fig.4.13 and fig.4.16 (a) and (b)). This behaviour is clearly caused by the decrease of the number of transverse modes which form as the asymmetry is made stronger and stronger.

In the following we will focus on a detailed description of fig.4.13 identifying some ΔV_g regions for the different typologies of conductance behaviour, starting from the experimental symmetric condition, i.e. $\Delta V_g = 5\ V$. In fig.4.18 we report two particulars of data in fig.4.13: in panel (a) and (b) five conductance curves are shown for ΔV_g ranging in the interval reported inside the graphs. A feature is noteworthy: note the lack of the first quantized plateau at $G \approx G_0$ in the $\Delta V_g \approx 5\ V$ curves showing a $G \approx 2G_0$ step, indicated by a red arrow in both panels. These structures evolve towards multiple integers of G_0, indicated by blue arrows. As mentioned in the previous section, this behaviour is likely a manifestation of the degeneracy of two energy levels belonging to two different subladders originating from the occupancy of the second excited level of the quantum well.

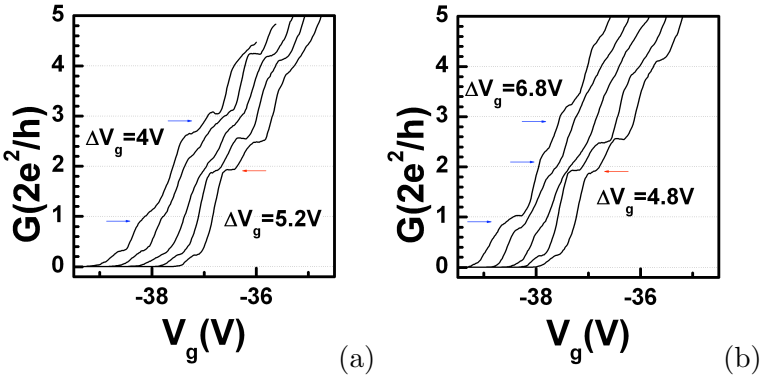

Figure 4.18: (a) and (b) Some of the $G(V_g)$ traces of fig.4.13: (a) $\Delta V_g = (4 \div 5.2)$ V, curves are horizontally shifted of 0.375 V. (b) $\Delta V_g = (6.8 \div 4.8)$ V, curves are horizontally shifted of 0.25 V.

The description of the curves which follows is separated into two ΔV_g intervals respect to the $\Delta V_g \approx 5$ V condition. The intervals of each panel has been chosen symmetrically respect to that condition. Coloured dashed lines are a guide for the eye. Starting from $\Delta V_g = -9.2$ V toward $\Delta V_g = -4.8$ V, in panel (a) of fig.4.19, the presence of a step-like plateau at about 0.6 G_0 evolving toward 0.5 G_0, as $|\Delta V_g|$ is changed, is apparent. The structure at $\sim 1G_0$ remains nearly at the same conductance value for a small ΔV_g interval and then splits into two at about 0.7 and 1.5 G_0. A plateau like structure at $G \approx 2G_0$ is always present in this ΔV_g range. In panel (b) of

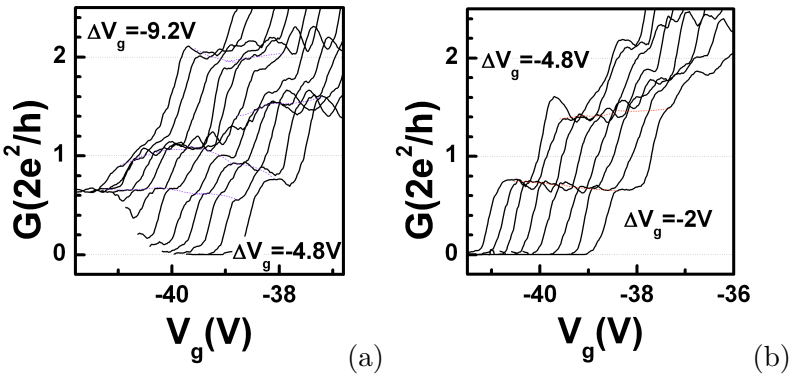

Figure 4.19: (a) and (b) Some of the $G(V_g)$ traces of fig.4.13: (a) $\Delta V_g = (-9.2 \div -4.8)$ V, curves are horizontally shifted of 0.23 V. (b) $\Delta V_g = (-4.8 \div -2)$ V, curves are horizontally shifted of 0.24 V.

fig.4.19 the 0.7 G_0 structure, whose amplitude slightly decrease to 0.65 G_0,

is approximately unchanged as $|\Delta V_g|$ is lowered from $\Delta V_g = -4.8$ to -2 V becoming a prominent flat step. Further decreasing $|\Delta V_g|$ from $\Delta V_g = -2$ to 0.8 V, in fig.4.20 (a), the flat plateau at 0.7 G_0 starts to decrease toward a less prominent structure at 0.3 G_0, while the shoulder at about 1.5 G_0 lowers to 1 G_0. In fig.4.20 (b), from $\Delta V_g = 0.8V$ to $\Delta V_g = 4V$, the 1 G_0

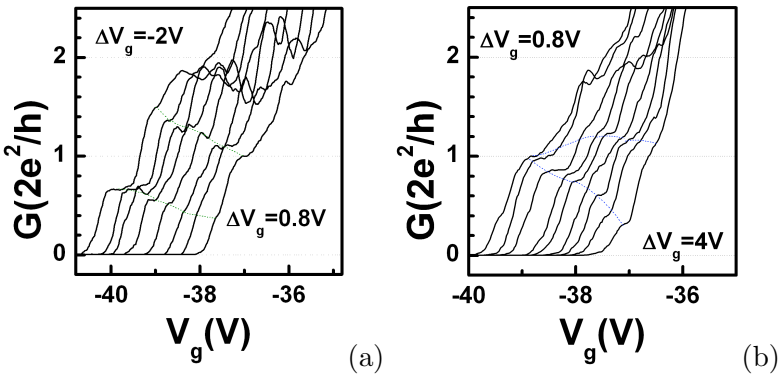

Figure 4.20: (a) and (b) Some of the $G(V_g)$ traces of fig.4.13: (a) $\Delta V_g = (-2 \div 0.8)$ V, curves are horizontally shifted of 0.26 V. (b) $\Delta V_g = (0.8 \div 4)$ V, curves are horizontally shifted of 0.19 V.

plateau first begins to increase, then comes back to the 1 G_0 shoulder indicated by a blue arrow in fig.4.18 (a). Contemporarily, a lower structure at 0.3 G_0 emerges from the splitting of the 1 G_0 plateau of the $\Delta V_g = 0.8$ V curve.

Going on symmetrically in the other ΔV_g interval, a 0.5 G_0 step in the $\Delta V_g = 20$ V curve of fig.4.21 (a) moves toward 1.1 G_0 plateau-like in the $\Delta V_g = 15.6$ V curve; concomitantly, a nearly 2 G_0 structure develops as ΔV_g is decreased. Note, indeed, that in the $\Delta V_g = 20$ V curve only a step is present in the conductance curve, indicating that just one quantized energy level forms in the constriction. As already mentioned, this occurs when a branch of the parabolic transverse potential drops below the Fermi energy and the electrons are no more confined in that direction. On the other hand, by further decreasing ΔV_g (fig.4.21 (b)), the 1.1 G_0 plateau lowers while a shoulder at about 0.3 G_0 develops. In the same ΔV_g interval it is evident the formation of a 1.5 G_0 plateau which remains approximately constant upon changing ΔV_g. This structure persists in fig.4.22 (a) and (b), up to $\Delta V_g \approx 10V$, then moves and disappear (in the G interval reported in figure). The structure just below 1 G_0 fig.4.22 (a) evolves toward the 0.5 G_0 ones,

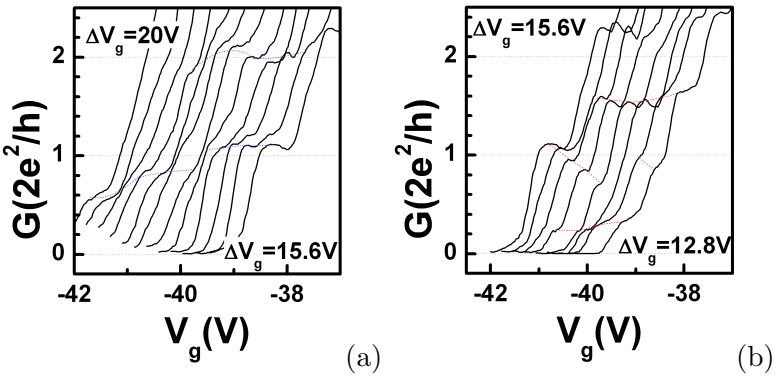

Figure 4.21: (a) and (b) Some of the $G(V_g)$ traces of fig.4.13: (a) $\Delta V_g = (20 \div 15.6)$ V, curves are horizontally shifted of 0.23 V. (b) $\Delta V_g = (15.6 \div 12.8)$ V, curves are horizontally shifted of 0.24 V.

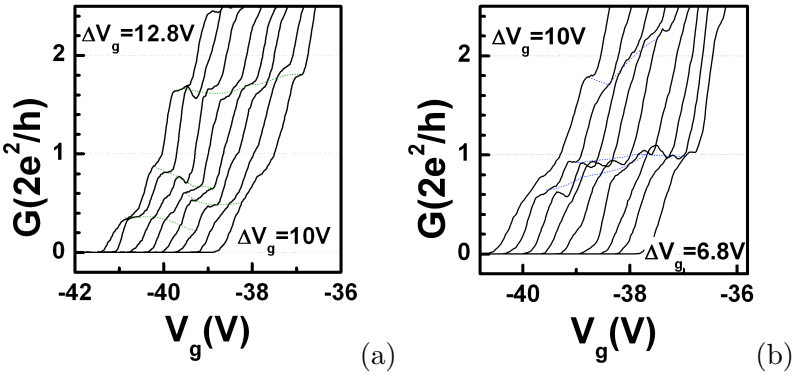

Figure 4.22: (a) and (b) Some of the $G(V_g)$ traces of fig.4.13: (a) $\Delta V_g = (12.8 \div 10)$ V, curves are horizontally shifted of 0.26 V. (b) $\Delta V_g = (10 \div 6.8)$ V, curves are horizontally shifted of 0.19 V.

whereas the shoulder at about 0.3 G_0 is constant for a small ΔV_g range, afterwards it lowers and disappears. Lastly, in fig.4.22 (b) the formation of the 1 G_0 plateau depicted by a blue arrow in fig.4.18 (b) is evident.

The overall framework of plateau evolution with the applied ΔV_g is rather complex. As stated previously, the experiment has been performed to check the presence of impurities: by shifting the minimum of the potential profile away from the centre of the channel, the peaks, affecting the linear conductance curve for $\Delta V_g = 0$, disappear. However we have shown that the applied ΔV_g has the further effect of changing the potential profile giving rise to new configurations of the 1D energy modes inside the constriction. Summarizing the found behaviour, we have observed that in the physical symmetric potential condition (occurring for $\Delta V_g \approx 5\ V$), the 1 G_0 plateau does not manifest, suggesting the possibility of two modes degeneracy. As $|\Delta V_g|$ is varied a gradual evolution of the plateau structures occurs: first the formation of the G_0 plateau and then the occurrence of structures at about 0.5 G_0. This complicated framework is compatible with the occupancy of the second energy level of the 2DEG (to be confirmed by further investigations on the 2DEG). The application of ΔV_g, by modifying the confining potential profile, contributes to change the relative alignment of the two subladders, which forms in the channel as a result of the quantum confinement. As a consequence, under certain conditions, the 1D modes belonging to the two 2D energy levels of the 2DEG misalign and the $1 \cdot G_0$ plateau forms.

Concerning the appearance of a 0.5 G_0 plateau in different ΔV_g intervals, this finding points to the occurrence of a zero-field spin polarization. With regard to this finding, it is worth citing ref.[144]. The authors proposed an experiment where the side gates of a $InAs$ QPC were differentially biased with a dc voltage in order to get an asymmetric transverse confinement potential. They measured a robust zero-field 0.5 G_0 plateau at finite ΔV_g and a regular quantization at $\Delta V_g = 0$. The interpretation proposed for the zero-field spin polarization was in terms of a lateral spin-orbit coupling (LSOC). Indeed, similarly to the Rashba SOC (eq.4.4), the gradient of the confining potential of a QPC, produced by differentially biasing the two gates, generates a transverse electric field resulting in a lateral spin-orbit coupling. The LSOC interaction term can be written as $H_{SO} = \alpha_{so}\vec{\sigma} \cdot [\vec{\nabla}U(y) \times \vec{k}_x]$, where α_{so} is the intrinsic spin orbit parameter (eq.4.5). It induces an effective magnetic field $\vec{B}_{SO} = \alpha_{so}[\vec{\nabla}U(y) \times \vec{k}_x]$ where k_x is the propagation vector

along x-direction and $\vec{\nabla}U(y)$ is the spatial gradient of the confining potential along the y-direction. The effective magnetic field along the z-axis has exactly the same magnitude but opposite direction at the transverse edges of the QPC, see fig.4.23 (a), for the case of symmetric side-gate voltage. Moving electrons with opposite spin experience opposite SOC forces that

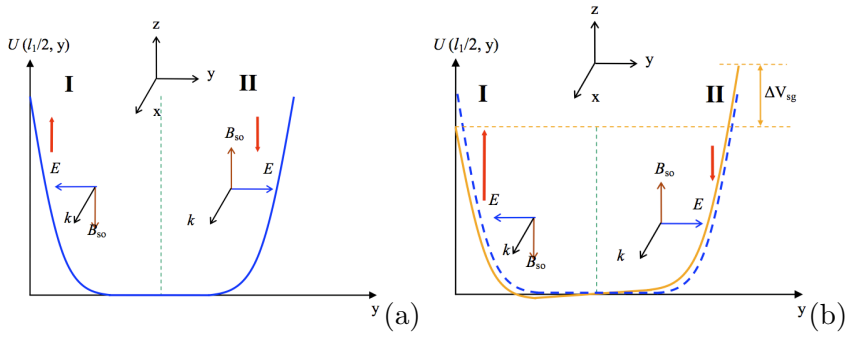

Figure 4.23: (a) Schematic representation of the confining potential energy of a QPC along y direction when symmetric side-gate voltages are applied; (b) same for asymmetric side-gate voltages, from [144].

lead to an accumulation of opposite spins at the opposite transverse edges. In this case there is an equilibrium between the number of spin-up and spin-down at the opposite sides of the QPC. Instead a net spin polarization occurs when the asymmetric gate voltage is applied so that a net imbalance between spin-up and spin-down at the opposite QPC edges results, fig.4.23 (b).

Although large similarity to our results is found in the cited work, the most intriguing features of our measurements are found in the magnetic field behaviour.

In the following section we present the conductance behaviour as a function of the external magnetic field, for different configurations of the confining potential profile. Firstly, we illustrate the conductance curves evolution by varying the field in the case of $\Delta V_g = 0$ for both devices B and C, and then we present different ΔV_g situations in presence of external magnetic field for devices B.

4.2.2 Magnetic field measurements

In the following figures linear conductance spectra taken at increasing perpendicular magnetic field from zero (blue line) to 12 T (green line) with step of 0.1 T are reported for device C, fig.4.24, and B, fig.4.25. In fig.4.26 linear conductance data are reported with increasing parallel magnetic field from zero (blue line) to 12 T (green line) with step of 0.1 T for device B. In fig.4.24 (a) $G(V_g)$ traces are horizontally shifted of 0.05 V for clarity. In panels (b) and (c) transconductance, dG/dV_g as a function of both magnetic field, B, and V_g along with dV_g/dG as a function of magnetic field, B, and conductance, G, are shown, respectively. Figure 4.24 reports the evolution of the first quantized conductance plateau in presence of the external field. Clearly in fig.4.24 (a) and (c) the 1 G_0 plateau splits into two structures at about 0.5 and 1.5 G_0. We interpret these findings as the energy splitting of the two spin-degenerate subbands due to the Zeeman effect. From the observed energy splitting of the spin-non degenerate levels, fig.4.24 (b), an energy conversion factor can be calculated from gate voltage to energy, $\Delta E = \eta \cdot \Delta V_g$. Since for $B = 12\ T$, $\Delta E = g^* \mu_B B = 1.3\ meV$ (for $g^* = 2$), we obtain a conversion factor $\eta \approx 2\ meV/V$. This gives roughly an estimate of the change in energy once the gate is being swept, suggesting that typical energy spacing between modes is of the order of 2.2 meV (comparison with fig.4.12 (c)).

On the contrary, we were not able to measure Zeeman spin splitting in device B neither in perpendicular magnetic field (fig.4.25), nor in parallel magnetic field (fig.4.26), up to intensity of 12 T. Linear conductance data of fig.4.25 and fig.4.26 show again two well-defined structures at 1 and about 2 G_0 whose V_g positions are almost unchanged (a slight shift of the transition edge of the $1G_0$ plateau is seen in fig.4.26). Therefore, there is no evidence of half-integer plateaus arising from spin-split levels in an applied magnetic field in device B. The results differ from prior reports which point to a strong polarization at fields well below 12 T, clear manifestation of Zeeman effect [7, 146]. To date a similar behaviour has not been found yet. Actually, suppression of spin-splitting in presence of magnetic field has been reported by Timothy E. Day et al. [147]. However the authors performed their experiment using an hybrid magnetic QPC with Co lateral gates in a $AlGaAs/GaAs$ 2DEG. They claimed that the lack of spin-split plateaus could be due to a suppression of the electron-electron interactions

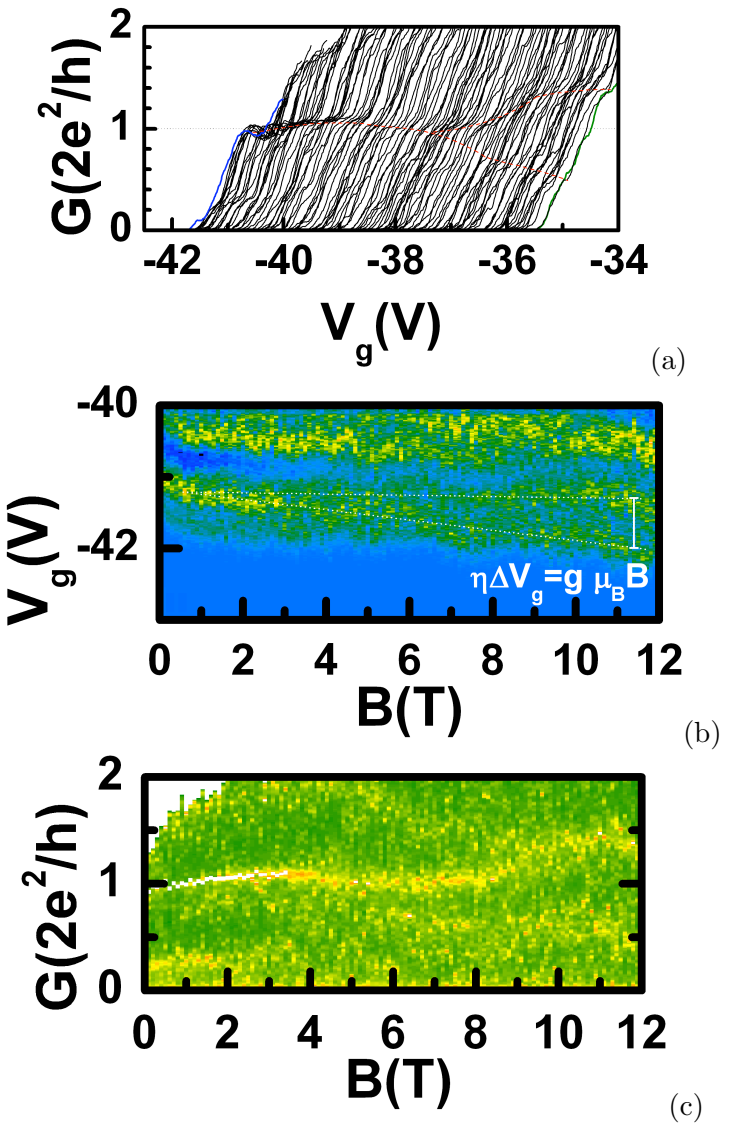

Figure 4.24: Linear conductance $G(V_g)$ for perpendicular magnetic field ranging from 0 to 12 V. (a) $G(V_g)$ curves are horizontally shifted of 0.05 V, magnetic field ranges from zero (blue line) to 12 T (green line), with step of 0.1 T. (b) Transconductance dG/dV_g in the $B - V_g$ plane. (c) Inverse transconductance dV_g/dG in the $B - G$ plane.

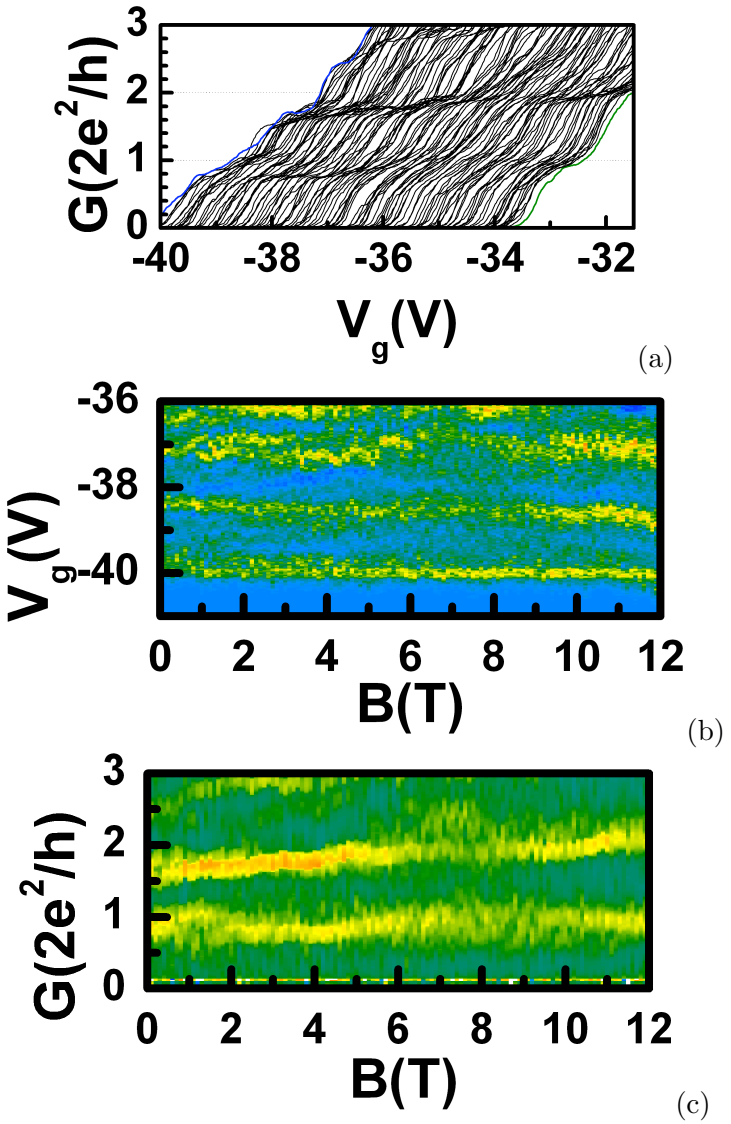

Figure 4.25: Linear conductance $G(V_g)$ for perpendicular magnetic field ranging from 0 to 12 V. (a) $G(V_g)$ curves are horizontally shifted of 0.05 V, magnetic field ranges from zero (blue line) to 12 T (green line), with step of 0.1 T. (b) Transconductance dG/dV_g in the $B - V_g$ plane. (c) Inverse transconductance dV_g/dG in the $B - G$ plane.

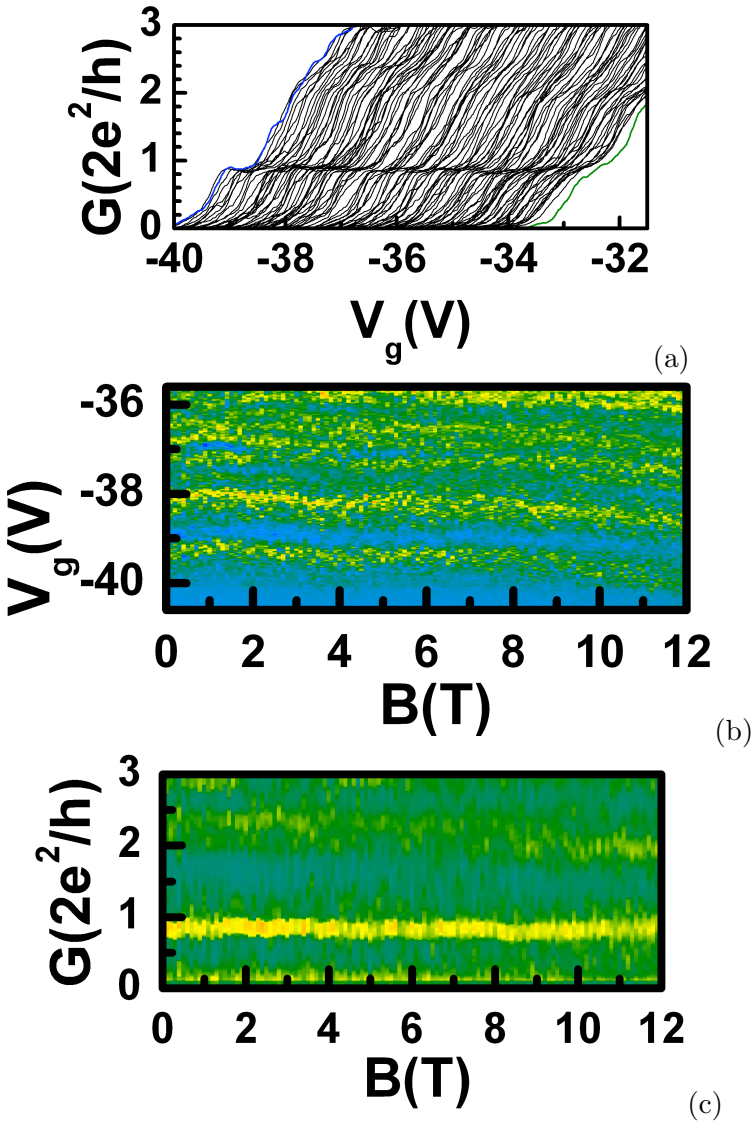

Figure 4.26: Linear conductance $G(V_g)$ for parallel magnetic field ranging from 0 to 12 V. (a) $G(V_g)$ curves are horizontally shifted of 0.05 V, magnetic field ranges from zero (blue line) to 12 T (green line), with step of 0.1 T. (b) Transconductance dG/dV_g in the $B - V_g$ plane. (c) Inverse transconductance dV_g/dG in the $B - G$ plane.

in the QPC, which limits the enhancement of the electron g-factor. As for our device, there are no magnetic gates able to shield the external applied magnetic field. One reason for the anomalous behaviour can be that the energy interval swept with the gate is much greater than the spin splitting energy at $B = 12\ T$ for device B. However this would imply that also the energy spacing between 1D modes is much greater than few meV (being $\Delta E = g^* \mu_B B = 1.3\ meV$ at $B = 12\ T$). This appears unlikely since we have obtained through a rough estimate a value of few meV for the energy spacing between 1D modes for the case of device C. In our opinion the origins of the singularities in our device should be searched to a large extent into the elevated value of the sheet carrier density $n_{2D} \sim\ 10^{13}\ cm^{-2}$. In fact, to date, the only experimental works on mesoscopic devices realized on these systems (GaN-based 2DEG) report samples with well lower electron densities ($n \approx 1 \times 10^{12}\ cm^{-2}$ in ref.[148] and $n \approx 0.8 \times 10^{12}\ cm^{-2}$ in ref.[149]). Indeed, the high electron density and the low mobility (compared to those obtained in $III - V$ semiconductors heterostructures) can make motion inside the channel quasi-ballistic: we have shown in chapter 1 that if the Fermi wave-length, λ_F, is comparable with the roughness size of the boundaries, these are supposed to behave as diffusive boundaries and effectively act as a scattering source. As a matter of fact, for our device $\lambda_F \approx 7.7\ nm$ which is the same order of magnitude of typical roughness size of metallic gates.

In the following the effect of an external magnetic field has been studied for some of the experimental situations described in section 4.2.1.
In fig.4.27 linear conductance trace for $\Delta V_g = -4\ V$ (see fig.4.19 (b)) has been investigated for an increasing parallel magnetic field in the $(0 \div 10)\ T$ range. Each curve in fig.4.27, from 0 (blue line curve) to 10 T (green line curve), has been horizontally shifted of 0.275. In fig.4.28 the $G(V_g)$ characteristics have been investigated for a fixed value of the external parallel magnetic field equal to 5 T, varying ΔV_g from -25 to 15 V. Increments of ΔV_g are of 0.2 V each. Moreover, curves are horizontally shifted of 0.063 V for clarity. As for the data presented in fig.4.27, linear conductance measurements reveal the presence of a 0.7 G_0 plateau which remains almost constant in energy and amplitude though a small shoulder develops at 0.5 G_0 for $B = 10\ T$ (green line curve). Similarly a plateau at 1.5 G_0 is found

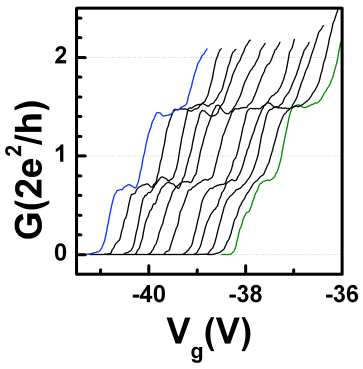

Figure 4.27: Differential conductance data $G(V_g)$ gathered for $\Delta V_g = -4\ V$ with increasing the external parallel magnetic field from zero (blue line) to 10 T (green line). Curves are horizontally shifted of 0.275 V

which remains unchanged upon varying the field. These features suggest that spin-split plateaus form in the $G(V_g)$ curves under certain conditions of the potential profile (ΔV_g) in zero-magnetic field. As a matter of fact, as reported in ref.[144], a parallel magnetic field should have hardly any influence on the spin-polarized plateaus, indicating fully polarized state.
Concerning the measurements reported in fig.4.28, it is not possible to compare singularly these curves with those reported in fig.4.13 since the various confining potential configurations, corresponding to a point in the plane $\Delta V_g, V_g$, giving rise to the peculiar evolution of the conductance traces, occur for different values respect to those of measurement of fig.4.13, i.e. a different couple of the values $(\Delta V_g; V_g)$ due to the observed hysteresis in the gate voltage. Compare, for instance, fig.4.14 with fig.4.28 (c). For this reason a qualitative discussion is only possible. The transconductance pattern found in presence of a parallel magnetic field, reported in fig.4.28 (c), strongly resembles that of fig.4.14: the linear evolution of the pinch-off voltages with increasing ΔV_g and the minimum value of the pinch-off voltage occurring for $\Delta V_g \neq 0$ are the same already shown in absence of magnetic field, though the numerical values differ from those previous reported in fig.4.14. The $G(V_g)$ spectra of fig.4.28 (a) and (b) reveal the presence of steps in the curves moving toward half integers of G_0. The overall framework of the evolution of steps in conductance is similar to the same measurement in zero-field however the development from integers to half-integers of G_0 and vice versa is more clearly visible in presence of the external magnetic

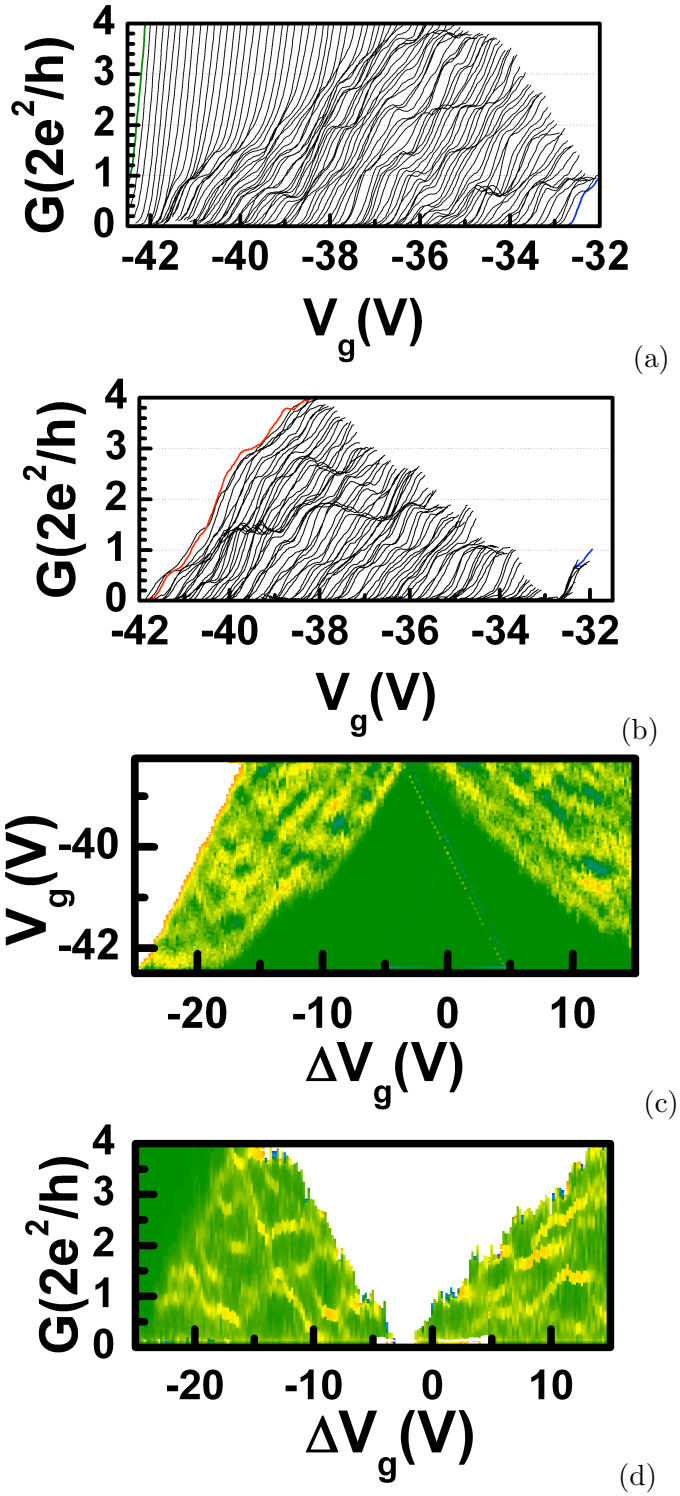

Figure 4.28: (a) and (b) $G(V_g)$ traces for device B as a function of ΔV_g for a fixed parallel magnetic field $B = 5\ T$. (a) $\Delta V_g = (-25 \div -5)\ V$, from green line to blue line curve. (b) $\Delta V_g = (-5 \div 15)\ V$, from blue line to red line curve. ΔV_g increases of $0.2\ V$. Curves are horizontally shifted of $0.063\ V$. (c) Colour map of transconductance, dG/dV_g, as a function of ΔV_g and V_g. (d) Colour map of the dV_g/dG as a function of ΔV_g and G.

field (see fig.4.28 (c)). By further investigating the conductance spectra with finite ΔV_g, we have again the same behaviour of the conductance, without any apparent spin-splitting of the G_0 integers plateaus.

However if both hypothesis, the presence of a double subladder of energy levels and the possibility of a fully spin-polarized state as due to the asymmetry of the confining potential [144], are confirmed, the occurrence of a 1 G_0 step (without the 0.5 G_0 plateau) is not surprising. In this case, indeed, the G_0-integers plateaus would result from the alignment of two spin-polarized states belonging to two different levels of the 2DEG.

In fig.4.29 three groups of curves of fig.4.28 have been reported in detail showing the formation of a 0.5 G_0 plateau (panels (a) and (c)) and of a 1 G_0 plateau (panel (b)) due to the applied asymmetry.

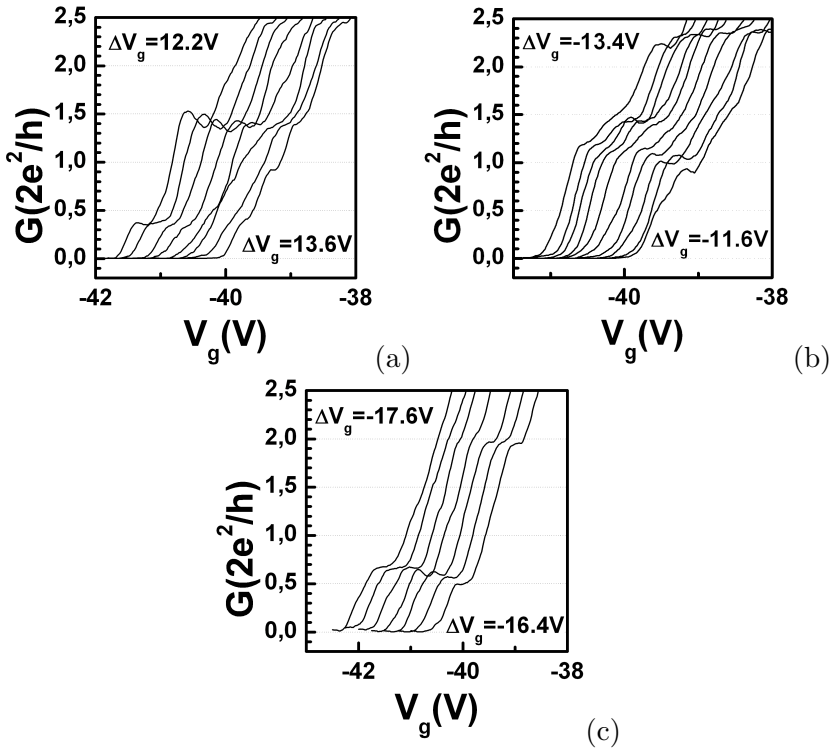

Figure 4.29: Some of the $G(V_g)$ traces of fig.4.28: (a) $\Delta V_g = (12.2 \div 13.6)\ V$, curves are horizontally shifted of 0.23 V. (b) $\Delta V_g = (-13.4 \div -11.6)\ V$, curves are horizontally shifted of 0.05 V. (b) $\Delta V_g = (-17.6 \div -16.4)\ V$, curves are horizontally shifted of 0.25 V.

Similarly to our study, several experimental works have been carried out in which the dependence of the confining potential on the electronic transport has been investigated by using different methods [150, 151, 152, 73, 144]. In all these work e-e interaction effects were supposed to play a fundamental role, and in particular, in ref. [150, 151, 152] and [73], the utmost important parameter of the investigation was the electron sheet density.

Thomas et al. [150] studied the electron transport of a 1D channel where the carrier density was parametrically varied by means of a top metallic gate (fig.4.30 (a)). It has been concluded that a complete spin-polarization was promoted at low densities, when the e-e interactions are supposed to be stronger. In addition their measurements confirm that the presence of disorder is crucial in the formation of a spin-polarized state since they claim that the spontaneous polarization is induced by weak disorder.
The possibility of a spontaneous spin polarization of electrons in a 1D channel has been debated for a long time. While Lieb and Mattis theorem [153] asserts the ground state of a 1D system of electron to be unmagnetized, theoretical [152] and experimental [150] works confirm that this is not true for a real 1D wire. Andreev and Kamenev demonstrate that for $d \leq 2$ a disordered system may exhibit a finite temperature partial spin polarization even if its clean analog is paramagnetic [154].
Still, Pyshkin and coauthors [151] reported of a 0.7 structure evolving into a fully polarized state as the electron density is lowered by means of a top gate (fig.4.30 (b)). The model proposed for the experimental evidences ascribes the evolution of the 0.7 structure into the 0.5 plateau to a breaking of the spin degeneracy driven by exchange interactions. At the same time they found a 0.5 structure in the conductance trace at the highest density value of the explored range whose origin however was not clear (fig.4.30 (b)).
On the contrary in ref.[152] a 0.5 spin-polarized plateau was found at high density in ultra low-disorder long quantum wires (fig.4.30 (c)).
While we are confident that even in our experiment a finite difference between the split gates bias affects the confining potential reducing the electron density as ΔV_g is raised, in the cited experimental works a radically different evolution of plateaus was found. The equilibrium linear conductance quantization was preserved: integer plateaus remained at their values as the electron density was varied, while the number of plateaus was reduced lowering n_{2D}, fig.4.30. In spite of this, the conductance characteristics pre-

sented in this thesis show a continuous evolution of plateau-like structures with modulation of ΔV_g and the integer values quantization is not preserved in our case.

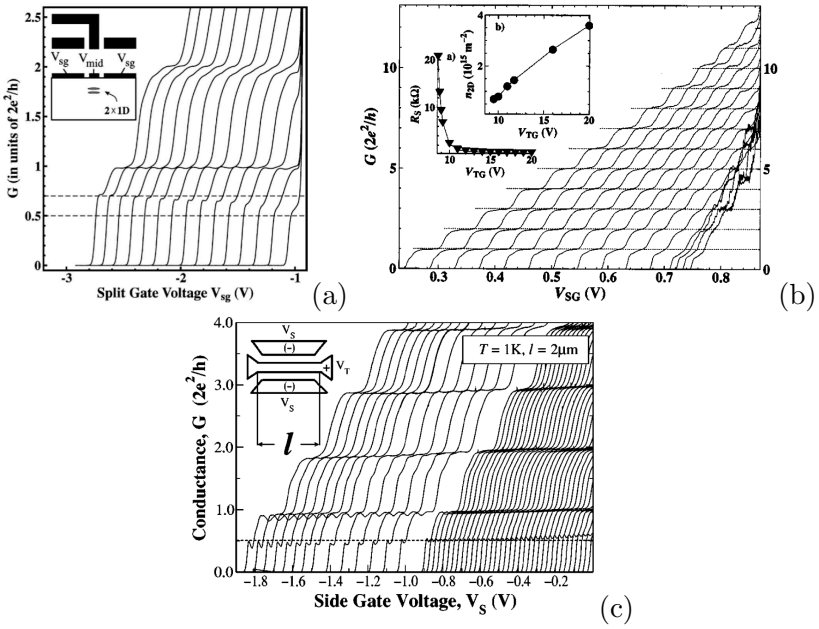

Figure 4.30: Linear conductance traces $G(V_g)$ varying parametrically the electron density by means of a *top gate*, V_{mid} in panel (a), from [150], V_{TG} in panel (b), from [151], V_T in panel (c), from [152]. In all the three cases the density was raised from left to right.

It is worth mentioning the experimental work reported by Shailos et al. [73]. Their aim was to perturb the potential profile of a split gate QPC by applying a finite bias to a finger gate located between two split gates forming the constriction. According to the performed potential profile simulations they claimed to be able to deliberately break the symmetry of the QPC structure using the finger gate which also allowed the variation of the electron density in the constriction. However their most important assumption is that the significative changes in density correspond to a variation of the Fermi energy by an amount of the order of the typical energy spacing of the lower few subbands in split-gate QPCs. In other words they state that, with some important differences, the influence of the finger gate is somewhat analogous to applying a large bias voltage across the QPC, between the source and drain contacts.

Similarly, we could assert that a change in the QPC density induced by the application of a finite gate bias difference ΔV_g would be equivalent to the application of a bias between the source and drain contacts of the QPC. Therefore we could explain our evolution of plateaus as ΔV_g varies. Indeed a variation of ΔV_g would result in the formation of 0.5 G_0 plateaus. As a matter of fact additional structures, called half plateaus, are expected to develop as a dc bias is applied between source and drain at conductance values approximately midway between the original integer values.

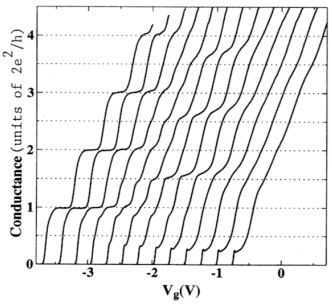

Figure 4.31: Differential conductance $G(V_g)$ at various source-drain voltages. The successive plots, taken as V_{sd} was incremented in steps of 0.5 mV, have been horizontally offset from each other by 0.2 V from left ($V_{sd} = 0$) to right ($V_{sd} = 6mV$), from [39].

While the explanation provided by ref.[73] could clarify the origin of the plateaus evolution as a finite ΔV_g is applied, in our device the broken symmetry takes place transversely respect to the direction of electrons motion. So it is still unclear if the supplied model could fit in our case once the confining potential has become transversely asymmetric. Moreover the magnetic field results suggest (with some still misunderstood aspects) that the occurrence of half-integer plateaus is to be ascribed to spin-polarized levels at zero-field (see fig.4.27). Therefore all these findings support the occurrence of an asymmetry-dependent spin polarization as reported by ref.[144].

4.3 Conclusions

This chapter presents a series of experiments performed on a GaN based 2DEG and on a selection of the nanostructures realized upon gating the heterostructure. Our 2DEG manifested a surprising high electron mobility ($\mu \sim 20000\ cm^2/Vs$) with respect to GaN two-dimensional systems with

comparable sheet carrier density ($\sim 1.1 \cdot 10^{13}\ cm^{-2}$), though still much lower compared to high-mobility $GaAs$ 2DEGs. The improved GaN 2DEG mobility is thought to be due to the insertion of an AlN exclusion layer at the heterojunction which eliminates alloy scattering. High-field magnetoresistance exhibited well-defined Shubnikov de Haas oscillations with a beating at $B \approx 5\ T$ whose origin is not obvious at this stage. One possible explanation is the effect of inhomogeneity of the electron density due to the presence of the metallic gate covering some areas of the sample. A second possible hypothesis is the presence of magneto intersubband scattering supported by the occupancy of a second level of the 2DEG. An additional possibility is that the beating of the SdH oscillations is due to spin-orbit interaction giving rise to a zero-field spin-splitting at the Fermi energy. Numerical values calculated from the SdH measurements for the spin-orbit coupling parameter ($\alpha_{so} = 2.28 \cdot 10^{-12}\ eV \cdot m$) are in agreement with literature [128]. Low-field magnetoconductivity manifested a zero-field weak anti-localization peak characteristic of spin-orbit coupling. However the numerical value of α_{so}, derived from low-field measurement, differs from previous estimate obtained by SdH analysis. Data reported in literature show a discrepancy in results obtained by using the two different types of measurements similar to that found in our work.

Using split-gate quantum point contacts, we have demonstrated ballistic transport on two-dimensional GaN systems with a sheet carrier density as large as $1.1 \sim 10^{13}\ cm^{-2}$. We have showed well-defined flat plateaus in the linear conductance of quantum point contacts. We have studied the reproducibility of conductance curve upon sweeping the gate voltage in different or in the same cooldown. The overall picture denotes various characteristic features present in the conductance curves, i.e. ill-defined plateau, amplitude reduction of conductance steps or resonance-like structures such us peaks and dips in conductance spectra. We have performed different experiments studying the effect of varying the confining potential: we deliberately introduced an asymmetry in confining potential exerted by the gates. The resulting spectra show a non trivial evolution of the conductance plateaus as the asymmetry is varied. The experimental finding were reproducible upon different thermal cycle and in different devices. Therefore an impurity-induced behaviour can be excluded as the cause of the observed data. Magnetic field measurements have shown Zeeman splitting of the quantized plateaus in one

of the reported cases. From the magnetic field splitting of the transconductance peaks we determined the energy conversion factor giving an energy spacing between transverse modes of the order of 2.2 meV, evaluated from the distance between two transconductance peaks relative to $G = 1 \cdot \frac{2e^2}{h}$ and $2 \cdot \frac{2e^2}{h}$.

Conclusions

The focus of this thesis work has been the experimental study of electron transport in quantum point contacts carried out on different heterostructures. Different approaches were used to obtain the quantum confinement. The systems under investigation were two-dimensional electron gases (2DEG) obtained by the heteroepitaxial growth of $Si/SiGe$ and $AlGaN/GaN$ heterostructures. Progresses in the semiconductor growth techniques allowed to obtain relatively high mobilities. These provide mean free paths that are similar or longer than the device sizes that can be obtained with present technology. This enabled us to study mesoscopic physics effects in devices of the size of hundreds of nanometers or more. Both the Si and the GaN-based 2DEGs, have shown to be very intriguing systems for their complexity, due to the presence of multiple valley minima, in the Si and, a large spin-orbit coupling and/or the large value of the electron density, in relation to the GaN. Complicated scenarios emerge in these systems which points to effects going beyond the independent-electrons picture.

As for the Si-based modulation doping 2DEG, the low temperature electrical characterization has demonstrated a good quality electron gas, with well-defined Shubnikov-de Haas oscillations, for magnetic field intensities lower than 1 T. SdH analyses have confirmed the results obtained from the classical low-field Hall effect, giving also further information on the relevant scattering mechanisms. Concerning the nanostructures developed starting from Si-2DEGs, these were build by using a hybrid approach in which the confinement is generated by physical etching of the 2DEG heterostructures and by a Shocktty gate employed for the electrostatic control of the potential. Devices having confining potentials of different shape were investigated. These were two quantum point contacts (QPC) obtained from the in-plane

shifting of the two square-shaped 2DEG areas and also an etched narrow straight wire (QW). A variegated framework emerged from the conductance behaviour at low temperature. The measure of the linear conductance of the QW at 4 K has shown an apparent quantization in units of $G = 4e^2/h$, as expected in a Si-based 1D narrow conducting channel in presence of both the spin and the valley degeneracy. However, upon lowering temperature, it became possible to appreciate a quantization of conductance in units of $2e^2/h$. The same results emerged in devices of different geometry investigated at low temperature (QPCs). We showed that almost all the measured conductance curves in etched Si nanostructures manifest, common characteristics at low temperature. These can be ascribed to resonance-like structures or to suppression of plateau amplitude due either to multiple reflections at the 2D-1D potential interface or to backscattering occurring at the boundaries of the confining potential or to backscattering from impurities. These structures are clearly seen to smear out and eventually disappear when the temperature is increased or when applying a perpendicular magnetic field, depending on the origin of the structures. As a matter of fact, upon increasing the perpendicular magnetic field up to 1.1 T on QPC1, the broad peaks, present in the zero-field conductance curve are seen to disappear and a fine plateau forms at $2e^2/h$. Simultaneously, at $B = 3\ T$, the non linear conductance curves exhibit the characteristic diamond plot in the transconductance, from which we measured a valley splitting energy of about 1.3 meV. On the other hand, in the narrow QW, the effect of suppression of the geometrical backscattering by the magnetic field is hardly visible since the cyclotron diameter is larger than the QW width for $B \gtrsim 7.8\ T$. Nevertheless, through the measure of the magnetoresistance oscillations in the QW, we measured an energy splitting between states that we interpreted as the valley splitting between orbital levels in this device. Comparing the behaviours of devices with different geometries by using various measurements we claimed an energy valley splitting of the order of $\sim 1\ meV$. In conclusion, we speculate that a strong confining potential is required in order to obtain valley degeneracy removal.

Chapter 4 contains the main achievements of the study of a new system such as GaN-based 2DEG. As already mentioned, GaN based heterostructures are a novel system where an intrinsic 2DEG, with high sheet carrier densities, is generated by the presence of high electric fields, caused

by piezoelectric and spontaneous polarization. The investigation of GaN 2DEG systems is a recent and growing field, whereas the study of the mesoscopic transport on GaN based nanostructures is still an almost unexplored field. It is worth while mentioning that, to our knowledge, only two papers have appeared on GaN nanodevices, ref.[148] and ref.[149]. The investigated sample has a sheet carrier density of $\sim 1.1 \cdot 10^{13}\ cm^{-2}$, with a mobility of $\mu \sim 20000\ cm^2/Vs$ at low temperatures, which makes this 2DEG quite a good sample compared to GaN 2DEGs, with identical density reported in literature. As a matter of fact the Shubnikov de Haas analysis has evidenced the good quality of the gas showing well-defined oscillations. A beat in the magneto resistance was found, and its origin is still being debated. At this preliminary stage, further measurements are required. However we propose two possible hypotheses. The most probable are magneto intersubband scattering with the occupation of a second 2DEG level or manifestation of a spin-orbit interaction.

We demonstrated the ballistic transport in one-dimensional quantum point contacts in GaN-based 2DEGs with the manifestation of a clear conductance quantization. The linear conductance curves are affected by a series of extrinsic effects ascribed to impurity backscattering, present in these systems and already reported in literature [148]. A preliminary experiment was performed with the aim of deliberately introducing an asymmetry in the confining potential. The asymmetry was obtained by differentially biasing two opposite split-gates (ΔV_g). We found a non-trivial evolution of plateau-like structures as a function of ΔV_g. The observed behaviour is compatible with the presence of a double occupancy of the level of the 2DEG with a symmetric configuration of potential. The formation of a 0.5 G_0 plateau as soon as ΔV_g is varied, points to the presence of a zero-field spin splitting, as already reported in a similar experiment [144], and attributed to a lateral spin-orbit interaction. The splitting of the conductance plateaus found upon increasing the magnetic field, gives a rough estimate of the energy spacing between 1D modes to be in the order of $\sim 2.2\ meV$.

Results obtained from the study of the GaN system are preliminary. However the investigation of the interesting and rich framework, revealed by the transport measurements on these nanostructures, is not likely to end with the work of this thesis and requires further investigations.

Some of the results obtained in this Dissertation have been presented in the following Conferences:

- *Electronic transport and conductance quantization in Si/SiGe nanostructures* L. Di Gaspare, A. Notargiacomo, G. Scappucci, G. Frucci, E. Giovine, R. Leoni, and F. Evangelisti

  E-MRS, May 29 - June 2, 2006, Nice, France.

- *Kondo-like behavior in SiGe quantum point contacts* A. Notargiacomo, L. Di Gaspare, E. Giovine, G. Frucci, V. Piazza, F. Beltram, and F. Evangelisti

  5th International Conference on Silicon Epitaxy and Heterostructures, May 20 - 2, 2007, Marseille, France.

- *Integer-spin Kondo-like behavior in SiGe quantum point contacts* A. Notargiacomo, L. Di Gaspare, E. Giovine, G. Frucci, V. Piazza, F. Beltram, and F. Evangelisti

  Electronic Properties of Two-dimensional Systems and Modulated Semiconductor Structures, July 15 - 20, 2007, Genoa, Italy.

- *Conductance Anomalies in Quantum Point Contacts* G. Frucci, A. Di Gaspare, L. Di Gaspare, A. Notargiacomo, E. Giovine, D. Spirito, and F. Evangelisti

  Proceedings of the 9th International Conference on Nanotechnology, July 26 - 30, 2009, Genoa, Italy.

The following papers are at a final stage of preparation:

- *Valley splitting in Si-based etched quantum point contact*

- *Conductance anomalies in GaN-based quantum point contacts*

- *Investigation of a AlN/GaN 2DEG with large electron density*

Bibliography

[1] S. Goswami, K. A. Slinker, M. Friesen, L. M. McGuire, J. L. Truitt, C. Tahan, L. J. Klein, J. O. Chu, P. M. Mooney, D. W. van der Wiede, R. Joynt, S. N. Coppersmith, and M. A. Eriksson, Nature Physics **3** (2007), 41.

[2] L. Kouwenhoven and L. Glazman, Phys. World **14** (2001), 33.

[3] M. Pustilnik Phys, Phys. Stat. Sol. **203** (2006), 1137.

[4] S. Sasaki, S. De Franceschi, J. M. Elzerman, W. G. van der Wiel, M. Eto, S. Tarucha, and L. P. Kouwenhoven, Nature **405** (2000), 764.

[5] D. Goldhaber-Gordon, H. Shtrikman, D. Mahalu, D. Abusch-Magder, U. Meirav, and M. A. Kastner, Nature **391** (1998), 156.

[6] S. M. Cronenwett, T. H. Oosterkamp, and L. P. Kouwenhoven, Science **281** (1998), 540.

[7] S. M. Cronenwett, H. J. Lynch, D. Goldhaber-Gordon, L. P. Kouwenhoven, C. M. Marcus, K. Hirose, N. S. Wingreen, and V. Umansky, Phys. Rev. Lett. **88** (2002), 226805–1.

[8] L. Di Gaspare, K. Alfarawi, F. Evangelisti, E. Palange, G. Barucca, and G. Majni, Appl. Phys. Lett. **79** (2001), 2031.

[9] L. Di Gaspare, G. Scappucci, E. Palange, K. Alfarawi, F. Evangelisti, G. Barucca, and G. Majni, Mat. Sci. Engin. B **89** (2002), 346.

[10] F. Schäffler, Semicond. Sci. Technol. **12** (1997), 1515.

[11] J.H. Davies, *The physics of low-dimensional semiconductors: an introduction*, Cambridge University Press, 1998.

[12] O. Ambacher, B. Foutz, J. Smart, J. R. Shealy, N. G. Weimann, K. Chu, M. Murphy, A. J. Sierakowski, W. J. Schaff, L. F. Eastman, R. Dimitrov, A. Mitchell, and M. Stutzmann, J. Appl. Phys. **87** (2000), 334.

[13] F. Bernardini, V. Fiorentini, and D. Vanderbilt, Phys. Rev. B **56** (1997), R10024.

[14] H. Okumura, Jpn. J. Appl. Phys. **45** (2006), 7565.

[15] P. T. Coleridge, R. Stoner, and R. Fletcher, Phys. Rev. B **39** (1989), 1120.

[16] S. Elhamri, R. Berney, W. C. Mitchel, W. D. Mitchell, J. C. Roberts, P. Rajagopal, T. Gehrke, E. L. Piner, and K. J. Linthicum, J. Appl. Phys. **95** (2004), 7982.

[17] S. Elhamri, W. C. Mitchel, W. D. Mitchell, G. R. Landis, R. Berney, and A. Saxler, Appl. Phys. Lett. **90** (2007), 042112.

[18] Y. Cao, K. Wang, A. Orlov, H. Xing, and D. Jena, Appl. Phys. Lett. **92** (2008), 152112.

[19] C.W.J. Beenakker and H. van Houten, Solid State Physics **44** (1998), 1.

[20] S. Datta, *Electronic transport in mesoscopic systems*, Cambridge University Press.

[21] L. L. Sohn, L. P. Kouwenhoven, and G. Schön, *Mesoscopic electron transport*, Kluwer Academic Publishers.

[22] B. J. van Wees, H. van Houten, C. W. J. Benakker, J. G. Williamson, L. P. Kouwenhoven, D. van der Marel, and C. T. Foxon, Phys. Rev. Lett. **60** (1988), 848.

[23] D. A. Wharam, T. J. Thornton, R. Newbury, M. Pepper, H. Ahmed, J. E. F. Frost, D. G. Hasko, D. C. Peacock, D. A. Ritchie, and G. A. C. Jones, J. Phys. C **21** (1988), L209.

[24] K.-F. Berggren, T. J. Thornton, D. J. Newson, and M. Pepper, Phys. Rev. Lett. **57** (1986), 1769.

[25] B. J. van Wees, L. P. Kouwenhoven, E. M. M. Willems, C. J. P. M. Harmans, J. E. Mooij, H. van Houten, C. W. J. Benakker, and J. G. Williamson, Phys. Rev. B **43** (1991), 12431.

[26] E. Tekman and S. Ciraci, Phys. Rev. B **43** (1991), 7145.

[27] M. Büttiker, Phys. Rev. B **41** (1990), 7906.

[28] J. N. L. Connor, Mol. Phys. **15** ((1968)), 37.

[29] W. H. Miller, J. Chem. Phys. **48** (1968), 1651.

[30] D. K. Ferry and S. M. Goodnick, *Transport in nanostructures*, Cambridge University Press.

[31] D. A. Wharam, *Electronic transport. part 1: Quantum point contacts and quantum wires*, Springer-Verlag, 2001.

[32] A. Grincwajg, G. Edwards, and D. K. Ferry, Physica B **227** (1996), 54.

[33] S. Roddaro, V. Piazza, F. Beltram, W. Wegscheider, C.-T. Liang, and M. Pepper, J. Appl. Phys. **92** (2002), 5304.

[34] B. J. van Wees, L. P. Kouwenhoven, H. van Houten, C. W. Beenakker, J. E. Mooij, C. T. Foxon, and J. J. Harris, Phys. Rev. B **38** (1988), 3625.

[35] H. van Houten, C. W. Beenakker, P. H. M. van Loosdrecht, T. J. Thornton, H. Ahmed, M. Pepper, C. T. Foxon, and J. J. Harris, Phys. Rev. B **37** (1988), 8534.

[36] H. Van Houten, C. W. J. Beenakker, and B. J. van Wees, *Semiconductors and semimetals*, (M. A. Reed, ed.) ed., vol. 35, Academic, New York, 1992.

[37] L. P. Kouwenhoven, B. J. van Wees, C. J. P. M. Harmans, J. G. Williamson, H. van Houten, C. W. J. Beenakker, C. T. Foxon, and J. J. Harris, Phys. Rev. B **39** (1989), 8040.

[38] N. K. Patel, L. Martín-Moreno, M. Pepper, R. Newbury, J. E. F. Frost, D. A. Ritchie, G. A. C. Jones, J. T. M. B. Janssen, J. Singleton, and J. A. A. J. Perenboom, J. Phys.: Condens. Matter **2** (1990), 7247.

[39] N. K. Patel, J. T. Nicholls, L. Martín-Moreno, M. Pepper, J. E. F. Frost, D. A. Ritchie, and G. A. C. Jones, Phys. Rev. B **44** (1991), 13549.

[40] J. E. F. Frost, K.-F. Berggren, M. Pepper, M. Grimshaw, D. A. Ritchie, A. C. Churchill, and G. A. C. Jones, Phys. Rev. B **49** (1994), 11500.

[41] S. M. Cronenwett, *Phd thesis dissertation:* Coherence, charging, and spin effects in quantum dots and point contacts, 2001.

[42] S.M. Sze, *Physics of semiconductor devices*, Wiley&Sons.

[43] O. V. Lounasmaa, *Experimental principles and methods below 1k*, Academic Press: London and New York, 1974.

[44] F. Pobell, *Matter and methods at low temperatures*, Springer, 1991.

[45] R. Radebaugh and J. D. Siegwarth, Cryogenics **11** (1971), 368.

[46] A. C. Anderson, Rev. Sci. Instrum. **51** (1980), 1603.

[47] D. Vion, P. F. Orfila, P. Joyez, D. Esteve, and M. H. Devoret, J. Appl. Phys. **77** (1995), 2519.

[48] S. Shiau, S. Chutia, and R. Joynt, Phys. Rev. B **75** (2007), 195345.

[49] K. A. Slinker, K. L. M. Lewis, C. C. Haselby, S. Goswami, L. J. Klein, J. O. Chu, S. N. Coppersmith, R. Joynt, R. H. Blick, M. Friesen, and M. A. Eriksson, New J. Phys. **7** (2005), 246.

[50] L. P. Rokhinson, L. J. Guo, S. Y. Chou, and D. C. Tsui, Appl. Phys. Lett. **76** (2000), 1591.

[51] L. J. Klein, D. E. Savage, and M. A. Eriksson, Appl. Phys. Lett. **90** (2007), 033103.

[52] R. A. Smith and H. Ahmed, J. Appl. Phys. **81** (1997), 2699.

[53] N. Shaji, C. B. Simmons, M. Thalakulam, L. J. Klein, H. Qin, H. Luo, D. E. Savage, M. G. Lagally, A. J. Rimberg, R. Joynt, M. Friesen, R. H. Blick, S. N. Coppersmith, and M. A. Eriksson, Nature Physics **4** (2008), 540.

[54] B. E. Kane, Nature **393** (1998), 133.

[55] T. Boykin, G. Klimeck, M. A. Eriksson, M. Friesen, S. N. Coppersmith, von Allmen, F. Oyafuso, and S. Lee, Appl. Phys. Lett. **84** (2004), 115.

[56] M. A. Eriksson, M. Friesen, S. N. Coppersmith, R. Joynt, L. J. Klein, K. Slinker, C. Tahan, P. M. Mooney, J. O. Chu, and S. J. Koester, Quantum Information Preocessing **3** (2004), 133.

[57] C. Tahan, M. Friesen, and R. Joynt, Phys. Rev. B **66** (2002), 035314.

[58] D. Többen, D. A. Wharam, G. Abstreiter, J. P. Kotthaus, and F. Schäffler, Semicond. Sci. Technol. **10** (1995), 711.

[59] S. L. Wang, P. C. van Son, B. J. van Wees, and T. M. Klapwijk, Phys. Rev. B **46** (1992), 12873.

[60] U. Weiser, U. Kunze, K. Ismail, and J. O. Chu, Appl. Phys. Lett. **81** (2002), 1726.

[61] E. Skuras, R. Kumar, R. L. Williams, R. A. Stradling, J. E. Dmochowski, E. A. Johnson, A. Mackinnon, J. J. Harris, R. B. Beall, C. Skierbiszewski, J. Singleton, P. J. van der Wel, and P. Wisniewski, Semicond. Sci. Technol. **6** (1991), 535.

[62] P. T. Coleridge, Semicond. Sci. Technol. **5** ((1990)), 961.

[63] P. T. Coleridge, Phys. Rev. B **44** ((1991)), 3793.

[64] M. J. Manfra, S. H. Simon, K. W. Baldwin, A. M. Sergent, K. W. West, R. J. Molnar, and J. Caissie, Appl. Phys. Lett. **85** (2004), 5278.

[65] S. L. Wang, P. C. van Son, B. J. van Wees, and T. M. Klapwijk, Phys. Rev. B **46** (1992), 12873.

[66] U. Wieser, U. Kunze, K. Ismail, and J. O. Chu, Appl. Phys. Lett. **81** (2002), 1726.

[67] M. J. Biercuk, N. Mason, J. Martin, A. Yacoby, and C. M. Marcus, Phys. Rev. Lett. **94** (2005), 026801.

[68] A. Kristensen, H. Bruus, A. E. Hansen, J. B. Jensen, P. E. Lindelof, C. J. Marckmann, J. Nygå rd, C. B. Sorensen, F. Beuscher, A. Forchel, and M. Michel, Phys. Rev. B **62** (2000), 10950.

[69] C.-T. Liang, M. Y. Simmons, C. G. Smith, D. A. Ritchie, and M. Pepper, Appl. Phys. Lett. **75** (1999), 2975.

[70] A. Yacoby, H. L. Stormer, N. S. Wingreen, L. N. Pfeiffer, K. W. Baldwin, and K. W. West, Phys. Rev. Lett. **77** (1996), 4612.

[71] D. Kaufman, Y. Berk, B. Dwir, A. Rudra, A. Palevski, and E. Kapon, Phys. Rev. B **59** (1999), R10433.

[72] K. J. Thomas, J. T. Nicholls, M. Y. Simmons, M. Pepper, D. R. Mace, and D. A. Ritchie, Phys. Rev. Lett. **77** (1996), 135.

[73] A. Shailos, A. Ashok, J. P. Bird, R. Akis, D. K. Ferry, S. M. Goodnick, M. P. Lilly, J. L. Reno, and J. A. Simmons, J. Phys.: Condens. Matter **18** (2006), 1715.

[74] O. Gunawan, B. Habib, E. P. De Poortere, and M. Shayegan, Phys. Rev. B **74** (2006), 155436.

[75] H. Bruus, V. V. Cheianov, and K. Flensberg, Physica E **10** (2001), 97.

[76] Y. Meir, K. Hirose, and N. S. Wingreen, Phys. Rev. Lett. **89** (2002), 196802.

[77] T.-M. Chen, A. C. Graham, M. Pepper, I. Farrer, and D. A. Ritchie, Phys. Rev. B **79** (2009), 153303.

[78] L. M. McGuire, M. Friesen, K. A. Slinker, S. N. Coppersmith, and M. A. Eriksson, cond.-mat. (2008), arXiv.org:0810.0538.

[79] K. Nishiguchi and S. Oda, Appl. Phys. Lett. **76** (2000), 2922.

[80] F. J. Ohkawa and Y. Uemura, J. Phys. Soc. Japan **43** (1977), 907.

[81] T. B. Boykin, G. Klimeck, M. Friesen, S. N. Coppersmith, P. von Allmen, F. Oyafuso, and S. Lee, Phys. Rev. B **70** (2004), 165325.

[82] K. Takashina, Y. Ono, A. Fujiwara, Y. Takahashi, and Y. Hirayama, Phys. Rev. Lett. **96** (2006), 236801.

[83] P. Weitz, R. Haug, K. von Klitzing, and F. Schäffler, Surface Science **362** (1996), 542.

[84] S. J. Koester, K. Ismail, and J. O. Chu, Semicond. Sci. Technol. **12** (1997), 384.

[85] M. Friesen, S. Chutia, C. Tahan, and S. N. Coppersmith, Phys. Rev. B **75** (2007), 115318.

[86] M. O. Nestoklon, E. L. Ivchenko, J.-M. Jancu, and P. Voisin, Phys. Rev. B **77** (2008), 155328.

[87] H. Kothari, A. Ramamoorthy, R. Akis, S. M. Goodnick, D. K. Ferry, J. L. Reno, and J. P. Bird, J. Appl. Phys. **103** (2008), 013701.

[88] K.-F. Berggren, G. Roos, and H. van Houten, Phys. Rev. Lett. **37** (1988), 10118.

[89] H. van Houten, B. J. van Wees, J. E. Mooij, G. Roos, and K.-F. Berggren, Superlattices Microstruct. **3** (1987), 497.

[90] A. B. Fowler, F. F. Fang, W.E. Howard, and P. J. Stiles, Phys. Rev. Lett. **16** (1966), 901.

[91] T. Ando, A. B. Fowler, and F. Stern, Rev. Mod. Phys. **54** (1982), 437.

[92] A. D. Bykhovski, R. Gaska, and M. S. Shur, Appl. Phys. Lett. **72** (1998), 3577.

[93] W. Knap, E. Frayssinet, M. L. Sadowski, C. Skierbiszewski, D. Maude, V. Falko, M. A. Khan, and M. S. Shur, Appl. Phys. Lett. **75** (1999), 3156.

[94] L. K. Li, B. Turk, I. Wang, W, S. Syed, D. Simonian, and H. L. Stormer, Appl. Phys. Lett. **76** (2000), 742.

[95] C. P. Jiang, S. L. Guo, Z. M. Huang, L. Yu, Y. S. Gui, G. Z. Zheng, J. H. Chu, Z. W. Zheng, B. Shen, and Y. D. Zheng, Appl. Phys. Lett. **79** (2001), 374.

[96] A. Link, T. Graf, O. Ambacher, A. Jimenez, E. Calleja, Y. Smorchkova, J. Speck, U. Mishra, and M. Stutzmann, Phys. Stat. Sol. **234** (2002), no. 3, 805.

[97] W. Knap, V. I. Fal'ko, E. Frayssinet, P. Lorenzini, N. Grandjean, D. Maude, G. Karczewski, B. L. Brandt, J. Lusakowski, I. Grzegory, M. Leszczyǹski, P. Prystawko, C. Skierbiszewski, S. Porowski, X. Hu, G. Simin, M. A. Khan, and M. S. Shur, J. Phys.: Condens. Matter **16** (2004), 3421.

[98] S. Syed, M. J. Manfra, Y. J. Wang, R. J. Molnar, and H. L. Stormer, Appl. Phys. Lett. **84** (2004), 1507.

[99] Z. J. Qiu, Y. S. Gui, T. Lin, N. Dai, J. H. Chu, N. Tang, J. Lu, and B. Shen, Phys. Rev. B **69** (2004), 125335.

[100] T. W. Kim, D. C. Choo, Y. R. Jang, K. H. Yoo, M. H. Jung, Y. H. Cho, Jae-H. Lee, and Jung-H. Lee, Solid State Commun. **132** (2004), 67.

[101] M. J. Manfra, K. W. Baldwin, A. M. Sergent, K. W. West, R. J. Molnar, and J. Caissie, Appl. Phys. Lett. **85** (2004), 5394.

[102] T. W. Kim, D. C. Choo, K. H. Yoo, M. H. Jung, Y. H. Cho, Jae-H. Lee, and Jung-H. Lee, J. Appl. Phys. **97** (2005), 103721.

[103] H.-I. Cho, G. M. Gusev, Z. D. Kvon, V. T. Renard, J.-H. Lee, and J.-C. Portal, Phys. Rev. B **71** (2005), 245323.

[104] X. Han, Y. Honda, T. Narita, M. Yamaguchi, and N. Sawaki, J. Phys.: Condens. Matter **19** (2007), 046204.

[105] K. Lai, W. Pan, D. C. Tsui, S. Lyon, M. Muhlberger, and F. Schäffler, Phys. Rev. Lett. **96** (2006), 076805.

[106] I. Lo, J.-K. Tsai, W. J. Yao, P. C. Ho, L.-W. Tu, T. C. Chang, S. Elhamri, W. C. Mitchel, K. Y. Hsieh, J. H. Huang, H. L. Huang, and W.-C. Tsai, Phys. Rev. B **65** (2002), 161306(R).

[107] K. Tsubaki, N. Maeda, T. Saitoh, and N. Kobayashi, Appl. Phys. Lett. **80** (2002), 3126.

[108] N. Tang, B. Shen, M. J. Wang, K. Han, Z. J. Yang, K. Xu, G. Y. Zhang, T. Lin, B. Zhu, W. Z. Zhou, and J. H. Chu, Appl. Phys. Lett. **88** (2006), 172112.

[109] S. Schmult, M. J. Manfra, A. Punnoose, A. M. Sergent, K. W. Baldwin, and R. J. Molnar, Phys. Rev. B **74** (2006), 03302.

[110] I. Lo, W.-Y. Pang, Y.-L. Chen, Y.-C. Hsu, J.-C. Chiang, W.-H. Lin, W.-T. Chiu, J.-K. Tsai, and C.-N. Chen, Appl. Phys. Lett. **93** (2008), 132114.

[111] N. Tang, B. Shen, K. Han, F.-C. Lu, Z.-X. Qin, and G.-Y. Zhang, Phys. Rev. B **79** (2009), 073304.

[112] Z. W. Zheng, B. Shen, Y. S. Gui, C. P. Jiang, N. Tang, R. Zhang, Y. Shi, Y. D. Zheng, S. L. Guo, G. Z. Zheng, J. H. Chu, T. Someya, and Y. Arakawa, Appl. Phys. Lett. **82** (2003), 1872.

[113] E. A. de Andrada e Silva, G. C. La Rocca, and F. Bassani, Phys. Rev. B **50** (1994), 8523.

[114] N. Thillosen, S. Cabanas, N. Kaluza, V. A. Guzenko, H. Hardtdegen, and Th. Schäpers, Phys. Rev. B **73** (2006), 241311R.

[115] N. Tang, B. Shen, Z. W. Zheng, J. Liu, D. J. Chen, J. Lu, R. Zhang, Y. Shi, Y. D. Zheng, Y. S. Gui, C. P. Jiang, Z. J. Qiu, S. L. Guo, J. H. Chu, K. Hoshino, T. Someya, and Y. Arakawa, J. Appl. Phys. **94** (2003), 5420.

[116] Z. J. Qiu, Y. S. Gui, Z. W. Zheng, N. Tang, J. Lu, B. Shen, N. Dai, and J. H. Chu, Solid State Commun. **129** (2004), 187.

[117] K. S. Cho, T.-Y. Huang, H.-S. Wang, M.-G. Lin, T.-M. Chen, C.-T. Liang, and Y. F. Chen, Appl. Phys. Lett. **86** (2005), 222102.

[118] N. Tang, B. Shen, M. J. Wang, Z. J. Yang, K. Xu, G. Y. Zhang, D. J. Chen, Y. Xia, Y. Shi, R. Zhang, and Y. D. Zheng, Phys. Rev. B **73** (2006), 037301.

[119] T. H. Sander, S. N. Holmes, J. J. Harris, D. K. Maude, and J.-C. Portal, Phys. Rev. B **58** (1998), 13856.

[120] L. Hsu and W. Walukiewicz, Phys. Rev. B **56** (1997), 1520.

[121] Z. W. Zheng, B. Shen, R. Zhang, Y. S. Gui, C. P. Jiang, Z. X. Ma, G. Z. Zheng, S. L. Guo, Y. Shi, P. Han, Y. D. Zheng, T. Someya, and Y. Arakawa, Phys. Rev. B **62** (2000), R7739.

[122] I. Lo, W. T. Wang, M. H. Gau, J.-K. Tsai, S. F. Tsay, and J.-C. Chiang, Appl. Phys. Lett. **88** (2006), 082108.

[123] I. Lo, J.-K. Tsai, W. J. Yao, P. C. Ho, L.-W. Tu, T. C. Chang, S. Elhamri, W. C. Mitchel, K. Y. Hsieh, J. H. Huang, H. L. Huang, and W.-C. Tsai, Phys. Rev. B **73** (2006), 037302.

[124] R. H. Silsbee, J. Phys.: Condens. Matter **16** (2004), R179.

[125] I. Lo, Y.-L. Chen, W. Y. Pang, Y.-C. Hsu, J.-C. Chiang, C. C. Yang, and J. Y. Su, J. Appl. Phys. **105** (2009), 093716.

[126] W. Weber, S. D. Ganichev, S. N. Danilov, D. Weiss, W. Prettl, Z. D. Kvon, V. V. Bel'kov, L. E. Golub, H.-I. Cho, and J.-H. Lee, Appl. Phys. Lett. **87** (2005), 262106.

[127] W. Z. Zhou, T. Lin, L. Y. Shang, L. Sun, K. H. Gao, Y. M. Zhou, G. Yu, N. Tang, K. Han, B. Shen, S. L. Guo, Y. S. Gui, and J. H. Chu, J. Appl. Phys. **104** (2008), 053703.

[128] S. B. Lisesivdin, N. Balkan, O. Makarovsky, A. Patanè, A. Yildiz, M. D. Caliskan, M. Kasap, S. Ozcelik, and E. Ozbay, J. Appl. Phys. **105** (2009), 093701.

[129] N. Tang, B. Shen, K. Han, F.-C. Lu, F.-J. Xu, Z.-X. Qin, and G.-Y. Zhang, Appl. Phys. Lett. **93** (2008), 172113.

[130] N. Thillosen, Th. Schäpers, N. Kaluza, H. Hardtdegen, and V. A. Guzenko, Appl. Phys. Lett. **88** (2006), 022111.

[131] C. Kurdak, N. Biyikli, U. Ozgur, H. Morkoc, and V. I. Litvinov, Phys. Rev. B **74** (2006), 113308.

[132] H. Cheng, N. Biyikli, U. Ozgur, C. Kurdak, H. Morkoc, and V. I. Litvinov, Physica E **40** (2008), 1586.

[133] A. E. Belyaev, V. G. Raicheva, A. M. Kurakin, N. Klein, and S. A. Vitusevich, Phys. Rev. B **77** (2008), 035311.

[134] J. Lu, B. Shen, N. Tang, D. J. Chen, H. Zhao, D. W. Liu, R. Zhang, Y. Shi, Y. D. Zheng, Z. J. Qiu, Y. S. Gui, B. Zhu, W. Yao, J. H. Chu, K. Hoshino, and Y. Arakawa, Appl. Phys. Lett. **85** (2004), 3125.

[135] M. Ahoujja, W. C. Mitchel, S. Elhamri, R. S. Newrock, D. B. Mast, J. M. Redwing, M. A. Tischler, and J. S. Flynn, Journ. Electr. Mat. **27** (1998), 210.

[136] A. Link, T. Graf, R. Dimitrov, O. Ambacher, M. Stutzmann, Y. Smorchkova, U. Mishra, and J. Speck, Phys. Stat. Sol. **228** (2001), no. 2, 603.

[137] C.G. Smith, M. Pepper, R. Newbury, H. Ahmed, D.G. Hasko, D.C. Peacock, J.E.F. Frost, D.A. Ritchie, G.A.C. Jones, and G. Hills, J. Phys.: Condens. Matter **1** (1989), 6763.

[138] S. F. Fischer, G. Apertrii, U. Kunze, D. Schuh, and G. Abstreiter, Phys. Rev. B **71** (2005), 195330.

[139] G. Salis, T. Heinzel, K. Ensslin, O. J. Homan, W. Bächtold, K. Maranowski, and A. C. Gossard, Phys. Rev. B **60** (1999), 7756.

[140] M. A. Topinka, B. J. LeRoy, S. E. J. Shaw, E. J. Heller, R. M. Westervelt, K. D. Maranowski, and A. C. Gossard, Science **289** (2000), 2323.

[141] A. R. Rocha and J. A. Brum, Braz. J. Phys. **32** (2001), 296.

[142] F. Sfigakis, C. J. B. Ford, M. Pepper, M. Kataoka, D. A. Ritchie, and M. Y. Simmons, Phys. Rev. Lett. **100** (2008), 026807.

[143] K. M. Liu, J. H. Hsiao, T. M. Hong, V. Umansky, and S. Y. Hsu, Journ. Phys. Conference Series **150** (2009), 022052.

[144] P. Debray, S. M. Rahman, J. Wan, R. S. Newrock, M. Cahay, A. T. Ngo, S. E. Ulloa, S. T. Herbert, M. Muhammad, and M. Johnson, Nature Nanotechnology **advance online publication** (2009), –.

[145] J. G. Williamson, C. E. Timmering, C. J. P. M. Harmans, J. J. Harris, and C. T. Foxon, Phys. Rev. B **42** (1990), 7675.

[146] K. J. Thomas, J. T. Nicholls, N. J. Appleyard, M. Y. Simmons, M. Pepper, D. R. Mace, W. R. Tribe, and D. A. Ritchie, Phys. Rev. Lett. **58** (1998), 4846.

[147] T. E. Day, A. Cummings, A. M. Burke, J. L. Reno, D. K. Ferry, and S. M. Goodnick, *Transport through magnetic quantum point contacts*, Prooceding 9^{th} *Nanotechnology Conference: IEEE NANO2009*, 2009.

[148] H. T. Chou, S. Lüscher, D. Goldhaber-Gordon, M. J. Manfra, A. M. Sergent, K. W. West, and R. J. Molnar, Appl. Phys. Lett. **86** (2005), 073108.

[149] H. T. Chou, D. Goldhaber-Gordon, S. Schmult, M. J. Manfra, A. M. Sergent, and R. J. Molnar, Appl. Phys. Lett. **89** (2006), 033104.

[150] K. J. Thomas, J. T. Nicholls, M. Pepper, W. R. Tribe, M. Y. Simmons, and D. A. Ritchie, Phys. Rev. B **61** (2000), R13365.

[151] K. S. Pyshkin, C. J. B. Ford, R. H. Harrel, M. Pepper, E. H. Linfield, and D. A. Ritchie, Phys. Rev. B **62** (2000), 15842.

[152] S. M. Reimann, M. Koskinen, and M. Manninen, Phys. Rev. B **59** (1999), 1613.

[153] E. H. Lieb and D. Mattis, Phys. Rev. B **81** (1998), 3199.

[154] A. V. Andreev and A. Kamenev, Phys. Rev. Lett. **81** (1998), 3199.